# 博　士　論　文

# Internal geometries and mechanical properties of discontinuous carbon fiber reinforced thermoplastics

（不連続炭素繊維強化熱可塑性樹脂の内部形態と力学特性）

万　　熠

# Preface

This thesis is one of the fruits of my five-year student life in the University of Tokyo. The research originally stemmed from my passion for developing a considerable methodology for detailed evaluation of discontinuous CFRTP.

In truth, I could not have achieved my current level of success without a strong support group and this thesis would not have been possible without the help from all the related persons.

I owe my deepest gratitude to my supervisor, Professor Jun Takahashi. He always provided me with new insights with his wide range of knowledge. In research, he not only showed me the direction with his strong leadership but also told me how to steer the way by myself.

I would like to thank Professor Stepan Lomov and Doctor Ilya Straumit from Katholieke Universiteit Leuven, the collaborative research of X-ray micro-CT enriched my thesis and inspired my cognition of corresponding research.

I am also grateful to the academic staffs Mr. Isamu Ohsawa and Ms. Mizuki Ohta who helped me with a lot of experimental studies.

I wish to thank the administrative staffs Ms. Emi Ohya and Ms. Junko Enomoto who always helped me on the document works.

I also wish to thank the juniors and graduated seniors in the laboratory. The communication and collaboration in research encouraged my work itself.

Lastly, I owe my loving thanks to my parents. Without their support, patience, and understanding not only in these five years but through all my life, it would have been impossible for me to finish this work. I dedicate this thesis to them.

August 2017. Tokyo, Japan
Yi Wan

# **Abstract**

Discontinuous carbon fiber reinforced thermoplastics (DCFRTP) are the combination of randomly oriented discontinuous fibers having considerable complex-shaped molding capabilities with the thermoplastics resins exhibit superior cycle molding time and good in-plant recyclability. Consequently, DCFRTP are regarded as potential substitutes for metallic materials applied in mass-production (e.g. automotive manufacturing industry) fields.

The main barriers obstructing the DCFRTP from industrial applications at present are the lack of comprehensive understanding of fabricating, material compositions and mechanical properties. Through this thesis, two kinds of DCFRTP with different components and fabrication processes, carbon fiber mats reinforced thermoplastics (CMT) and chopped carbon fiber tapes reinforced thermoplastics (CTT), are analyzed in detail on the aspects of internal geometries and mechanical properties to achieve further insight on the material researches and industrial applications of these composites.

Two different X-ray micro-CT methodologies, VoxTex and TRI/3D-BON, were applied. Multi-scale internal geometry analyses were conducted on CMT and CTT to investigate the structural features in fiber-, layer- and macro-level. Limitations and restrictions of X-ray facilities on the X-ray analysis were discussed in detail and solved statistically. The relationships between the internal geometry and fabricating properties like molding conditions and component sizes were revealed quantifiably. In CTT, it was found that higher molding pressure can decrease the structure regularity due to tape splitting, and the tape length exhibits positive effect on increasing the layer independence through thickness direction. The out-of-plane waviness and out-of-plane orientation tensor calculated from tape thickness of CTT showed considerable linearity with corresponding tensile properties. The internal geometry properties like orientation tensors and layered orientation distributions were collected from the two X-ray micro-CT methodologies to achieve precise descriptions of CMT and CTT.

Tensile tests and two different analytical simulation methods, Mori-Tanaka method and equivalent laminate method were applied to evaluate the tensile properties of CMT and CTT in different fabricating processes and components. Fiber orientation tensors calculated from 3D-BON method were applied to the Mori-Tanaka methods and internal geometry properties collected from the VoxTex method were input to the equivalent laminate methods. The aspect ratio of reinforcements and components properties of CMT and CTT were also studied in detail to increase the accuracy

and reliability of simulations. The CTT exhibit higher Young's moduli with lower tensile fracture strain compared with CMT. Considerable results were achieved in both the Mori-Tanaka method and equivalent laminate method simulations of CTT, while the simulation results of CMT generally overestimated the tensile properties. This difference indicated the difference in CAE capability between CTT and CMT. The Mori-Tanaka method provided better accuracy in tensile moduli while the equivalent laminate method demonstrated considerable tape length dependency on the tensile strengths due to the different simplification processes during the modeling. Determination of optimal strand aspect ratio of CTT is given by the simulation methods based on the comprehensive consideration of mechanical simulation results with manufacturing conditions.

The combination of X-ray micro-CT methods and analytical simulation models open the new ways for comprehensive solution methodologies of DCFRTP analyses with the criterions and suggestions of DCFRTP applications.

# Contents

# List of Figures

---

# List of Tables

# List of Equations

# Chapter 1.   Introduction

## 1.1.  Backgrounds

Carbon fiber reinforced polymers (CFRP) are now generally regarded as the substitutes for metallic materials where high mechanical properties and light weight are required. Conventionally, epoxy and other thermoset resins were selected as the matrix material. In recent years, carbon fiber reinforced thermoplastics (CFRTP) have attracted attentions from both researchers and engineers and significant progress have been made in the relative developments. It is because compared to the traditional thermoset polymers, thermoplastics show superiorities on short cycle molding time and good in-plant recyclability as well as omitting the curing process. On the other hand, randomly oriented discontinuous carbon fiber reinforced polymers (DFRP) are the preferred composites for applications involving the mass-productions (e.g. automotive manufacturing industry) because the randomly oriented discontinuous fiber systems generally show achievability of high cycles molding and high capability of being manufactured in complex geometries without internal structural damage. Consequently, the combination of the thermoplastic polymers with the randomly oriented discontinuous carbon fibers is considered to mix their advantages, and the

discontinuous carbon fiber reinforced thermoplastics (DCFRTP) are regarded as potential substitutes for metallic materials applied in mass-production of automotive parts.

Under this situation, a national project was expanded in our research group since 2013fy, named the Japanese METI project 'the Future Pioneering Projects / Innovative Structural Materials Project' [1]. In this project, the focus is on the reduction of energy consumption in the transport sector. The growth of total fossil energy consumption is mainly led by the increase of the energy consumed in the transport sector since the 1970s (Figure 1-1 (a)). That is, a decrease in the energy consumption of the vehicles can lead to a significant reduction in the total fossil energy consumption, which can both help protect the environment and reduce the stress on energy imports. The life cycle assessment of vehicles (Figure 1-1 (b)) indicates that most of the energy is consumed during the driving stage. As a solution, applying the CFRTP on the vehicle body can decrease the momentum and kinetic energy of the vehicles, which helps reduce the driving energy consumption as well as improve the driving performance [1, 2].
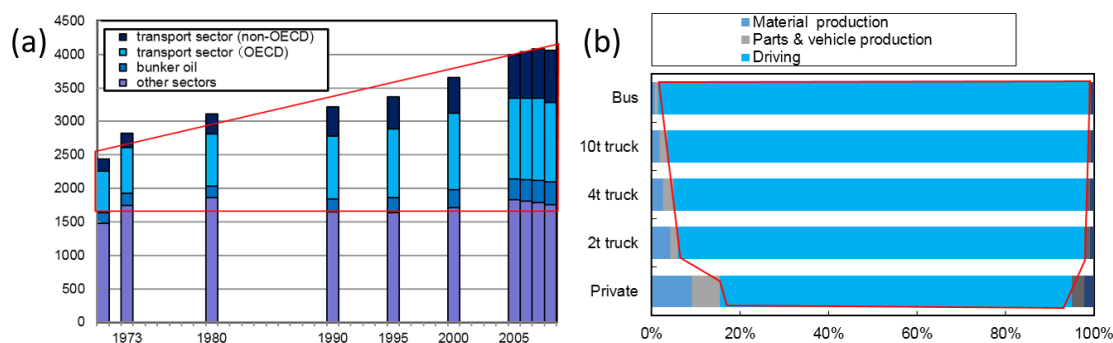


**Figure 1-1. Total fossil energy consumption tendency (a) and energy consumption of vehicles by life cycle assessment (b) [2].**

To achieve the mass-production application, the mechanical performance, cost efficiency, cycle molding time and complex molding formability are considered. The CFRTP composited with traditional industrial plastics like polypropylene (PP) and polyamide 6 (PA6) exhibit high cycle molding time with relatively low resin melting temperature and considerable economic efficiency. The Figure 1-2 illustrates the schematics of high cycle stamping molding processes of CFRTP developed in our research group, which exhibits the feasibility to conduct cycle molding of CFRTP within 1 minute. Combined with the cheap industrial plastics PP or PA6, cost-efficient high speed cycle molding processes can be established.

The CFRTP developed at present can be generally classified into four different types based on their fiber length and morphologies. Table 1-1 listed the four types of CFRTP, which are the continuous fiber systems (unidirectional, laminate and woven structures), injection molding composites, fiber mat structures (randomly oriented fibers in general) and short strands (randomly oriented strands (ROS)). To ensure high mechanical performances, the high fiber volume fraction is required. To achieve the complex molding formability, discontinuous fiber systems are regarded as the better choice because the wrinkles and creases are generally generated during the compression molding processes of continuous fiber composites. Consequently, the discontinuous CFRTP composited with fiber mats and short strands are considered to be the suitable candidates for the mass-production applications in automotive industry and regarded as the main target materials in the present study.

**Table 1-1. Four types of CFRTP.**

| Type | Continuous fibers | Injection molding | Fiber mats | Short strands |
|---|---|---|---|---|
| Fiber volume fraction ($V_f$) | Over 50% | Generally less than 5% | Around 10 to 30% | Over 50% |
| Fiber length | Continuous | Around 1 mm or less | Several millimeters | Around 10 to 100 millimeters |
| Complex molding | Difficult | Suitable | Possible | Suitable |
| Orientation | Based on design | Injection direction preference | Generally transversely isotropic | Generally transversely isotropic |
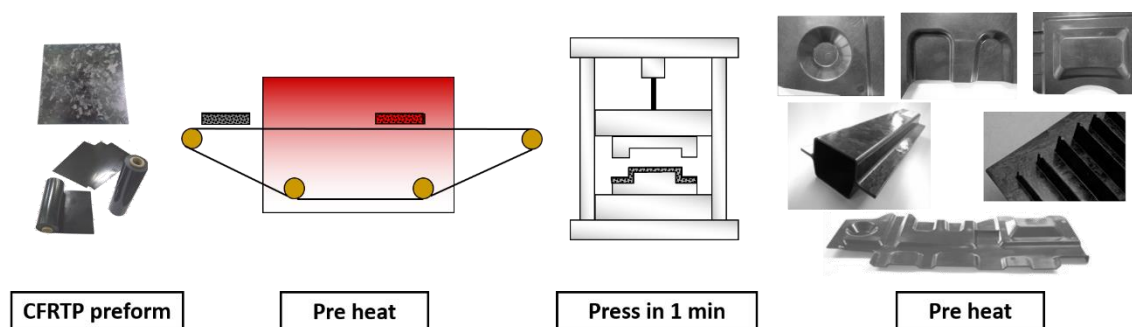
**Figure 1-2. Fabricating process of carbon fiber reinforced thermoplastics in high cycle stamping molding [1].**

To achieve the goal towards the mass-production applications of DCFRTP in the automotive industry, comprehensive knowledge of DCFRTP is required. The performances and computer aided engineering (CAE) capabilities of DCFRTP must be verified carefully to ensure the reliability and safety during application. Also the fabrication processes, not only for the materials themselves but also for the mass-production approaches, should be considered in detail to ensure the manufacturing efficiency and economic possibility. As the initial approach, internal geometries and mechanical properties are the dominate features of composites in material characterizations. Consequently, the present research is started based on this background to acquire the comprehensive knowledge of internal geometries and mechanical properties of DCFRTP and to ensure the feasibility of mass-production applications.

## 1.2. Previous studies

The subject of this research is the internal geometries and mechanical properties of DCFRTP as introduced in the previous section. In this section, researches concerning the development of internal geometry analysis and mechanical property characterization of composites are reviewed thoroughly.

### 1.2.1. Internal geometry analysis

Knowledge of internal geometry properties like fiber orientation in DCFRTP are of great importance because internal geometry has numerous implications on the functional and mechanical performances of the composites [3]. The experimental evaluation of the internal

4

geometries (especially the fiber orientations) in composites can be performed by different methods. One of the first methods to be proposed on discontinuous fiber systems, which is still the most commonly employed today, is based on the optical observation of the elliptical footprints left by the fibers on polished cross sections of a sample, from which the fiber orientation angles can be inferred [4]. In the optical observation method, the orientation of each single fiber is calculated from the measured diameters of the orientation angle $\phi$ with respect to the in-plane direction. As illustrated in the Figure 1-3, the orientation angle is calculated by the orientation parameter $f$ proposed by Hermans [5] for describing the orientation in crystalline polymers. The "Hermans' orientation parameter" $f_p$ is of the form:

$$f_p = 2\langle cos^2\phi \rangle - 1 \qquad \textbf{Equation 1-1}$$

where

$$\langle cos^2\phi \rangle = \frac{\sum_i N(\phi_i)cos^2\phi_i}{\sum_i N(\phi_i)} \qquad \textbf{Equation 1-2}$$

and $\phi_i$ represents the angle between the individual fibers and the primary axis (in-plane direction), and $N(\phi_i)$ is the number of fibers under certain angle $\phi_i$. The parameter $f_p$ is scaled and range from zero to 1 to determine the degree of anisotropy.
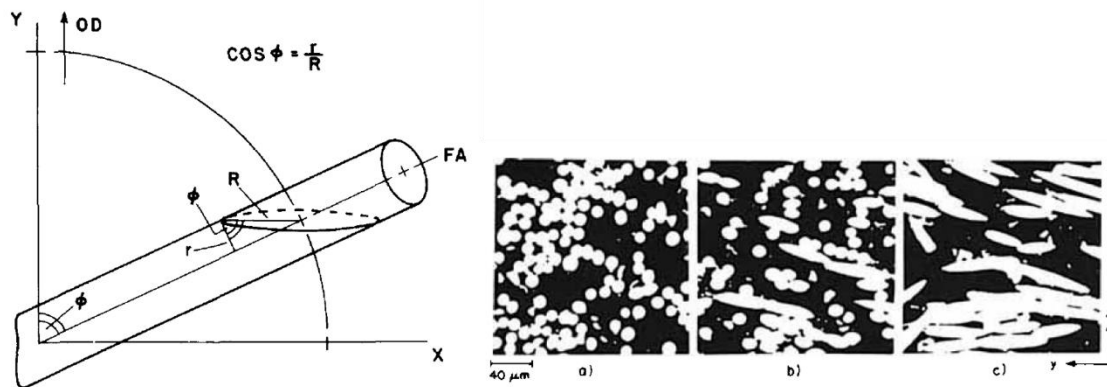


**Figure 1-3. Schematic of the fiber orientation angle $\phi$ and cross section of fiber (left), micrographs of three typical areas of short glass fiber composites [5].**

However, the optical observation method requires sectioning preparation of the sample at the location where measurements are performed, thus resulting in a fully destructive method. When applying this method, the dependence on fiber orientation of the probability for a plane to cross a fiber has to be taken into consideration [3, 6, 7]. In some cases, issues arise about the accuracy of angle measurements for different cross sections and fibers almost perpendicular to the section plane, and Bay et. al. conducted some discussions on these issues [8]. The ambiguity about the sign of the orientation angle and the image resolution problems are provided by Davidson [9],

and special techniques like the two section method [9, 10] (Figure 1-4) and the advanced use of confocal microscopy [11-13] have been proposed. Furthermore, the optical observation method is able to conduct the analysis of relatively large samples under the automation [14-16]. The use of optical observation method is widespread in the researches on fiber reinforced composites with relatively simple internal geometries (continuous fiber systems, short fiber with low fiber volume fractions, etc.), thanks to the relative simplicity of the setup required, and particularly compared with microtomography methods [3].
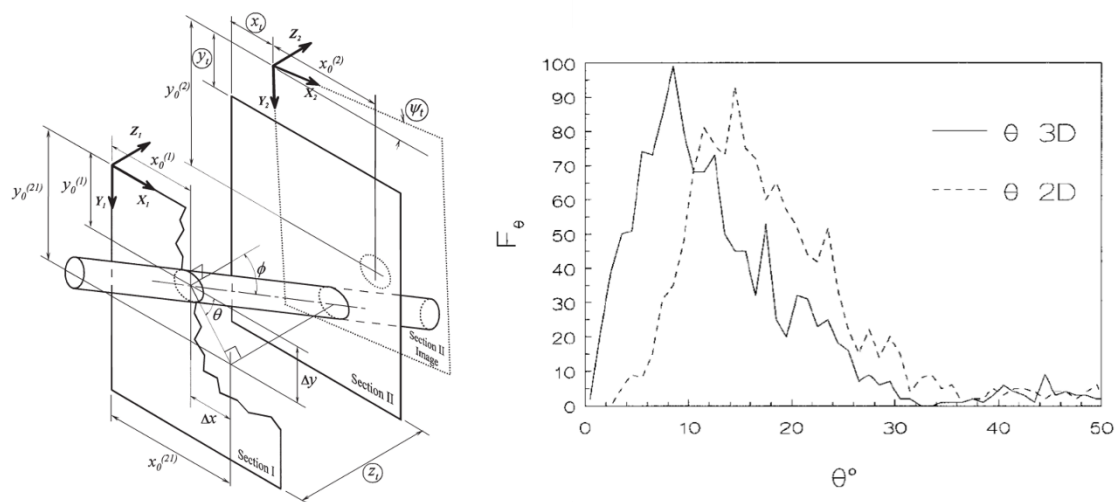


**Figure 1-4. Schematic of two section method (left) [10] and the calculated fiber orientation compare with single section result [9].**

X-ray radiography is another approach to the analysis of fiber orientation [17, 18]. In principle, it is a non-destructive method, although, in the case of members with non-planar geometry, extraction of samples might be required. It is based on the projection of X-rays and the analysis of the absorption patterns onto an X-ray sensitive plate or sensor. Thus, it can provide only information on the orientation of the projection of fibers onto this plane. This simplification missing information of the 3D structures and these limitations of radiography can be overcome under the combination with Computed Tomography (CT), which is based on a series of radiographic projections taken at varying angles [3]. In X-ray CT methods the radiographic projections are processed by algorithms allowing for reconstruction of the internal structure of the observed sample. For the analysis of fiber reinforced composites, a resolution of the order of fibers' diameter is required (less than the fiber radius can bring high accuracy), which is possible with special micro-CT equipment. Moreover, in the case of materials having constituents of similar and low absorption index (e.g. carbon fibers in a polymer matrix), identification of fibers

6

can become very difficult, if not impossible. The problem of the low absorption index of polymers and of other constituents like carbon fibers can be overcome by using non-conventional X-ray sources, particularly synchrotron light, which allows for exploiting phase contrast techniques [19]. Micro-CT, because of the small size of samples which is possible to analyze, results into a partially non-destructive method.

The 3D model reconstructed by X-ray micro-CT has to be processed in order to analyze the internal fiber architecture. Methods have been proposed, aiming at isolating each single fiber and then calculating its orientation angles, but they are applicable only in the case of relatively low fiber content and are very likely to generate fragments and "miss" a high percentage of fiber (Figure 1-5) [20]. More recently, methods for the analysis of the fiber distribution in samples reconstructed by micro-CT has been proposed, based on the Mean Intercept Length (MIL) concept [21, 22] and "voxel model" [19, 23, 24].

The MIL is a parameter commonly used in biomechanics [25] and also have been applied to evaluate distributions of reinforcing fibers in polymer composites [21, 26]. For a given structure composed of two different constituents, the MIL is defined as the average distance between the two phases along a certain direction. To measure the MIL of planar distributions, a grid of length $L$ is placed on the X-ray image, oriented along a direction with angle $\theta$ (Figure 1-6). By counting the number of fiber to matrix transitions $I(\theta)$, the MIL is evaluated as

$$MIL(\theta) = \frac{L}{I(\theta)}$$ **Equation 1-3**

The MIL is a function of the orientation angle $\theta$, and higher values are obtained along directions with fewer intersections.

On the other hand, the "voxel model" method is used to designate a high-level description of the material's microstructure. This method is developed in these years by Lomov [23, 24] and a software named VoxTex including this method is developed in the collaboration research of Lomov and me [19] and applied in the present study. The detailed algorithm of "voxel model" is introduced in sub-section 2.3.2.1.

By these methods, it is possible to characterize the internal fiber structure by means of the components of second order tensors, the MIL fabric tensor and the structural tensor, and derive useful information about the preferred fiber orientation and the degree of anisotropy. These methods can be applied to subsets of the reconstructed volume, called volumes of interest (VOI).

Each VOI contains a certain number of fibers, thus avoiding analyzing each single fiber. By these methods, several VOIs can be quickly and easily analyzed at varying depths from the free surfaces and avoid physical sectioning and polishing compare with the optical observation method. Even if information about the orientation of each single fiber is not captured, the method is able to provide a global characterization of fiber distribution [3].
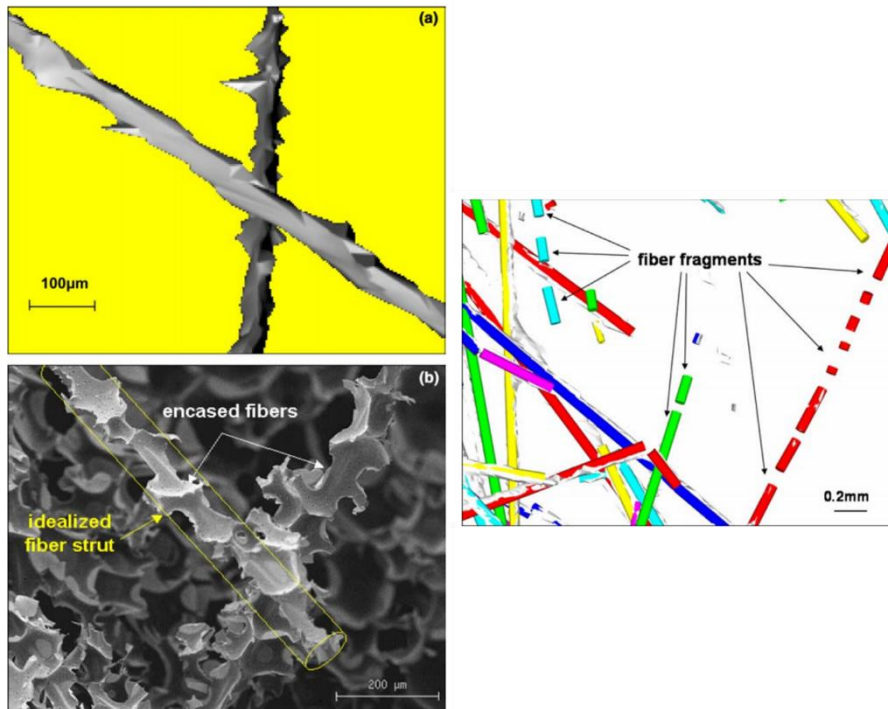


**Figure 1-5. Reconstructed image and SEM photo of fibers (left); fiber fragments in reconstructed micro-CT image [20].**
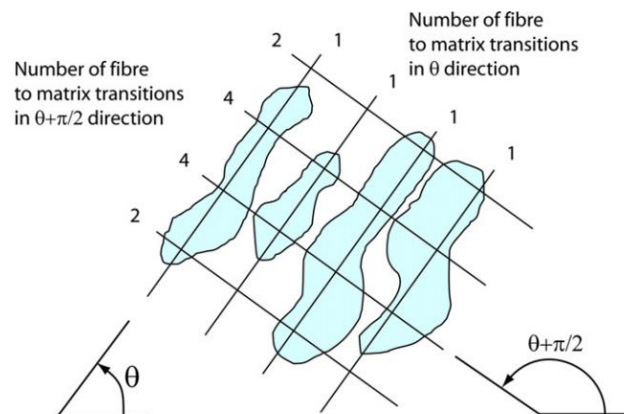


**Figure 1-6. An example of phase transitions counting two rotations with perpendicular grid**

**lines [21].**

Consequently, the X-ray micro-CT methods that can provide higher accuracy on the global characterization of internal geometry are adopted in the present study.

The X-ray micro-CT researches of fiber reinforced composite materials, however, were mainly concentrated on the injection molding compound [3, 21, 27-30], laminates [31-33] and woven fabric composites [23, 24, 34, 35]. The distribution of injection molded natural fiber morphologies embedded in PP matrix was studied by Alemdar et al. [27], in which 3D models were generated to characterize the fiber length and fiber width distributions. Local average orientation distribution and visualized 3D orientation modeling of GF (glass fiber) /PA6 injection materials were investigated by Bernasconi et al. [21] using the MIL technique. Fiber orientation and effect of injection flow on injecting molded glass fiber reinforced nylon (GF/PA6) and carbon fiber reinforced polypropylene (CF/PP) were analyzed respectively [29, 30]. The orientation distribution together with local volume fraction of CF/Aluminum and CF/epoxy unidirectional laminates were investigated through 3D micro-CT method [31]. 2D laminated preform and random felt carbon-carbon composites were fabricated, and studied by Dietrich et al. focusing on the distribution of the fibers, porosity and other internal geometries [32]. The porosity of CF/epoxy laminates were also studied and the X-ray micro-CT aided mechanical simulations were conducted by Tserpes et al. [33]. The internal geometries of carbon woven fabric [24] and woven textile CF/epoxy composites [23] were analyzed using a structural tensor based micro-CT method. The combination of the reconstructed 3D model of both short fiber composites and textile composites with the FE mesh generation and numerical analysis have been reported [28, 34].

Among the previous studies on X-ray micro-CT, we found only limited researches reported the internal geometry analysis of DCFRTP. The dominate research objects in X-ray micro-CT studies are the continuous fiber systems like laminates and woven textiles. Few people conducted the orientation and fiber morphology examinations on injection molded DCFRTP. However, concerning the fiber mats and ROS composites, scarcely studies can be found related to the X-ray micro-CT analysis. The reason of this situation is considered to be caused by the facility limitations. The X-ray facilities up-to-date still cannot provide large scan volume with required resolution (general in millimeter-scale volumes with micrometer resolution to identify fibers). While the traditional short fiber composites or textile fabric composites generally have structural periodic boundary conditions as illustrated in Figure 1-7 and the size of representative volume element (RVE), the smallest volume that can represent the globe internal geometry properties of

the corresponding material, is relatively small compared with the observation capability of X-ray facilities. Hence the internal geometry analysis of continuous fiber systems and injection molding are feasible to conduct directly with the existent experimental methods. On the other hand, the fiber length in fiber mats and the strands size of ROS are generally several millimeters to tens millimeters, therefore the RVE of these composites are also in tens millimeter scale, which is larger than maximum scan volume of X-ray facility with required resolution (3 to 4 μm as the radius of carbon fiber).

Consequently, the reason why there is almost no report concerning the internal geometry analysis of fiber mats and ROS composites with X-ray micro-CT methods is caused by the fact that the limitation of current X-ray facilities may lead to lack of significance and accuracy of acquired data, and the simulation results may show as just stochastic states from different locations of materials.
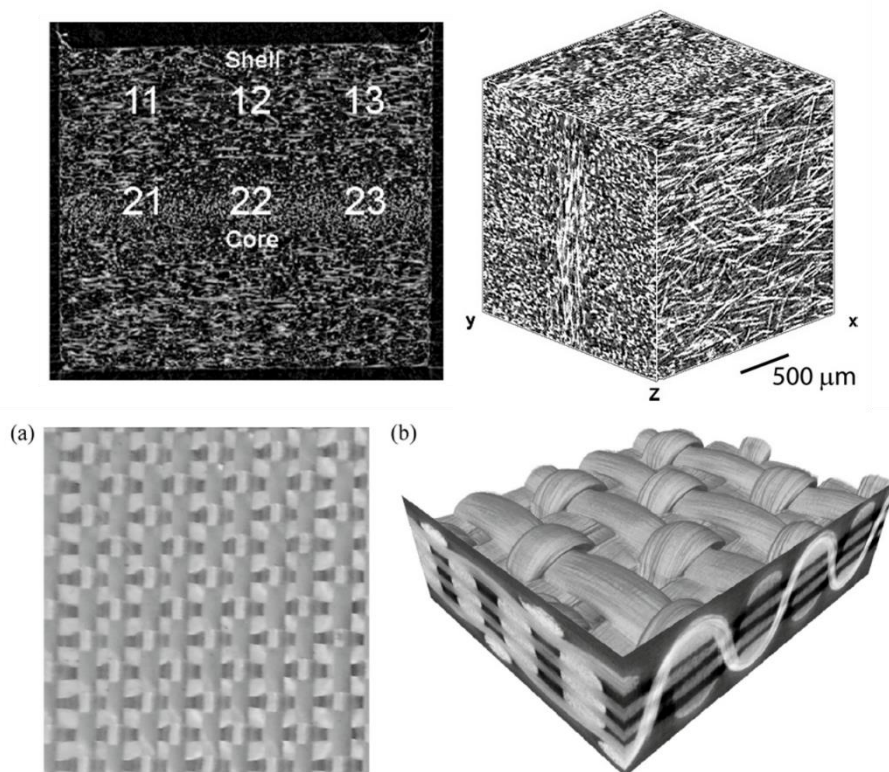


**Figure 1-7. Reconstructed cross-section and 3D model of injection molded composites (fiber length between 200 μm to 300 μm) [21] (up); reconstructed cross-section and 3D model of 3D orthogonal non-crimp woven fabric [34] (down).**

### 1.2.2.  Mechanical property characterizations

The characterizations of mechanical properties of DCFRTP were developed in decades. The main concept of characterizations is focusing on the "homogenization" because the calculation capabilities are generally restricted by the structural complexity and the attendant sophisticated interactions between the reinforcements and the matrix.

One of the mainstream approaches to predict the modulus and strength of DCFRTP is the modified rule of mixtures (MROM) [36-47]. In this method, the mechanical properties of the composites are considered to be the simple combination of matrix properties and fiber properties with their weight coefficients (volume ratio), and adding additional factors on fiber properties based on the orientation and fiber length effects (matrix is considered as isotropic). Cox provided the analytical model based on the concept of MROM to calculate the modulus of short fiber composites [36]:

$$E_{11} = E_f \left[ 1 - \frac{\tanh(\beta l/2)}{\beta l/2} \right] V_f + E_m (1 - V_f) \qquad \textbf{Equation 1-4}$$

where $E_{11}$ is the longitudinal modulus of the composite, $E_f$ and $E_m$ are the elastic modulus of the fibers and the matrix, respectively. $\beta$ is given by Equation 1-5 [48]:

$$\beta = \left[ \frac{2\pi G_m}{E_f (\pi r_f{}^2) \ln(R/r_f)} \right] \qquad \textbf{Equation 1-5}$$

where $G_m$ is the shear modulus of the matrix, $r_f$ is the radius of the fibers and $R$ is the mean separation of the fibers normal to their length. Also the transverse modulus and the in-plane shear modulus, $E_{22}$ and $G_{12}$ also could be calculated through the Halpin-Tsai equations [37, 38]:

$$E_{22} = E_m \frac{(1 + 2\eta_1 V_f)}{(1 - \eta_1 V_f)} \qquad \textbf{Equation 1-6}$$

$$G_{22} = G_m \frac{(1 + \eta_2 V_f)}{(1 - \eta_2 V_f)} \qquad \textbf{Equation 1-7}$$

where

$$\eta_1 = \frac{\left( \frac{E_f}{E_m} - 1 \right)}{\left( \frac{E_f}{E_m} + 2 \right)} \qquad \textbf{Equation 1-8}$$

$$\eta_2 = \frac{\left(\dfrac{G_f}{G_m} - 1\right)}{\left(\dfrac{G_f}{G_m} + 1\right)}$$

**Equation 1-9**

where $G_f$ is the shear modulus of the fibers.

A more general equation based on MROM is given by Fu with the consideration of fiber orientation, fiber length distribution and bridging stress of fibers [39]:

$$\sigma_C = \chi_1 \chi_2 V_f \sigma_f + V_m \sigma_m$$

**Equation 1-10**

where

$$\chi_1 \chi_2 = \int_{\theta_{min}}^{\theta_{max}} \int_{L_{min}}^{L_{c0}} f(L) g(\theta) \left(\frac{L}{L_{mean}}\right) \left(\frac{L}{2L_c}\right) \exp(\mu\theta) \mathrm{d}L \mathrm{d}\theta$$

$$+ \int_{\theta_{min}}^{\theta_{max}} \int_{L_{min}}^{L_{c0}} f(L) g(\theta) \left(\frac{L}{L_{mean}}\right) (1 - A \tan\theta)$$

**Equation 1-11**

$$\times \frac{\left(1 - L_c(1 - A \tan\theta)\right)}{\left(2L \exp(\mu\theta)\right)} \mathrm{d}L \mathrm{d}\theta$$

The $\sigma_C$ is the strength of the composite. $\chi_1$ and $\chi_2$ are respectively, the fiber orientation and fiber length factors, and the product of $\chi_1$ and $\chi_2$, i.e. $\chi_1 \chi_2$, is the fiber efficiency factor for the strength of the composite. $L$ is the fiber length and $L_{mean}$ and $L_c$ are the mean fiber length (i.e. the number average fiber length) and the critical fiber length, respectively. $\theta$ is the fiber orientation angle and the $\mu$ is the snubbing friction coefficient between fiber and matrix at the crossing point, which has been defined elsewhere [49, 50]. $f(L)$ and $g(\theta)$ are fiber length probability densify function and fiber orientation density function, respectively. $f(L)$ is given by a two-parameter Weibull distribution function [51]:

$$f(L) = \left(\frac{m}{n}\right) \left(\frac{L}{n}\right)^{m-1} \exp\left[-\left(\frac{L}{n}\right)^m\right] \text{ for } L > 0$$

**Equation 1-12**

where $m$ and $n$ are shape parameters. $g(\theta)$ is set up with a two-parameter exponential function [52]:

$$g(\theta) = \frac{(\sin\theta)^{2p-1}(\cos\theta)^{2q-1}}{\int_{\theta_{min}}^{\theta_{max}} (\sin\theta)^{2p-1}(\cos\theta)^{2q-1} \mathrm{d}\theta}$$

**Equation 1-13**

where $p$ and $q$ are the shape parameters which can be used to determine the shape of the distribution curve, and $p \geq 1/2$ and $q \geq 1/2$. Also, $0 \leq \theta_{min} \leq \theta \leq \theta_{max} \leq \pi/2$.

However, the further development of MROM is restricted in the field of DCFRTP because the components (fibers and matrix) are independent in this method and the additional factors concerning internal geometries can only affect the fibers part (the matrix is considered to be constant and isotropic). In addition, the expansibility for more accuracy modeling of the internal geometries is also limited by the simple combination of the structural factors in this method. Consequently, this conception can result in considerable average value under simple situations (unidirectional composites, randomly fibers with very low volume fraction, etc.), but for the fiber mats with high volume fractions and long fiber length, as well as the ROS composite with extremely high fiber volume fractions and multi-scale internal geometries, the MROM is considered powerless.

The ROS have noticeable internal geometries that are highly heterogeneous and with localized anisotropy due to the large strand dimensions and random orientations. These characteristics are also shared by the fiber mats composites although the macroscopic effect of the heterogeneous microstructure is reduced because of the smaller distribution fibers.

Methods different from MROM are developed to predict the mechanical properties of ROS and fiber mats composites. The equivalent laminate analogy is considered to be an efficient method to account for the randomly oriented architecture of the fibers or strands [53-65]. The equivalent laminate assumption represents the random orientations of discontinuous composites into a ply-by-ply equivalent laminate, which contains unidirectional discontinuous plies at different orientations and forming a (generally quasi-isotropic) lay-up laminate (Figure 1-8). To conduct the simulation, the classical laminate theory is generally introduced in the lay-up processes to combine the properties of each equivalent layer. To calculate the equivalent layers that can represent the randomly fibers and strands, micromechanics like shear-lag theory [66] and mean-filed homogenization [67] together with the finite element method (Figure 1-9) [57] are generally considered. Concerning the finite element method have a similar feature with the MROM that the accurate internal geometry properties are difficult to be imported (high accuracy of finite element model needs numerous of calculation capability), the more efficient micromechanics are adopted in the present research.
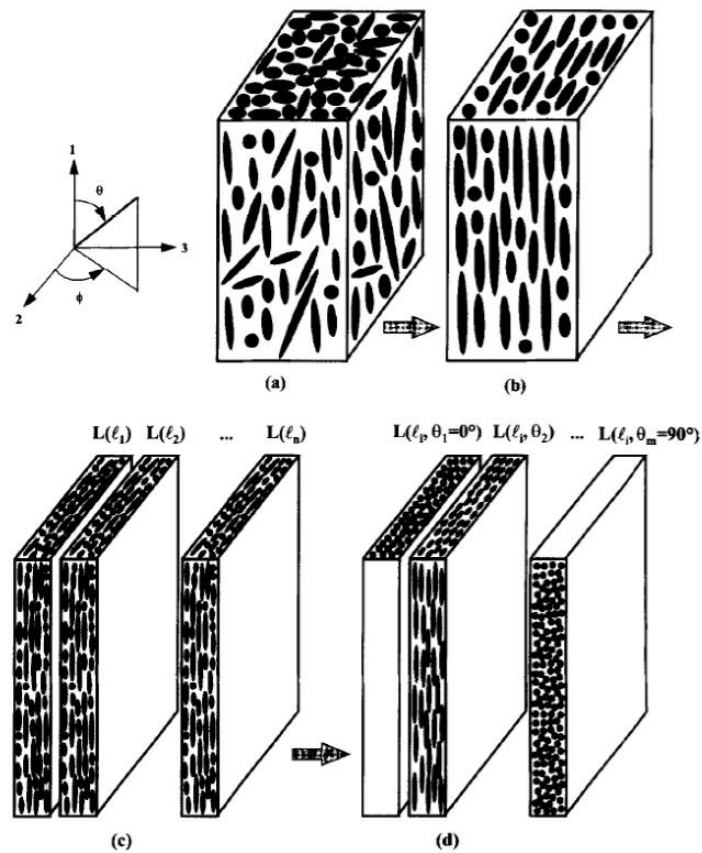
**Figure 1-8. Simulated progress of the equivalent laminate analogy of a 3D, misaligned short-fiber-reinforced polymer composite: (a) the real 3D DCFRP, (b) the supposed DCFRP, (c) the supposed DCFRP is considered as combination of laminates, each laminate has the same fiber length and (d) each laminate is treated as a stacked sequence of laminate, each lamina has the same fiber length and the same fiber orientation [58]**
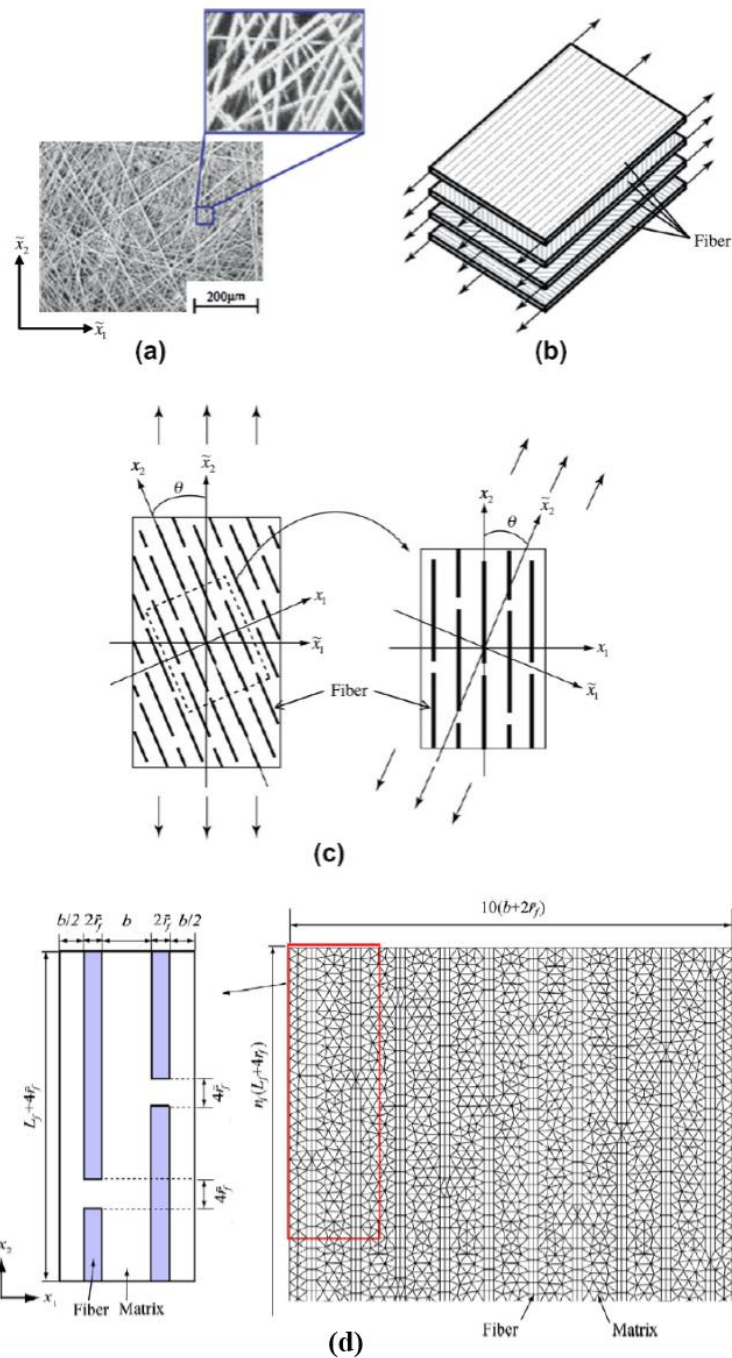
**Figure 1-9. Schematic of the equivalent laminate analogy of fiber mat composites; (a) fiber orientation in composite, (b) stack of plies, (c) coordinate transformation, (d) unit cell finite element model [57].**

Apart from the equivalent laminate analogy, developments in micromechanics provided additional possibilities to predict mechanical properties of ROS and fiber mats composites with

complex internal geometries.

Historically, shear-lag models were the first micromechanics model for the simulation of discontinuities in the reinforcement of composites and to examine behavior near the ends of broken fibers in continuous fiber composites [36, 46, 56, 68, 69]. The shear-lag analysis focuses on a single fiber of length $l$ and radius $r_f$ and embedded in a concentric cylindrical shell of matrix having radius $R$. The fiber axial equilibrium requires:

$$\frac{d\sigma_{11}^f}{dx} = -\frac{2\tau_{rx}}{r_f}$$

**Equation 1-14**

where $x$ is the fiber direction, $\tau_{rx}$ is the axial shear stress at fiber surface. Based on the assumption in shear-lag given by Cox [36] that $\tau_{rx}$ is proportional to the difference in displacement $w$ between the fiber surface and the outer matrix surface:

$$\tau_{rx}(x) = \frac{H}{2\pi r_f}\left[w(R, x) - w(r_f, x)\right]$$

**Equation 1-15**

where $H$ is a constant depending on matrix properties and fiber volume fraction. Combine Equation 1-14 and Equation 1-15, the average fiber stress is:

$$\bar{\sigma}_{11}^f = E_f \bar{\varepsilon}_{11}\left[1 - \frac{tanh\left(\frac{\beta l}{2}\right)}{\left(\frac{\beta l}{2}\right)}\right]$$

**Equation 1-16**

where

$$\beta^2 = \frac{H}{\pi r_f^2 E_f}$$

**Equation 1-17**

For convenient, Equation 1-16 is also expressed as:

$$\bar{\varepsilon}_{11}^f = \alpha_l \bar{\varepsilon}_{11}$$

**Equation 1-18**

where $\alpha_l$ is considered to be length-dependent efficiency factor (similar with the $\chi_2$ in Equation 1-10). Consequently the shear-lage method is usually completed by combing with the MROM for the axial modulus:

$$E_{11} = \alpha_l V_f E_f + V_m E_m$$

**Equation 1-19**

However, the shear-lag methods exhibit inability on the solutions when facing to the highly

heterogeneous composites, and the mean-filed homogenization methods based on Eshelby's equivalent inclusion are developed to fill the gap in the analytical simulations of discontinuous fiber reinforced composites.

The self-consistent model and Mori-Tanaka model are the most adopted Eshelby's equivalent inclusion based micromechanics for the prediction of mechanical properties of discontinuous fiber reinforced composites. The self-consistent model approach is generally credited to Hill [70] and Budiansky [71], whose original work focused on spherical particles and continuous, aligned fibers. The application to short fiber composites was developed by Laws and McLaughlin [72] and by Chou, Nomura and Taya [73]. On the other hand, the Mori-Tanaka model is originally established by Mori and Tanaka [74] and Benveniste [75] provided a particularly simple and clear explanation of Mori-Tanaka approach and modified it to ensure the application of discontinuous fiber reinforced composites. Compared with the Mori-Tanaka method, the self-consistent model needs iterative calculation to approximate the self-consistent strain-concentration tensor $A^{SC}$ and considered less efficient [69]. Consequently, the Mori-Tanaka model is selected for the analytical simulation of DCFRTP and the detailed theoretical fundaments and algorithms are introduced in the section 3.3. However, some previous researches reported that mean-filed homogenization methods demonstrated overestimation of DCFRTP when the fiber volume fraction is over 20% [76] and the aspect ratio is over 100 (Figure 1-10) [77]. But this conclusion is only verified by finite element model and comprehensive experimental verification with the corresponding simulation is still required at present.
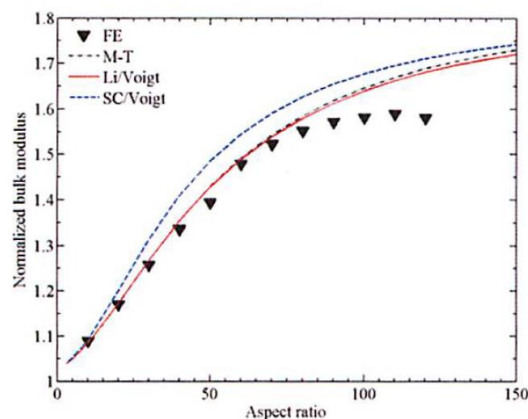


**Figure 1-10. The bulk modulus of random fiber composites at 2% fiber volume fraction with different fiber aspect ratio [77].**

## 1.3.  Problems and difficulties

DCFRTP, especially the ROS and fiber mats with long fiber length composited with complexed internal geometries that are highly heterogeneous with localized anisotropy. The internal geometry analysis of relative materials is restricted by the limitation of X-ray facilities and algorithms to prove the significance of scanned images. There is still no X-ray micro-CT method that can provide credible internal geometry properties of DCFRTP. With the increased interests on the DCFRTP in both the aspects of material researches and industrial applications, this becomes a crucial problem at present.

Simultaneously, the complexed internal geometries of DCFRTP bring the numerical finite element modeling analysis of these materials to only the theoretical feasibility and the practical simulation with the consideration of detailed inner structures will cause extremely high computing power and time-consuming modeling. However, analytical modeling methods like mean-filed homogenizations and equivalent laminate also show some limitations based on the previous researches. The development and verification of simulation methods with considerable accuracy and efficiency are urgently required for not only the applications but also theory establishments of DCFRTP.

## 1.4.  Research objectives

The final objective of my Doctor thesis is aiming at the feasibility of mass-production applications of DCFRTP in the automotive industry and the comprehensive characterization of internal geometries and mechanical properties of DCFRTP. As a newly developed researches filed, comprehensive knowledge is needed for the characterization of DCFRTP. To achieve this goal, the performances and reliability of DCFRTP must be verified in detail firstly. Concerning the verification of performances and reliability of one material, the careful evaluation of the structural and mechanical properties as well as the CAE capability for property predictions are regarded as the dominant approaches. Consequently, reliable and efficient methodologies are required for the comprehensive study of the internal geometry evaluations as well as the mechanical property characterizations of DCFRTP.

This thesis is mainly constituted of two subjects corresponding to Chapter 2 and Chapter 3. In addition, Chapter 1 gives a general introduction on the background and relevant researches, Chapter 4 summarizes the outputs from these investigations.

In Chapter 2, the internal geometries of DCFRTP are analyzed. Two different X-ray micro-CT methodologies purposing for accurate fiber orientation quantification and microstructure visualization of DCFRTP in different fabricating processes and components were developed. One methodology is named "VoxTex" based on the "voxel model" and structure tensors to conduct the micro scale computed tomography. Another methodology is called "TRI/3D-BON" and developed with the image binarization processing combined with the MIL concept with the X-ray scanned images. Multi-scale internal geometry analyses were conducted to investigate the structural features of DCFRTP in fiber-, layer- and macro-level. Limitations and restrictions of X-ray facilities on the X-ray analysis of DCFRTP were discussed in detail and solved statistically in the present study. The relationships between the internal geometry and fabricating properties like molding conditions and component sizes were revealed quantifiably. The internal geometry properties like orientation tensors and layered orientation distributions were collected from the two X-ray micro-CT methodologies to achieve precise descriptions of DCFRTP.

In Chapter 3, the mechanical properties of DCFRTP are evaluated. Two different analytical simulation methods and experiments were applied to evaluate the tensile properties of DCFRTP in different fabricating processes and components. One method is the general mean-filed homogenization Mori-Tanaka method. Another one is the equivalent laminate method (as called "de-homogenization" method) based on the combination of classical laminate theory with composite micromechanics. The simulation results were compared with the experimental values to clarify the capability and advantages of each method. In the Mori-Tanaka method, the fiber orientation tensors of the DCFRTP calculated from 3D-BON X-ray micro-CT were applied into the modeling processes. In the equivalent laminate method, the internal geometry properties (out-of-waviness, for instance) collected from the VoxTex X-ray micro-CT were input to the models of DCFRTP. The aspect ratio of reinforcements and components properties were also studied in detail to increase the accuracy and reliability of simulations.

The entire picture of DCFRTP potential on both the material research side and industrial application side was captured with the studies on the internal geometries and mechanical properties. The combination of novel methodologies developed in the X-ray micro-CT and the analytical simulation models for mechanical property predictions open the new ways not only for comprehensive solution methodologies of DCFRTP analyses but also criterions and suggestions of DCFRTP applications.

## 1.5. Object materials

To give a comprehensive investigation on the internal geometries and mechanical properties, two kinds of DCFRTP with different components and fabrication processes were prepared in this research.

One is carbon fiber mats reinforced thermoplastics (CMT), which is composed of acid-modified polypropylene (PP) films and paper-like randomly orientated carbon fiber monofilaments. The PP used in this material is acid-modified and developed in our project; the carbon fibers in CMT are the T700 from Toray and the fiber length before molding is 6mm in average. The surface appearance of CMT materials is illustrated in Figure 1-11, and regarded as the general DCFRTP, the structural schematic of CMT is shown in Figure 1-12. In this study, two different kinds of CMT, named as CMT-1 and CMT-2 that differ on their fiber volume fraction ($V_f$), are applied. The CMT-1 are regarded to have $V_f = 10\%$ and CMT-2 have $V_f = 20\%$. The CMT materials were manufactured and provided by Toray Industries, Inc.
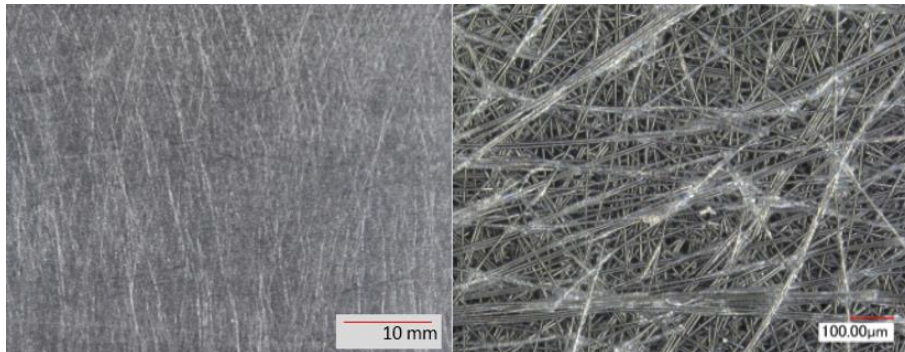


**Figure 1-11. Carbon fiber mats reinforced thermoplastics (CMT).**
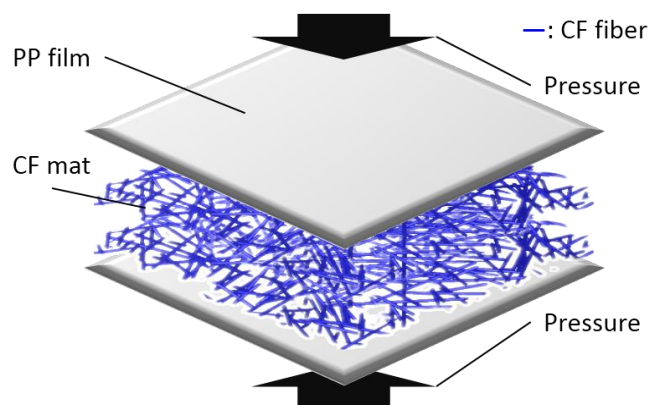
**Figure 1-12. The schematics of the CMT.**

Different from the traditional DCFRTP, another one is a kind of ROS named chopped carbon fiber tapes reinforced thermoplastics (CTT). The CTT is composed with randomly oriented unidirectional pre-impregnated tapes, and as a new serious of composites, this study will mainly focus on the CTT materials and the CMT are regarded as the comparison items. The tapes are cut off from pre-impregnated sheet, which is provided by the Industrial Technology Center of Fukui Prefecture in Japan. The pre-impregnated sheet is manufactured with carbon fiber (TR 50S, Mitsubishi Rayon Co., LTD.) and Polyamid-6 (PA6, DIAMIRON™ C, Mitsubishi Plastics, Inc.). To manufacture the tape, the carbon fiber tows were first opened and lined up. Then the lined carbon fibers were heated and compressed with the PA 6 films. At last the impregnated sheets were cut into certain sizes as the pre-impregnated tape. The pre-impregnated sheets have a averaged $V_f$ around 55%. The manufacturing process of the UT sheet is shown in the Figure 1-13.

Different tape shapes are selected in CTT to give a comprehensive study on the effect of tape morphology. Five different tape lengths (6 mm, 12 mm, 18 mm, 24 mm and 30 mm) (Figure 1-14) and three different tape thicknesses (44μm, 88μm, 132μm) (Figure 1-15) are cut from the pre-impregnated sheets. The width of tapes cut from the pre-impregnated sheet is fixed to 5 mm. For convenience, the CTT with different tape lengths are named as CTT-6, CTT-12, CTT-18, CTT-24 and CTT-30, and the CTT with different thicknesses are named as CTT-Thin (44μm), CTT-Med (88μm) and CTT-Thick (132μm). Among them, the thickness of CTT-thin pre-impregnated sheet is much thinner compared with the conventional pre-impregnated sheet (about 150 μm or more). Due to the thin-layer effect, the CTT-Thin is regarded as the main object material in this study, hence the CTT-Thin is referred further as "CTT" with no fixes.
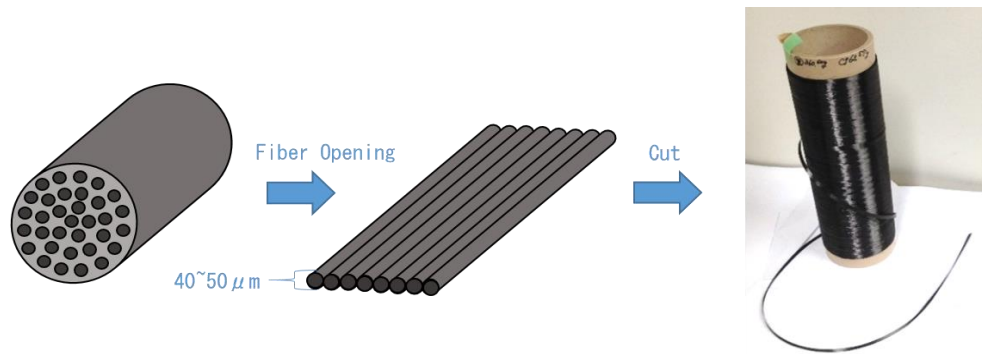
**Figure 1-13. The manufacturing process of the UT tape.**
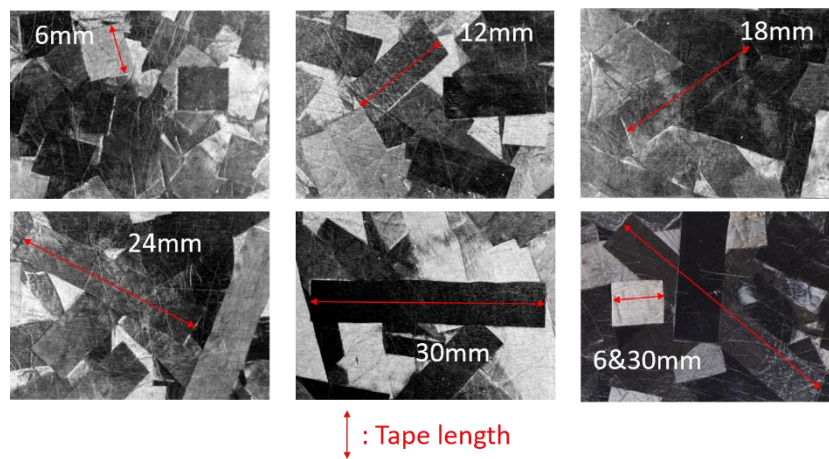


**Figure 1-14. CTT with different tape lengths.**

Thickness: 44 µm        Thickness: 88 µm        Thickness: 132 µm

CTT(Thin)        CTT(Med)        CTT(Thick)
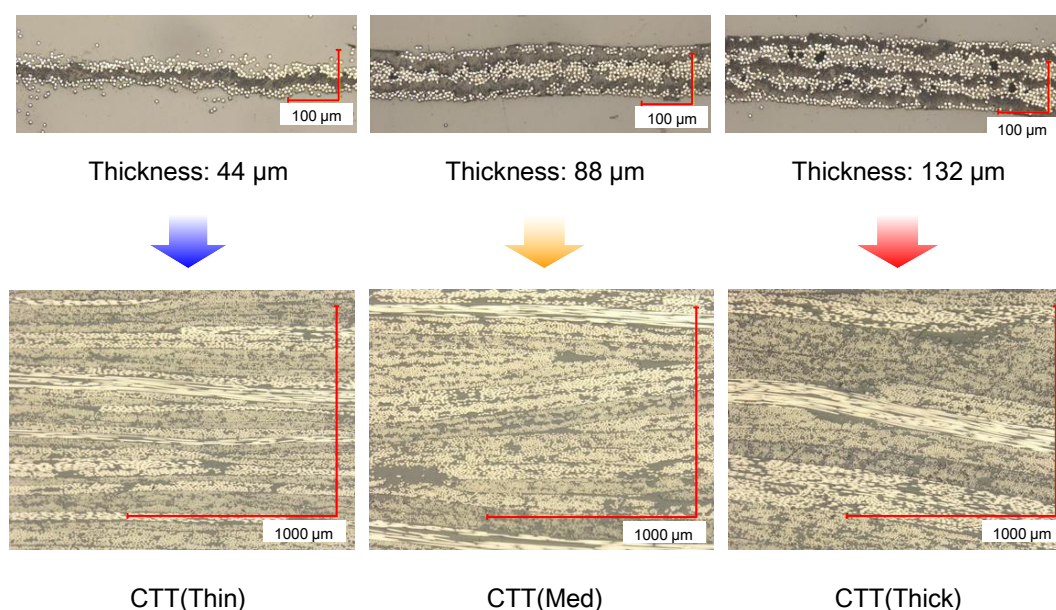
**Figure 1-15. Cross section of pre-impregnated sheets with different thicknesses [78].**

Generally, there are two different fabricating methods to manufacture ROS-alike CTT materials (Figure 1-16). One is the general method to put the chopped tapes into the mold, heat up and conduct compression molding, which is named bulk molding CTT (BM-CTT). On the other hand, the other fabricating method added additional processes to ensure a better in-plane even distribution of the tapes and to preserve the tape structure after molding. To ensure this better distribution, a wet-type sheet making process were introduced. In the process, the obtained discontinuous tapes were collected and placed inside a water-filled container with a filter and an aperture on the bottom side. After the tapes were randomly dispersed, the aperture was opened to remove the water from the container. Then, the CTT sheets were temporarily fixed by heating and cooling hand presses under two procedures: firstly, under 90 degree Celsius and 0.1 MPa pressure for 1 min to remove the water; secondly, under 230 degree Celsius and 0.5 MPa pressure for 1 min to temporarily fix the sheet. Because of the high water absorption of PA6, the CTT sheets were put into a vacuum dryer before molding. The temperature of the dryer was set to 90 degree Celsius and the sheets were vacuuming for 12 hours before the sheets were stacked and molded. The CTT sheets are stacked to manufacture CTT plates with 2 mm thickness using compression molding. Because of this wet-type sheet making process, the CTT fabricated with the second method is named as sheet molding CTT (SM-CTT). Because the purpose of the present research aimed at the characterization of the internal geometry and mechanical property of CTT as well as

23

their relation with the tape scale, so the repeatability and reliability of the CTT and their fabricating process is very important. Consequently, only the wet-type sheet making process, i.e., SM-CTT, that have better in-plane even tape distribution and tape structure after molding will be selected for this study (Figure 1-17).
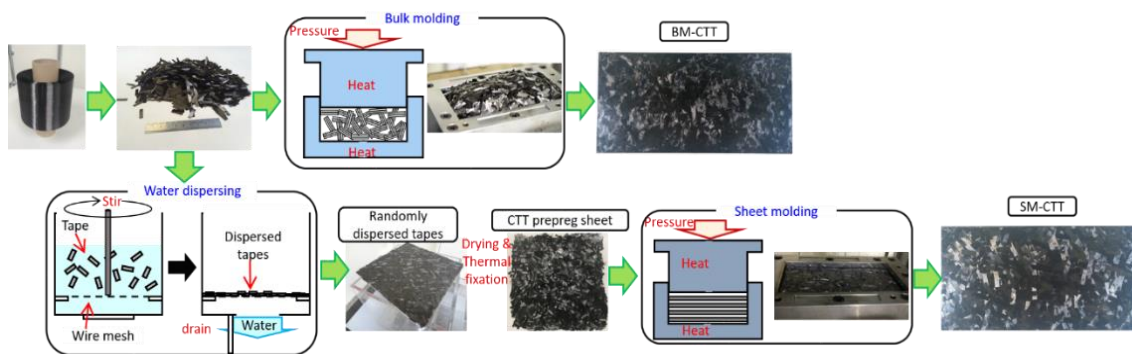


**Figure 1-16. Fabricating processes of bulk molding CTT (BM-CTT) and sheet molding CTT (SM-CTT).**

In the compression molding processes, three different molding pressure are applied in this study to identify the capability of applied analysis method on CTT. The first molding condition is regarded as the general condition with the highest pressure during molding in 5 MPa (the 5 MPa molded CTT are named with no additional prefixes and suffixes). To verify the effect of molding pressure on properties of CTT, two comparison molding pressures are also introduced and labeled as high pressure molding with 10 MPa molding pressure ($M_{10}$ CTT) and low pressure molding with 3 MPa molding pressure ($M_3$ CTT). The CTT are molded using a 30t automatic hydraulic press machine (Pinette Emidecau Industries Co., Ltd), and the molding conditions are plotted in Figure 1-18 (5 MPa molding pressure) and Figure 1-19 ($M_3$ and $M_{10}$). Both the low and high molding pressures give the CTT plates visible effects after molding. After 5 MPa molding and $M_{10}$ molding, the CF impregnation quality was very good since the CF tape surface was entirely covered by the polymer matrix. In contrast, the impregnation quality of the material surface obtained by $M_3$ molding was not as good since some tape parts were not fully covered with the polymer species, making the CF surface partially exposed (Figure 1-20 and Figure 1-21). After the CTT plates are molded, each edge of the plates is cut off by 15 mm to eliminate the molding edge effect, and the plates will be cut to specific shapes for corresponding studies.
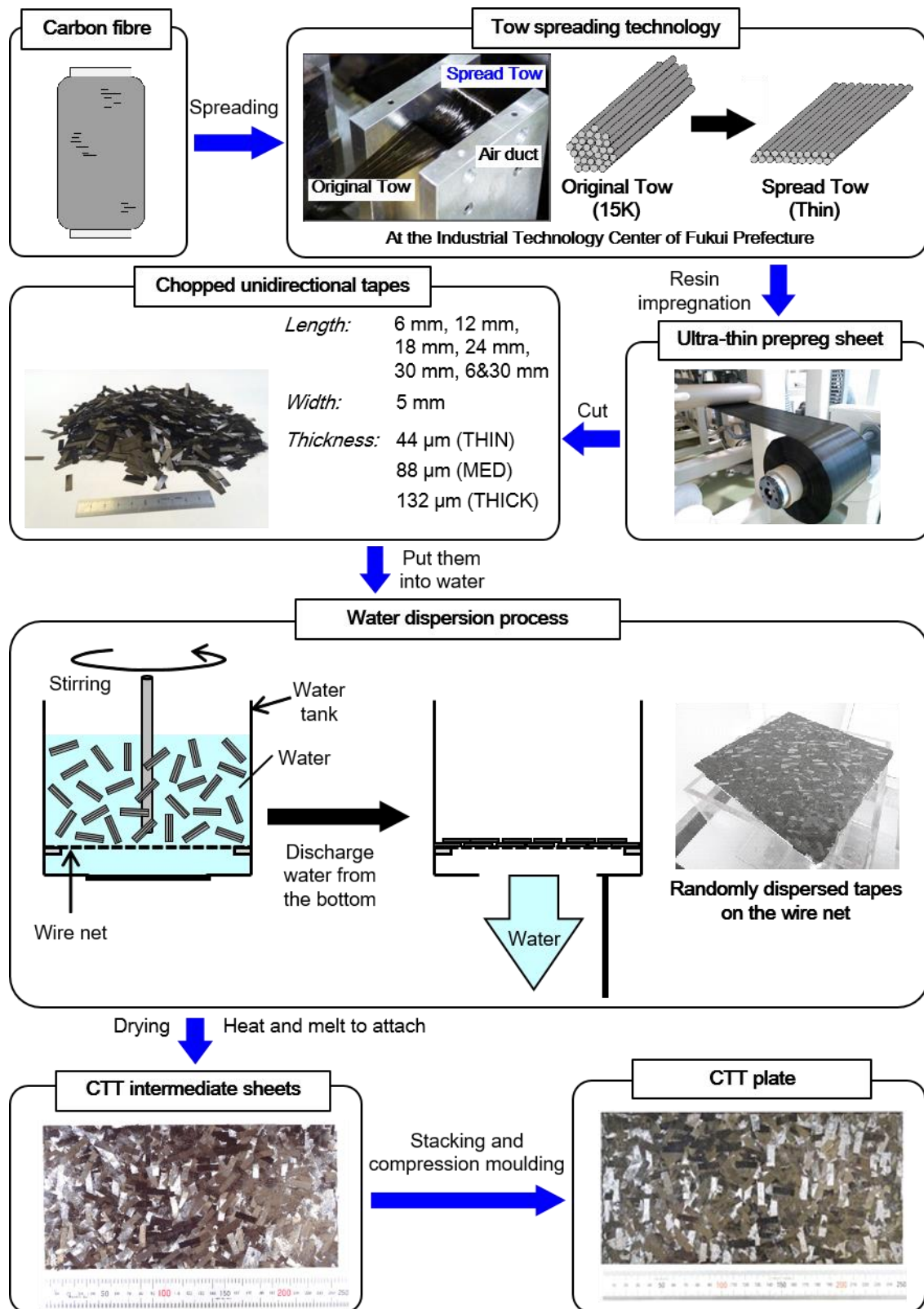
**Figure 1-17. Fabricating processes to manufacture the SM-CTT used in present study [78].**
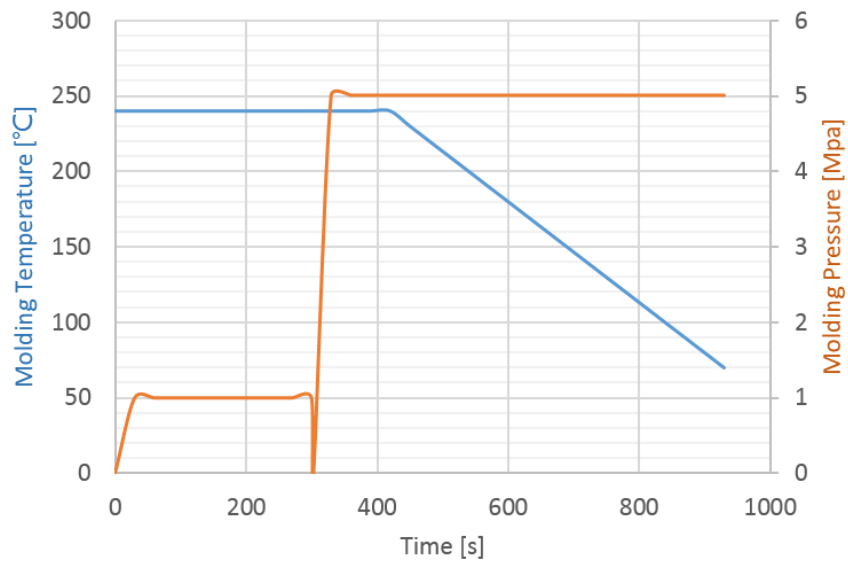
**Figure 1-18. Molding condition of 5 MPa pressure process.**
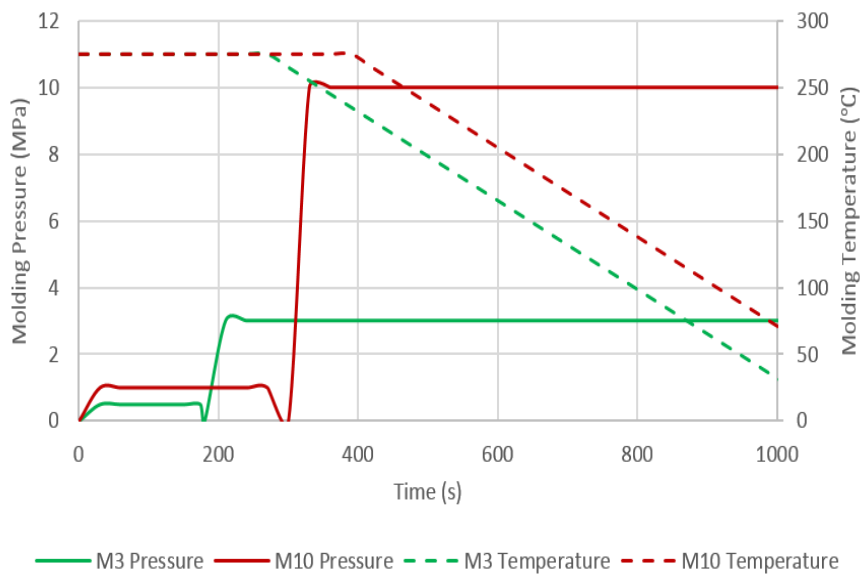


**Figure 1-19. Molding conditions of 3 MPa and 10 MPa pressure processes.**
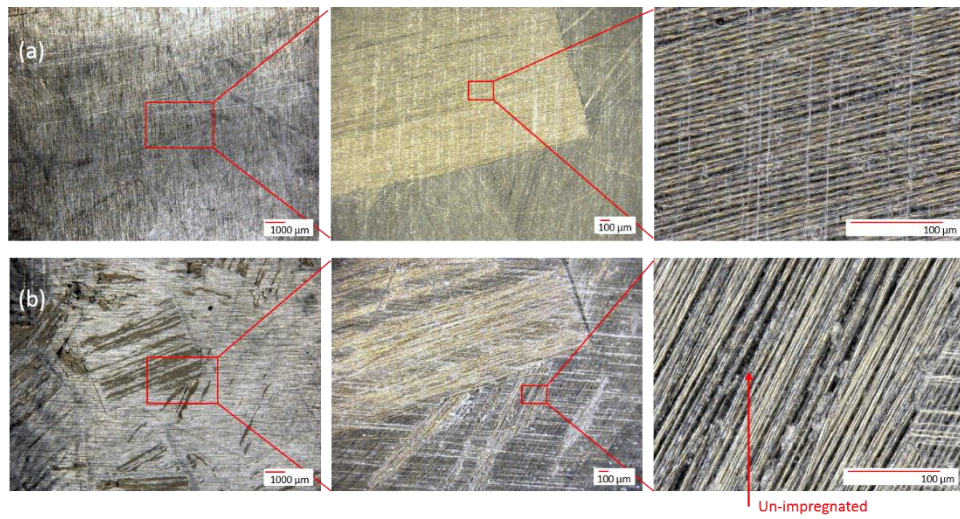
**Figure 1-20. Micrographs of CTT-6 fabricated under $M_3$ (a) and $M_{10}$ (b) conditions.**
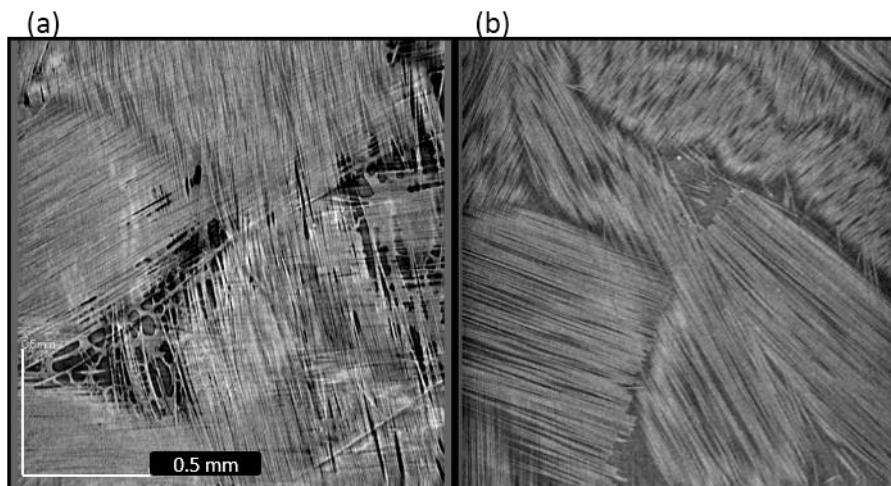


**Figure 1-21. X-ray micro-CT images of the poor impregnation of $M_3$ specimen (a) and the general $M_{10}$ specimen (b).**

# Chapter 2.   Internal Geometries

## 2.1.  Introduction

In chapter 2, the internal geometries of DCFRTP are analyzed.

As reviewed in the Chapter 1, few researches have been done concerning about the internal geometry analysis of CMT and CTT due to the limitations of X-ray facilities to observe considerable volumes including the long fiber lengths of these composites to ensure the analysis significance.

In this chapter, the internal geometry properties of CMT and CTT are studied in detail with the consideration of the X-ray scanning volume problem. Statistical method is developed to solve this problem. Two different X-ray micro-CT methodologies are applied to CMT and CTT to compare the capabilities in terms of internal geometry quantifications and visualizations. The internal geometry properties collected from both X-ray micro-CT methods are organized for further

application of material modeling.

## 2.2. Specimens

To conduct the X-ray micro-CT analysis of CTT and CMT, the size of specimens are restricted by the X-ray facilities and image processing techniques.

Generally, to ensure an adequate fiber-level orientation analysis, the images collected from the X-ray need a resolution higher than the radius of the object fiber (in the case of carbon fiber, 3.5μm in average). However, to ensure this resolution of the X-ray image, the X-ray scanner developed currently can just provide limited scan volume (generally in millimeter scale).

Consequently, to acquire the scan volume as large as possible, the specimens for X-ray scan should be prepared in a specific shape to ensure efficient scanning processes. In the present study, the specimens with a size of 2×2×30 mm (thickness × width × length) were cut from all the CTT plates using thin section cutting machine (EXAKT Advanced Technologies GmbH 310CP). In addition, to avoid the effect on uneven in-plane property, the specimens were cut from arbitrary positions of the plates.

## 2.3. Methods

To conduct comprehensive analyses of the internal geometries of both CTT and CMT, the X-ray scanning and two different micro-CT processes are applied in this study.

### 2.3.1. X-ray scanning

The internal structural information of CTT was observed and collected by the 3D X-ray scan system TDM1000-II from Yamato Scientific Co., Ltd. During the observation, the specimens were fixed on a rotational stage as shown in Figure 2-1. The distance between the rotation axis and the radiation source is set to 10 mm for reliable resolution of embedded fibers on the images. The scanned raw volume is a right circular cylinder after the scanning process because of the stage rotation, and the size of the cylinder is 0.88 mm in radius and 1.76 mm in height under setting condition. The pixel size of the reconstructed 3D micro-CT images was fixed to 3.4 μm,

and the scanned raw volume consisting of 512 stacked images through out-of-plane direction. To ensure sufficient image resolution and image contrast during CT acquisition processes, the air part of the scanned raw images were removed. In addition, the CT processes in the present study is conducted under the Cartesian coordinate system, so the volume for CT processes should be in a cube shape. Consequently, the sample was positioned in the scanner's field of view inscribed in the right circular cylinder, so that the imaged volume had a physical size of 1.1×1.1×1.1 mm and excluded the air surrounding the sample. The X-ray tube voltage was set to 40 kV and X-ray tube current was set to 40 μA for all the specimens. After the acquisition of the X-ray projection images (a rotation step of 0.24 degree and 25 minutes per full rotation of the sample), the 3D image was reconstructed by the image processing unit of the X-ray scan system and 325 images are stacked through the out-of-plane direction in each specimen for image processing and CT analysis. The X-ray scanning process is illustrated in Figure 2-2.
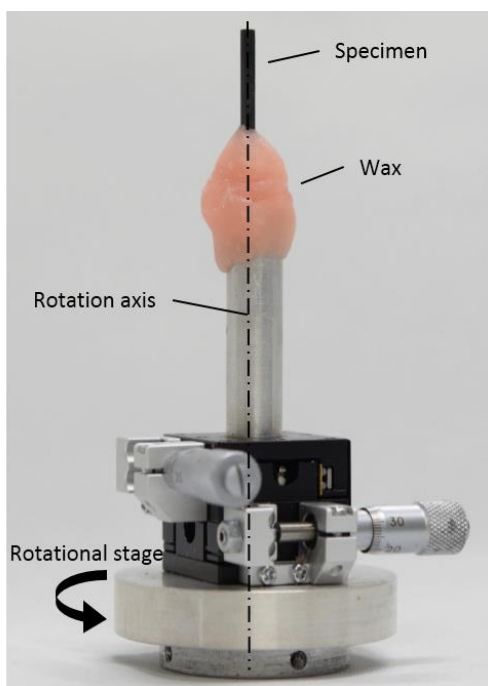


**Figure 2-1. X-ray scanning specimen on the rotational stage.**
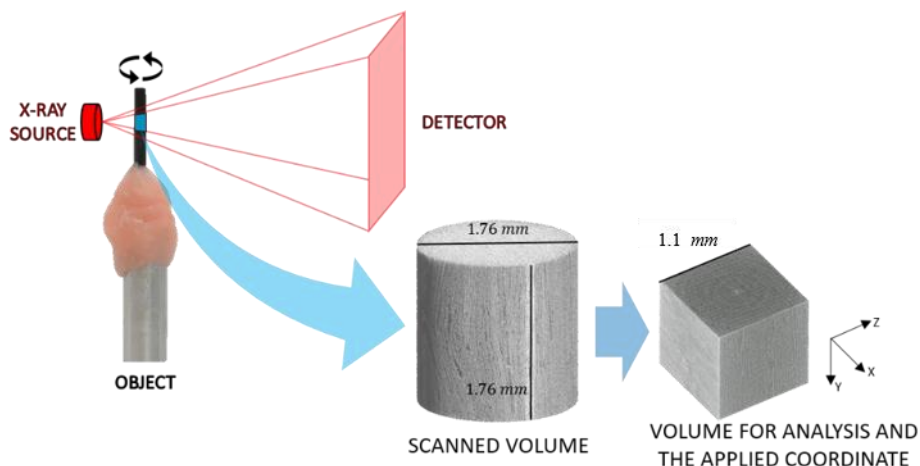
**Figure 2-2. Schematic of scanning process and scanned volume of CTT.**

### 2.3.2.   Image processing and data analysis

Two different CT image processing methods are introduced in the present research.

2.3.2.1.   VoxTex

The first method involved in this study is based on a software named VoxTex developed under my collaboration research with Dr. Ilya Straumit and Prof. Stepan V. Lomov from the Katholieke Universiteit Leuven (KULeuven), Belgium [19, 23, 24]. This software is still under developing currently and not available commercially.

The algorism of this method based on the "voxel model" and using structure tensor for the orientation quantification (Figure 2-3).

The term "voxel model" is used to designate a high-level description of the material's microstructure in this method. The usage of this term should not be confused with the micro-CT image used as a starting point for the model derivation, even if the image can also be described as an array of "voxels", containing grey-scale values only. The "voxel models" derived from the image can be different from it in two aspects: first, the dimensions of voxels in the model can

differ from the elements of the image, and second, voxels of the model contain physical rather than gray-scale information. The original micro-CT image, which can be stored as an image stack or a single file containing gray values, is converted into a single three-dimensional array of gray values with 256 levels (8 bit) of gradation. Further on, if not specified otherwise, the expression "micro-CT image" means this three-dimensional array of gray values. The term "voxel", which has two meanings in the context of this method: as a pixel of the three-dimensional image and as an element of voxel model, will be used mainly in its second meaning, except when it is used to define physical size of the voxels in the micro-CT image. According to the given definition of the voxel model, a voxel is a subdomain of the material's domain, with centroid coordinates, dimensions and associated vector of variables. Derivation of the voxel model from a three-dimensional micro-CT image involves partitioning of the image domain into subdomains, centered at the nodes of a regular lattice; calculation of the principal direction, the degree of anisotropy and the average grey value at each subdomain; and segmentation of the image domain into material components using the derived variables. Result of the segmentation is an additional integer value assigned to each voxel, which indicates its material type.

Density of the voxels in the voxel model can be chosen on the basis of a trade-off between the level of details required for final application (visualization, permeability, mechanical calculations), and computation time, which depends on the total number of voxels.

The internal geometry of the material was reconstructed from the CT image using a regular rectangular (voxel) mesh. The CT image is converted from the native scanner format to a single three-dimensional array $I(x_1, x_2, x_3)$ of 8-bit grey values where the coordinates $x_1, x_2, x_3$ are integer numbers. The analyzed variables are fiber orientation angles $\varphi$ and $\theta$ in spherical coordinate system. $\varphi$ is in-plane orientation axis, with the Cartesian axes $x_1$ and $x_2$ lying in the plane of the sheet, and $\theta$ is an angle of the vector with the axis $x_3$, normal to $x_1$ and $x_2$ axes. The fiber orientation vector is calculated using structure tensor from the CT image $I(x_1, x_2, x_3)$ as a solution of the following eigenvalue problem:

$$S(\boldsymbol{p}) = \int_{W(\boldsymbol{p})} S'(\boldsymbol{r}) dr \qquad \textbf{Equation 2-1}$$

$$S'(x_1, x_2, x_3) = \begin{bmatrix} \left(\dfrac{\partial I}{\partial x_1}\right)^2 & \dfrac{\partial I}{\partial x_1}\dfrac{\partial I}{\partial x_2} & \dfrac{\partial I}{\partial x_1}\dfrac{\partial I}{\partial x_3} \\ & \left(\dfrac{\partial I}{\partial x_2}\right)^2 & \dfrac{\partial I}{\partial x_2}\dfrac{\partial I}{\partial x_3} \\ sym & & \left(\dfrac{\partial I}{\partial x_3}\right)^2 \end{bmatrix} \qquad \textbf{Equation 2-2}$$

where $p$, $r$ are three-dimensional vectors and $W(p)$ is the window of integration, $W(p)$: $\forall\{x_1, x_2, x_3\}(|x_1 - p_1| \le w_r, |x_2 - p_2| \le w_r, |x_3 - p_3| \le w_r)$. The vector $p$ defines a current position of the integration window, whereas the $r$ vector with the components $(x_1, x_2, x_3)$ is a point in the image $I$ relative to the integration window. The $w_r$ parameter is discrete and is refereed further as window size. The actual size of the integration window is $2w_r + 1$ pixels. The size of the window can be larger, smaller, or equal to the distance between voxels. The derivatives in Equation 2-1 and Equation 2-2 are calculated using the 5-point central difference formula:

$$\frac{\partial I}{\partial x} = \frac{1}{12h}[I(x_1 - 2h, x_2, x_3) - 8I(x_1 - h, x_2, x_3) + 8I(x_1 + h, x_2, x_3) \qquad \textbf{Equation 2-3}$$
$$- I(x_1 + 2h, x_2, x_3)]$$

and similarly for the derivative by other coordinates. In a given coordinate system a structure tensor is represented by a 3×3 matrix. Eigenvalue decomposition of this matrix produces three eigenvalues $\{\lambda_1, \lambda_2, \lambda_3\}, \lambda_1 \le \lambda_2 \le \lambda_3$, and three corresponding eigenvectors $\{e_1, e_2, e_3\}$. The smallest eigenvalue indicates the minimum of variability of the microstructure, and the corresponding eigenvector indicates the direction in which this minimum is achieved. This direction is taken as a principal direction of the local fiber direction.

The integration is done over a local volume V of the CT image. The integration volume V has a cubical shape with a size of 17×17×17 pixels ($w_r = 8$). The eigenvector $e_1$ corresponding to the smallest eigenvalue $\lambda_1$ is the fiber orientation vector. The spherical angles were calculated from the eigenvector $e_1$ (unit vector):

$$\theta = arccos(e_{1,3}) \qquad \textbf{Equation 2-4}$$

$$\varphi = arctan\left(\frac{e_{1,2}}{e_{1,1}}\right) \qquad \textbf{Equation 2-5}$$

The voxel mesh therefore represents the two scalar fields $\theta(x_1, x_2, x_3)$ and $\varphi(x_1, x_2, x_3)$

defined over the spatial domain of the material sample, represented in the CT image. For the purposes of the present study, a special type of two-dimensional histograms was introduced, which includes the analyzed variable as one of the axes, and one of the spatial dimensions $(x_1, x_2, x_3)$ as the second axis of the histogram. A bin of this histogram shows frequency of occurrence of orientations in the range of the bin over a certain cross-section plane in the material. This type of histograms (further referred to as "unfolded" histogram) allows to represent the change of the distribution of a variable along a spatial coordinate. In this study it was applied to analyze through-thickness distribution of fiber orientations. The calculations using VoxTex were performed using C# code. Inside the code, two-dimensional histograms were rendered using Root Data Analysis Framework v 5.34 (CERN).
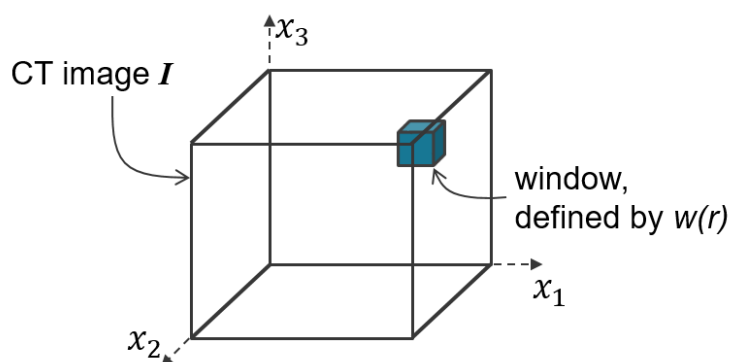


**Figure 2-3. Schematic of the VoxTex method and the "voxel model".**

### 2.3.2.2. TRI/3D-BON

The second method applied in this study using a commercialized software named TRI/3D-BON (RATOC System Engineering Co., Ltd.). The basic algorithm of this method based on the general image binarization process combines with the MIL concept. By setting the main plane (the material in-plane is regarded as the main plane in this study), the 3D model of the scanned X-ray images is rebuild, and the in-plane image is binarized based on the grey-scale values of the image Figure 2-4. The in-plane and out-of-plane orientation distribution and visualized meso-structure model of the X-ray scanned images were built by this software. Also, the orientation tensors of analyzing volumes were calculated based on the average in-plane and out-of-plane angle summarized by this software. The equation for orientation tensor calculation is [61]:

$$\boldsymbol{O} = \begin{bmatrix} cos^2\,\phi\,sin^2\,\theta & sin\,\phi\,cos\,\phi\,sin^2\,\theta & cos\,\phi\,sin\,\theta\,cos\,\theta \\ sin\,\phi\,cos\,\phi\,sin^2\,\theta & sin^2\,\phi\,sin^2\,\theta & sin\,\phi\,sin\,\theta\,cos\,\theta \\ cos\,\phi\,sin\,\theta\,cos\,\theta & sin\,\phi\,sin\,\theta\,cos\,\theta & cos^2\,\theta \end{bmatrix} \qquad \textbf{Equation 2-6}$$

where $\boldsymbol{O}$ denotes the orientation tensor, $\phi$ is the average in-plane angle and $\theta$ is the average out-of-plane angle of the materials Figure 2-5. The calculation of each vector in the $\boldsymbol{O}$ based on an integration of a function of the Euler angles:

$$\boldsymbol{a}_{ij} = \int_0^{2\pi}\int_0^{2\pi} \boldsymbol{p}_i\boldsymbol{p}_j\psi(\boldsymbol{p})d\boldsymbol{p} = \oint \boldsymbol{p}_i\boldsymbol{p}_j\psi(\boldsymbol{p})d\boldsymbol{p} \qquad \textbf{Equation 2-7}$$

with the distribution function $\boldsymbol{\psi}(\boldsymbol{p})$:

$$\boldsymbol{\psi}(\boldsymbol{p}) = \begin{cases} \boldsymbol{p}_1 = cos\,\phi\,sin\,\theta \\ \boldsymbol{p}_2 = sin\,\phi\,sin\,\theta \\ \boldsymbol{p}_3 = cos\,\theta \end{cases} \qquad \textbf{Equation 2-8}$$

This method is mainly used as the comparison with the VoxTex method to clarify their advantages and disadvantages.
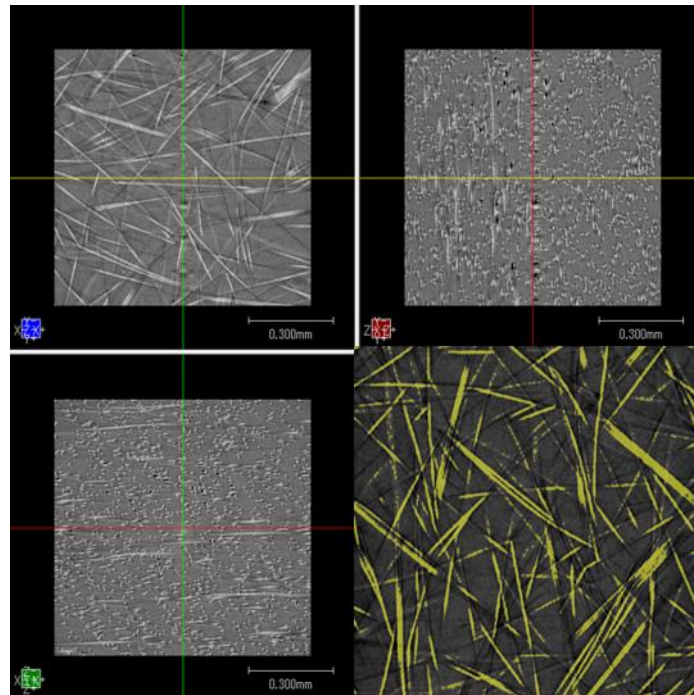


**Figure 2-4. Three views of the 3D model and in-plane fiber binarization using 3D-BON.**
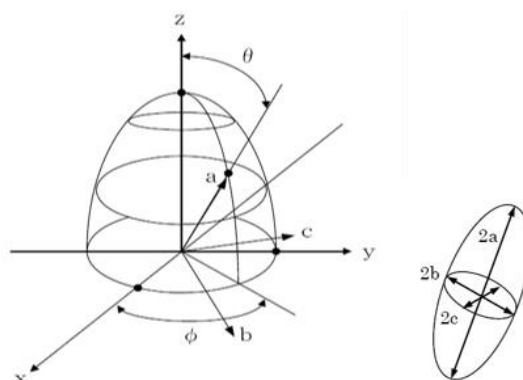
**Figure 2-5. Schematic Fiber orientation calculation in 3D-BON.**

## 2.4. Results and discussions

### 2.4.1. General results

In the present study, the internal geometries of CMT and CTT were observed and analyzed by two 3D X-ray micro-CT methods. The X-ray scanned images of all specimens were input to the introduced two micro-CT methods for fiber orientation calculation as well as the 3D models visualization.

Before the micro-CT processes, the distance between voxels for averaging calculation (window size $w_r$) in the step of voxel model construction in the VoxTex image processing should be considered carefully for accuracy analysis, especially in CTT which have in-plane layered internal structure. Therefore, the out-of-plane window size applied in the micro-CT analysis, refereed further as "volume of interest" (VOI) of the micro-CT analyis, needs to be determined related to the corresponding materials.

Consequently, the VOI's through-thickness dimension of layered stacked CTT is set to 13 pixels, i.e., 44.2 µm to ensure that the thickness of each VOI is close to the thickness of a single thin-tape (44 µm in average). Under this condition setting, the single layer of CTT with different thickness (Thin, Med and Thick) can be separated into one, two or three VOI respectively. And the voxel model calculation of internal geometries properties of corresponding materials can be related to the real layered internal structure of X-ray specimens for detailed analysis. Other two

dimensions of VOIs are equal to the extents of the image. The VOIs are numbered according to their order in position along the thickness direction: VOI 1 to VOI 25. All volumes of interest have a hexahedral shape.

After CT images were collected by the 3D X-ray scanner, the 3D models of specimens were reconstructed using the image processing unit of the X-ray scan system. The CMT model show as traditional DCFRTP with fiber mat internal structure (Figure 2-6 (a)). On the other hand, the CTT models exhibited layered structures, and the individual tapes in the CTT showed orientations that were not perfectly flat (Figure 2-6 (b)). Concentric circles (ring artifacts) were observed at the side faces of the reconstructed 3D model of the X-ray images in previous studies (Figure 2-6 (c)) [19]. These ring artifacts will have great effects on the orientation distributions. And thanks to the improvements in the image reconstruction unit of the X-ray scan system, the ring artifacts were apparently suppressed in these new reconstructed 3D models as shown in Figure 2-6 (b).
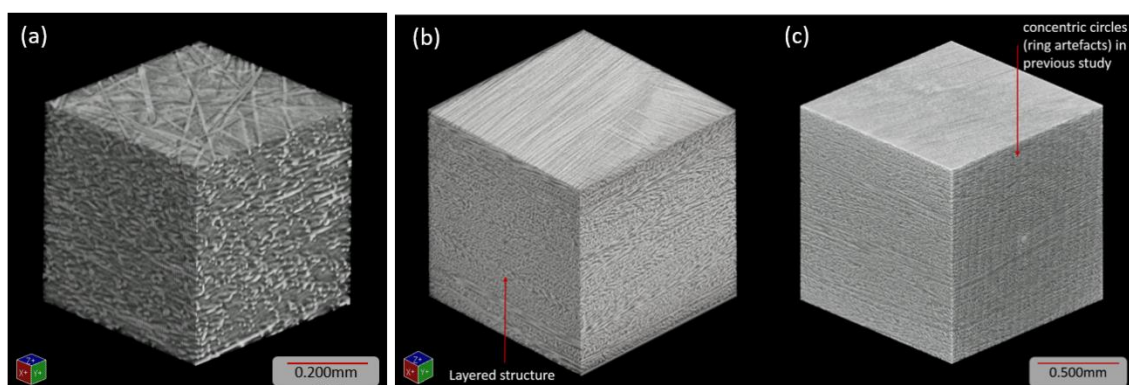


**Figure 2-6. Reconstructed 3D model of CMT-2 (a), CTT-6 (b) and CTT-6 with ring artifact (c).**

In the next step, the X-ray images of the materials were input to the VoxTex and 3D-BON software to conduct the micro-CT analysis.

In VoxTex, the visualized 3D model and histograms of the fiber orientation distribution were constructed using the stacked X-ray images. Figure 2-7 illustrates a CTT-6 example of the fiber orientation distribution model used in the subsequent analysis. The color in the visualized 3D

models (Figure 2-7 (a)) indicates the local in-plane fiber orientation angle $\varphi_{XY}$ (Phi_XY), in units of degrees (°). A two-dimensional histogram, which combines in-plane ($\varphi_{XY}$, Phi_XY) and out-of-plane ($\theta_{XY}$, Theta_XY) fiber orientation distribution angles, is given in Figure 2-7 (b), where the color bars in Figure 2-7 (b), (c) and (d) indicate the number of voxels with certain values (data density).

The orientation distribution shows the prevailing in-plane orientation of the tapes embedded in the samples, and the orientation clusters are observed in the histograms. To investigate this orientation concentration, the distributions of $\varphi_{XY}$ and $\theta_{XY}$ were "unfolded" in the out-of-plane direction as shown in Figure 2-7 (c) and (d) respectively, in order to analyze their changes based on thickness. The unfolded $\varphi_{XY}$ and $\theta_{XY}$ were calculated for each VOI, meaning that the orientation distribution in each row in Figure 2-7 (c) and (d) shows the tape orientation information in the corresponding layer position in these samples. The clusters observed in the unfolded $\varphi_{XY}$ histogram indicate the fiber clusters with their corresponding orientation preferences. The unfolded $\theta_{XY}$ histogram exhibits a concentrated distribution up to 90°. For more detailed analysis of the orientation distribution, the mean value and standard deviations (SD) of both $\varphi_{XY}$ and $\theta_{XY}$ were also calculated for each VOI separately (Figure 2-7 (e) and (f) respectively).
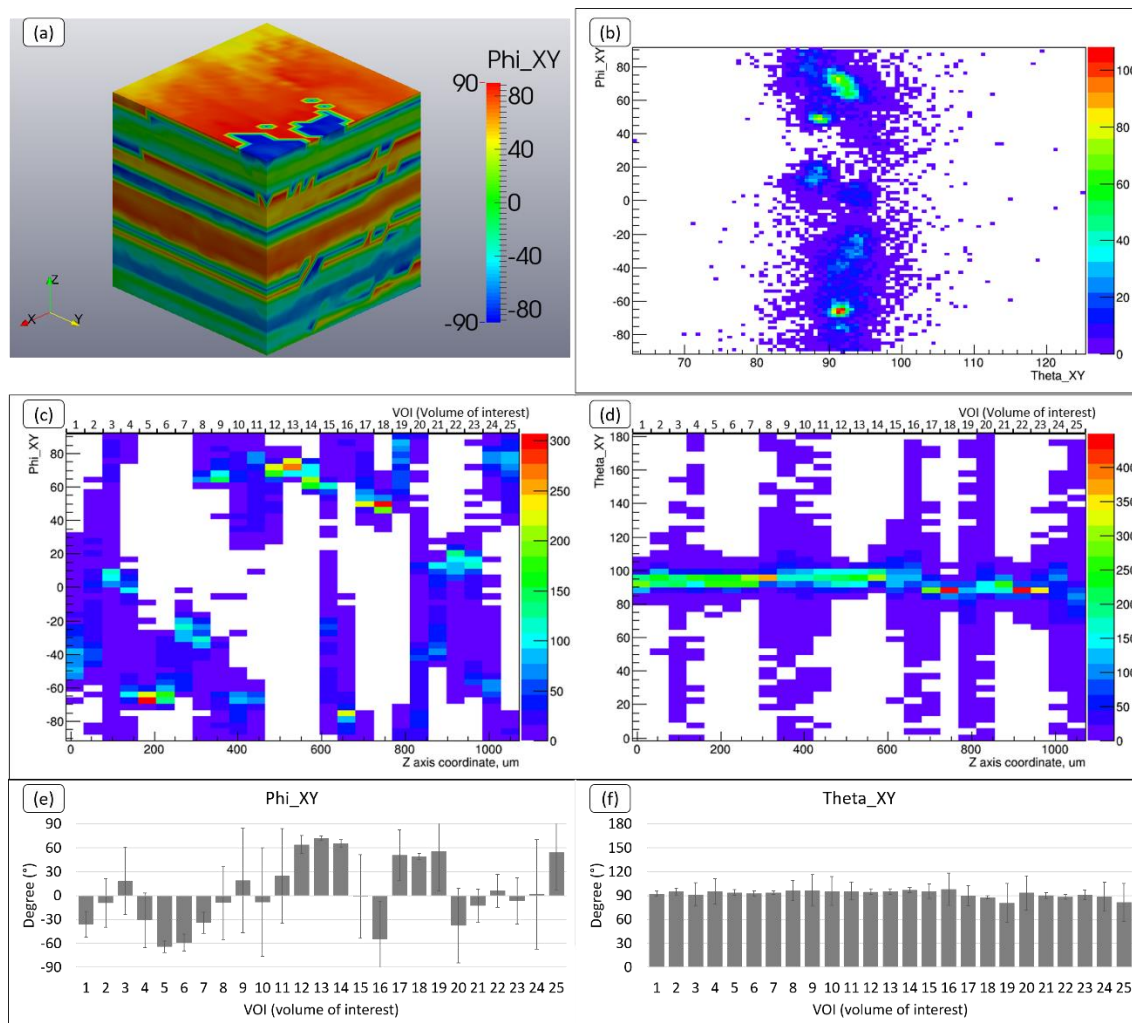
**Figure 2-7. An example of micro-CT data processing: visualized 3D model (a), orientation distribution (b), unfolded distributions of $\varphi_{XY}$ (c) and $\theta_{XY}$ (d), and average values with standard deviations (SD) of $\varphi_{XY}$ (e) and $\theta_{XY}$ (f) of CTT-6.**

On the other hand, in 3D-BON micro-CT analysis, the image binarization and orientation calculation of the X-ray images were conducted and the orientation angles are outputted (Table 2-1) for the orientation tensor calculations. The 3D models of scanned volumes with identified fibers and orientation visualization can also be generated. Under the fiber level binarization, the fiber morphologies and fiber-level orientation distribution visualizations are able to be achieved Figure 2-8.

**Table 2-1. Example of fiber orientation calculation result of CMT-2 by 3D-BON.**

| No | Label | Length(mm) | Position(mm) | | | Angle(deg) | |
| | | | CntrX(mm) | CntrY(mm) | CntrZ(mm) | Theta(deg) | Phi(deg) |
|---|---|---|---|---|---|---|---|
| 1 | 1 | 0.025 | 0.010 | 0.008 | 0 | 90 | 38.660 |
| 2 | 2 | 0.025 | 1.364 | 0.010 | 0 | 90 | 51.340 |
| 3 | 3 | 0.060 | 0.614 | 0.011 | 0 | 90 | 155.977 |
| 4 | 4 | 0.029 | 0.796 | 0.012 | 0 | 90 | 125.478 |
| 5 | 5 | 0.030 | 1.386 | 0.012 | 0 | 90 | 52.461 |
| 6 | 6 | 0.091 | 1.166 | 0.023 | 0 | 90 | 30.685 |
| 7 | 7 | 0.075 | 0.027 | 0.029 | 0 | 90 | 129.111 |
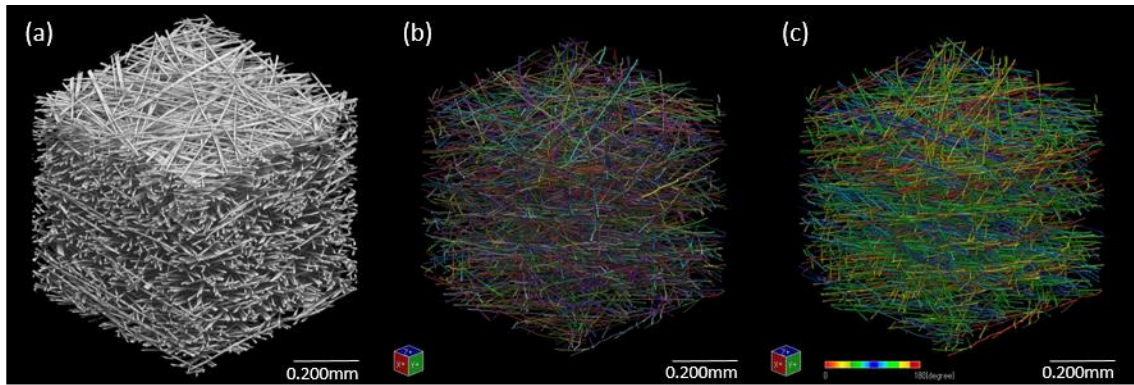


**Figure 2-8. Example of fiber 3D-model (a), single fiber identified model (b) and in-plane orientation quantified model (the color bar indicate the orientation angle from 0° to 180°) (c) of CMT-2 using 3D-BON.**

### 2.4.2.  Significance of X-ray micro-CT

Prior to investigating the internal geometries, one critical problem needs to be solved firstly. Similar to the statement in the introduction section, the scanned volume size for 3D X-ray micro-CT analysis used in this study is restricted to 1.1×1.1×1.1 mm, which is smaller compared with the scale of the reinforcements (monofilament fibers in CMT and tapes in CTT). Therefore, the significance of X-ray micro-CT analysis results needs to be discussed in detail firstly to ensure the reliability of these methods in practical applications.

Although the fiber length in CMT before molding is 6 mm, but thanks to the monofilament level random distribution, the local internal geometries of CMT specimens are considered have similar properties with the internal geometry of CMT material and analogy researches were published [28-30]. On the other hand, the tapes of CTT were cut from the pre-impregnated sheets in sizes from 5 mm × 6 mm to 5 mm ×30 mm with different thickness, which are much larger than the analyzed volume. Also the CTT exhibit relatively high individual difference even in coupon size [79]. The significance of X-ray micro-CT analysis in ROS-structure researches is regarded as a crucial problem [80-82].

### 2.4.2.1. Hypothesis for significance examination

To solve the significance problem, a multi-sample method is developed in the X-ray scanning process to cover the shortage of X-ray scanning devices. In this multi-sample method, multiple specimens are cut off from one kind of material to conduct the X-ray observation, by gathering the VoxTex micro-CT data from the multiple specimens, statistical representative internal geometry properties of one kind of material are possible to acquire. In this section, the statistical significance of the multi-sample method is verified using the individual irregular CTT with different tape length.

Three different tape lengths (6 mm, 18 mm and 30 mm) and four types of composite plates (6 mm, 18 mm, 30 mm and 6&30 mm mixture) were produced to ensure the reliability and repeatability of the multi-sample method. To ensure the representation and accuracy of the X-ray data, 15 specimens each for 6 mm and 18 mm CTT, and 20 specimens each for 30 mm and 6&30 mm CTT, were cut from arbitrary positions of the molded plates.

To ensure that a limited number of small-sized samples is representative for the entire material, distributions of $\varphi_{XY}$ and $\theta_{XY}$ (Figure 2-8 (c) and (d)) of all the specimens are calculated by averaging the fiber orientations in a layer of the analyzed volume. Two premises are firstly stated before the statistical verification: 1) based on the sheet-molding process, the tapes in CTT are uniformly distributed and CTT is known to be a transversely isotropic material [79]; 2) there are multiple tapes exist in each image layer of the scanned volume for micro-CT analysis (Figure 2-9). As such, it can be expected that the in-plane angle distribution of the tapes embedded in CTT is

uniform. Therefore, ensuring that the assembly of samples subjected to multi-sample analysis yields a representative picture of the material is equivalent to validating whether or not the in-plane angle distribution of the embedded tapes (observed in CT images) is actually uniform.

Because there is generally more than one tape present in each layer, the averaging process will cause the distributions of the average in-plane angles in the layers to approach normal distributions, according to the central limit theorem (Figure 2-10). Therefore, the analyzed volume is regarded as statistically significant and representative of the internal geometric properties of the corresponding material when the observed layer-averaged $\varphi_{XY}$ values are normally distributed.
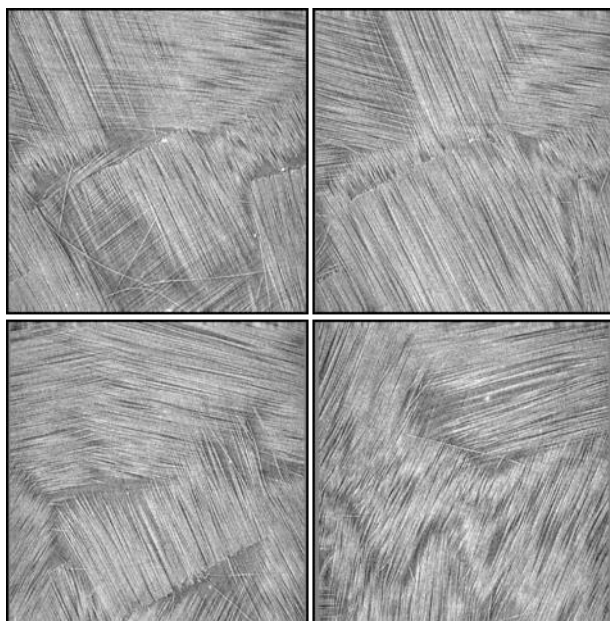


**Figure 2-9. Examples of the X-ray image for micro-CT analysis.**
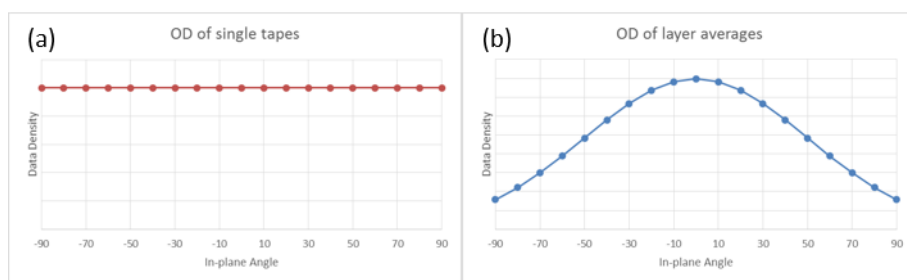


**Figure 2-10. Example of orientation distribution of individual tapes (a) and averaged-layers (b).**

2.4.2.2.   Experimental verification

To clarify this assumption, a statistical simulation was conducted in which random in-plane orientations of tapes were generated by selecting random numbers from a uniform (-90°, 90°) distribution, and the average $\varphi_{XY}$ values of the layers (generating randomly 2 to 4 tapes in each layer) were calculated. The distribution of average $\varphi_{XY}$ for 10000 randomly generated layers with randomly oriented tapes inside is shown in Figure 2-11 (a). The normal distribution fitting curve shows considerable matching with the average $\varphi_{XY}$ distribution with a mean value close to 0°. This result indicates that the representative internal geometry properties of a material can be analyzed using micro-CT data when the average $\varphi_{XY}$ is normally distributed. In the present study, only 25 layer-averaged $\varphi_{XY}$ values can be collected in one X-ray sample, because the sample was separated into 25 VOIs based on tape thickness. The average $\varphi_{XY}$ distribution of one CTT-6 sample exhibits a significant stochasticity (Figure 2-11 (b)), while the result for 10 CTT-6 samples shows a good tendency to normal distribution with a mean value close to 0° (Figure 2-11(c)), indicating that the tapes are uniformly distributed in-plane. Therefore, if the measured orientations $\varphi_{XY}$ do follow a normal distribution, the analyzed volumes are representative for the entire material, rather than for some local region, hence the number of X-ray samples used in this study is sufficient for our analysis. Consequently, our initial objective to ensure the significance and accuracy of multi-sample X-ray analysis became an issue of whether or not the analyzed set of samples provides sufficient micro-CT data to satisfy the normal distribution of the layer-averaged $\varphi_{XY}$ angles.

To identify the distribution and the substantive departures from normality of layer-averaged $\varphi_{XY}$, normal probability plots were created in this study. The normal probability plot is a graphical technique to identify substantive departures from normality. The normal probability plot is a special case of the Q–Q probability plot ("Q" stands for quantile) for a normal distribution. The theoretical quantiles are generally chosen to approximate either the mean or the median of the corresponding order statistics.

First, the randomly-generated tape orientation data were identified with samples of 250 data points (equal to 10 samples in X-ray scanning) and 10000 data points (equal to 400 samples in X-ray scanning), and the results are illustrated in Figure 2-12. The plots show satisfactory agreement with the normal distribution in both cases. The coefficient of determination ($R^2$) of the trend lines

in these plots, which is often used to identify departures of sample data from normality, also show good linearity. The normal probability plot shows adequate visualization and quantification of the data normality determination from the randomly generated data, and the plots of measured micro-CT data are discussed in the next step.

Figure 2-13 illustrates two single-sample data normal probability plots of CTT-6 samples, where the samples were arbitrarily selected from the collected X-ray data. Similar to Figure 2-11 (b), although the single data points represent normality, there are still significant departures from the normal distribution. Figure 2-13 indicates that using the micro-CT data of a single sample to analyze the internal geometry properties of a material may lead to stochastic and non-homogeneous results, which can be affected by the specimen preparation processes. Therefore, multi-sample X-ray data with different tape lengths were studied. The normal probability plots with data of 10 samples are illustrated in Figure 2-14. These plots show much better normality compared to the result for a single sample of 6 mm; the 10-sample groups for 6 mm and 18 mm tapes plotted in Figure 2-14 (a) and Figure 2-14 (b) have comparable normality with the plot of randomly generated data with the same number of samples (Figure 2-12 (a)). The increase of normality from a single sample to 10 samples certified that multi-sample X-ray scanning could be a solution to analyze the internal geometry of ROS when the X-ray sample dimensions are smaller than the strand size. Furthermore, the normal probability plots of $\varphi_{XY}$ also show differences for CTT samples with different tape lengths. The normal probability plots of the 6 mm and 18 mm sets have identical fitting conditions and their $R^2$ values are similar. However, in the CTT-30 and CTT6&30 sets, the plots show worse linearity and their $R^2$ values are lower than in the cases of 6 mm and 18 mm sets. In addition, based on the normal probability plots of 10 samples, the CTT-6&30 set possesses a $\varphi_{XY}$ distribution normality between those of the CTT-18 and CTT-30. The change of normality of $\varphi_{XY}$ distribution with increasing tape length is attributed to the increase of the volume of a single tape. With a fixed sample size, higher volume tapes will lead to lower actual tape contents, and consequently a larger number of samples will be needed to ensure randomness within a certain examined volume. To investigate the effect of the sample number on the normal probability plots of CTT for different tape lengths, additional normal probability plots of each tape length were collected following the sample numbers introduced previously. $R^2$ values of all plots were calculated and are presented in Figure 2-15. The CTT-6 and CTT-18 have good $R^2$ values based on the plots of 10 samples as discussed, and no significant increase in $R^2$ was observed after increasing from 10 samples to 15 samples. Conversely, $R^2$ further increased when the sample number increase from 10 to 15 in the CTT-30 and CTT-6&30. In addition, compared with the increase from 10 to 15, the rate of increase decreases as the sample number is further increased from 15 to 20 in CTT-30 and CTT-6&30. In addition, the one sample

Kolmogorov-Smirnov test (K–S test) of all the specimens were also conducted as the supplementary verification of the normality consistency. The orientation data of 15 samples of all kinds of samples were collected and the IBM SPSS Statistics 24 (IBM Inc.) software was used for conducting the K–S test. The result of K-S test is listed in Table 2-2. From the table, analogy results can be observed with the normal probability plots. Also with 15 samples, all the CTT with different tape lengths exhibit normality in layer-averaged $\varphi_{XY}$. The randomly generated data show the highest normality and with the increase of tape length, the normality of $\varphi_{XY}$ decreased. The $p$-value for statistical hypothesis testing in this K–S test is listed as the "Exact Sig. (2-tailed)", and the $p$-value indicated that in CTT-6 and CTT-18, the layer-averaged $\varphi_{XY}$ are strongly normal distributed ($p$-value is bigger than 0.05), while in CTT-30 and CTT-6&30, the $p$-values are similar and relatively small, but the normal distribution hypothesis is still regarded valid ($p$-value is bigger than 0.01).

**Table 2-2. One-sample Kolmogorov-Smirnov test of 15 CTT samples in each tape length and randomly generated data**

|  |  | CTT-6 | CTT-18 | CTT-30 | CTT-6&30 | Random |
|---|---|---|---|---|---|---|
|  | N | 375 | 375 | 375 | 375 | 375 |
| Normal | Mean | 2.3494 | 7.7754 | -1.9267 | 3.8557 | -1.7616 |
| Parameters[a,b] | Std. Deviation | 34.23593 | 39.33078 | 40.97434 | 36.27773 | 40.00293 |
| Most | Absolute | 0.045 | 0.058 | 0.079 | 0.080 | 0.030 |
| Extreme | Positive | 0.044 | 0.049 | 0.079 | 0.060 | 0.030 |
| Differences | Negative | -0.045 | -0.058 | -0.072 | -0.080 | -0.026 |
| Test Statistic | | 0.045 | 0.058 | 0.079 | 0.080 | 0.030 |
| Exact Sig. (2-tailed) | | 0.426 | 0.152 | 0.018 | 0.015 | 0.883 |
| Point Probability | | 0.000 | 0.000 | 0.000 | 0.000 | 0.000 |

a. Test distribution is Normal.

b. Calculated from data.

Since the 15 samples results exhibit considerable normality in all the cases and increasing the number of samples beyond 15 leads to a negligible increase in normality. Therefore, the number of samples adopted in the multi-sample micro-CT analysis of CTT with different tape lengths was set to 15 in this study. However, the generalization of sample number for multi-sample micro-CT analysis of ROS materials still features some complexity because the sample size, instrument

capability and software algorithm must be taken into consideration as well. Moreover, since the CMT need fewer samples to reach the statistical level, so 15 samples are also sufficient for the X-ray micro-CT study of CMT material.
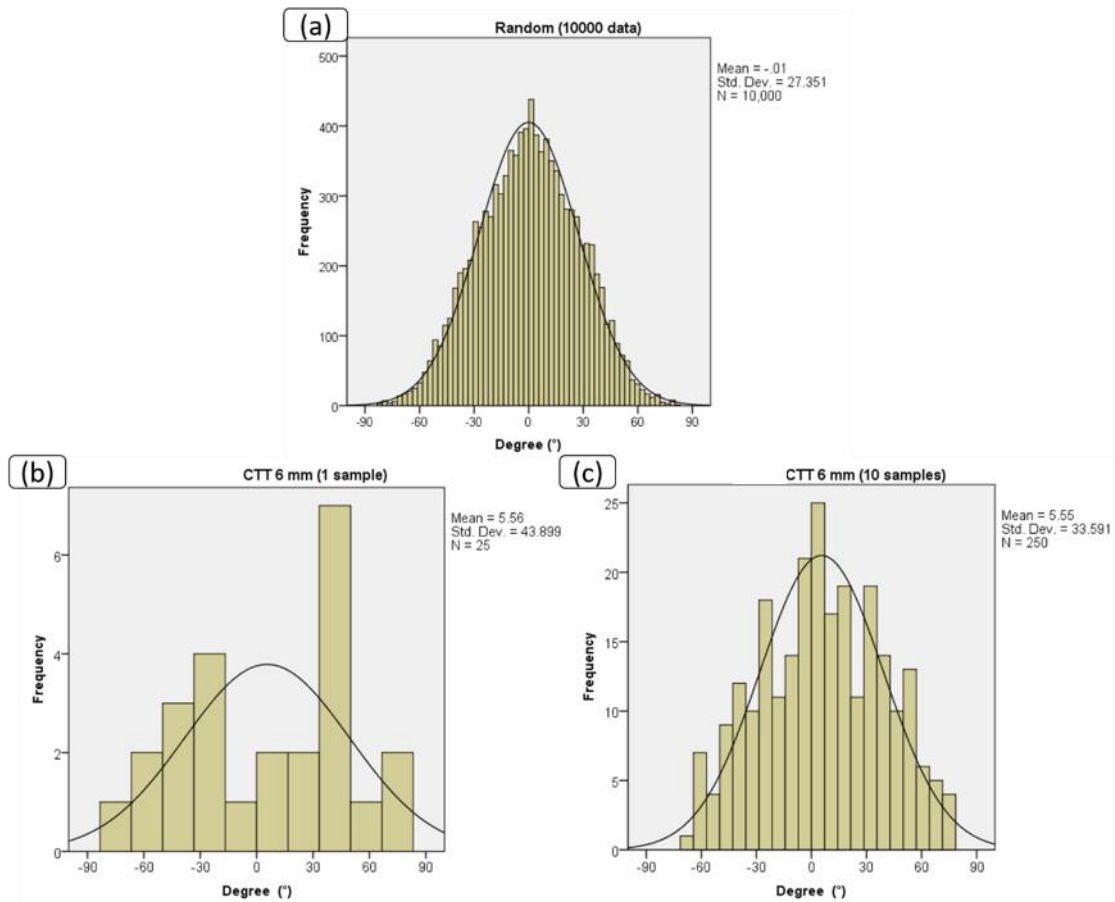


**Figure 2-11. Histograms of layer-averaged $\varphi_{XY}$ distributions with 10000 randomly generated layers (a), one CTT-6 samples (b) and 10 CTT-6 mm sample (c).**
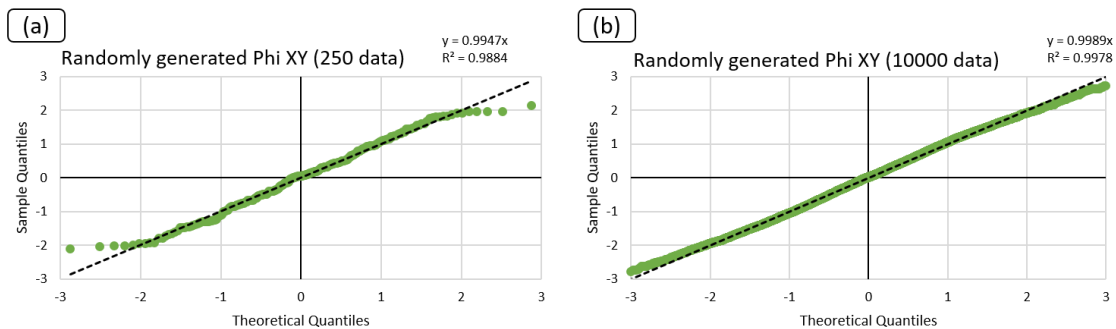
**Figure 2-12. Normal probability plots of randomly generated $\varphi_{XY}$ with 250 data points (a) and 10000 data points (b).**
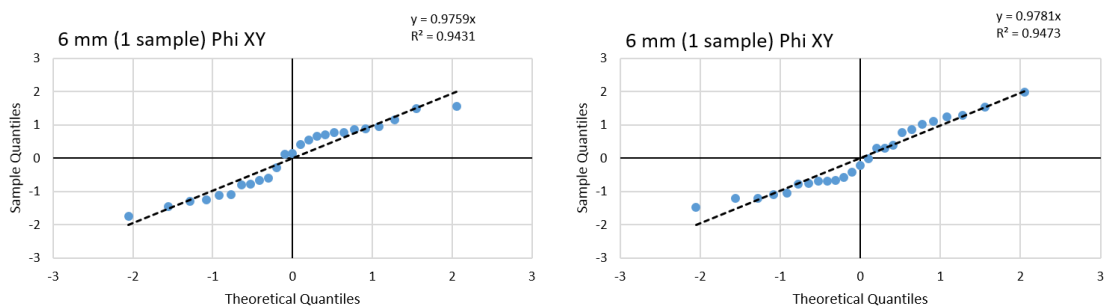


**Figure 2-13. Normal probability plots of $\varphi_{XY}$ in arbitrary single CTT-6 samples.**
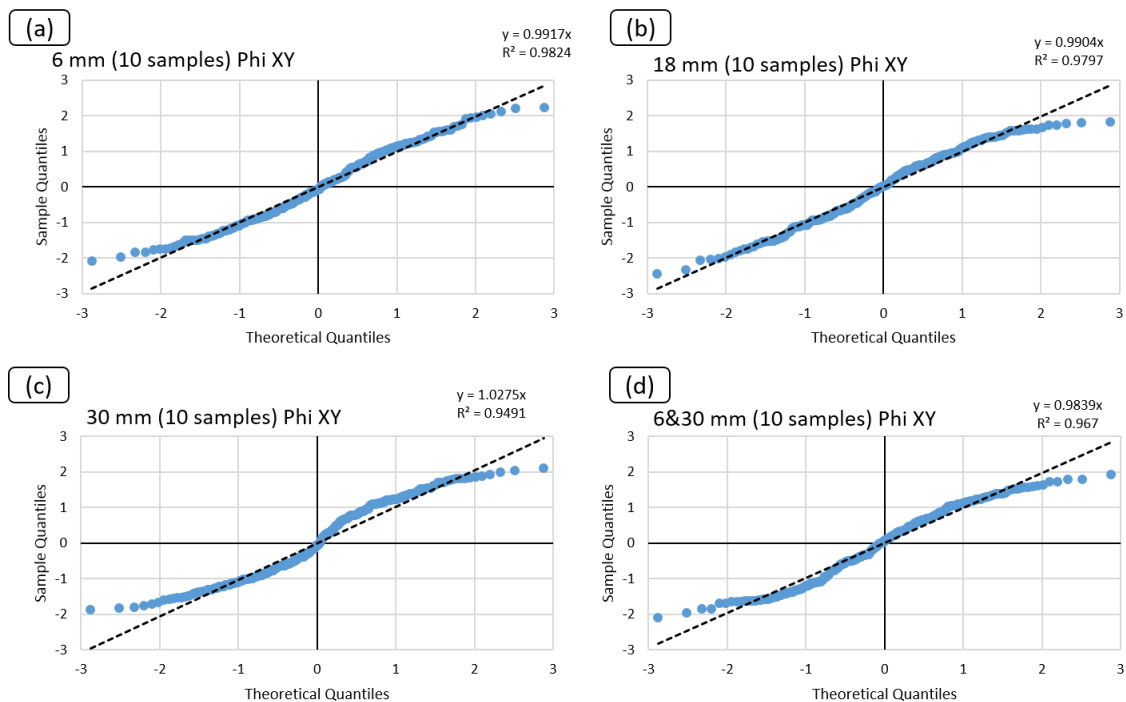
**Figure 2-14. Normal probability plots of $\varphi_{XY}$ for 10 samples of CTT-6 (a), CTT-18 (b), CTT-30 (c) and CTT-6&30.**
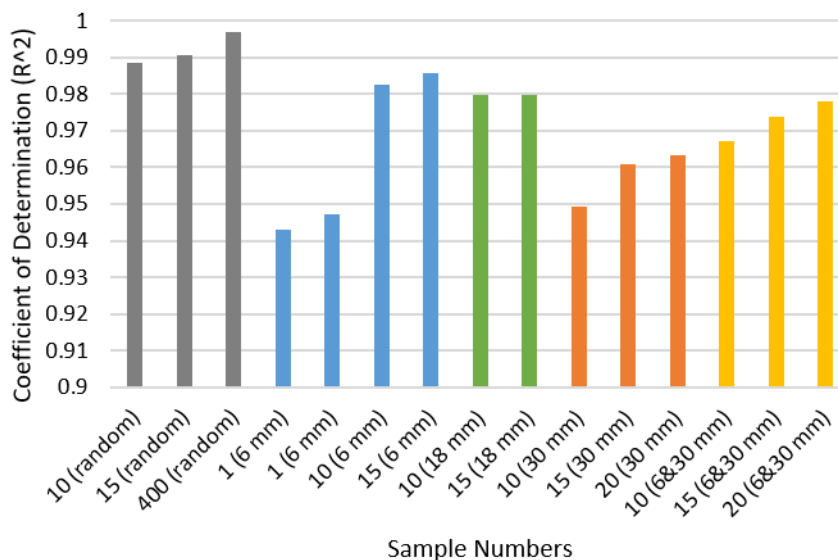


**Figure 2-15. Coefficient of determination ($R^2$) of different normal probability plots with varied sample numbers.**

48

### 2.4.3. VoxTex results

After the significance of X-ray micro-CT analysis is verified in the previous section, the internal geometries of CMT and CTT are to be studied. In this section, the micro-CT analysis using VoxTex method are conducted.

One of the important innovation points in the VoxTex method is the introduction of VOI definition to give the X-ray micro-CT better layered analysis capability. This innovation can provide more efficient internal geometry study of layered internal structural materials (like CTT), but the VOI definition is considered meaningless for the internal geometry analysis of traditional DCFRTP like CMT. One sample of CMT-2 internal geometry analyzed using VoxTex is illustrated in Figure 2-16. From the results, the VOI setting obviously cannot help to analyze the internal geometry compared with the CTT sample introduced before. Consequently, the internal geometry analysis using VoxTex method will be concentrated on the CTT materials, and the effect of molding conditions and tape morphologies on the internal geometry properties are to be revealed in this section.
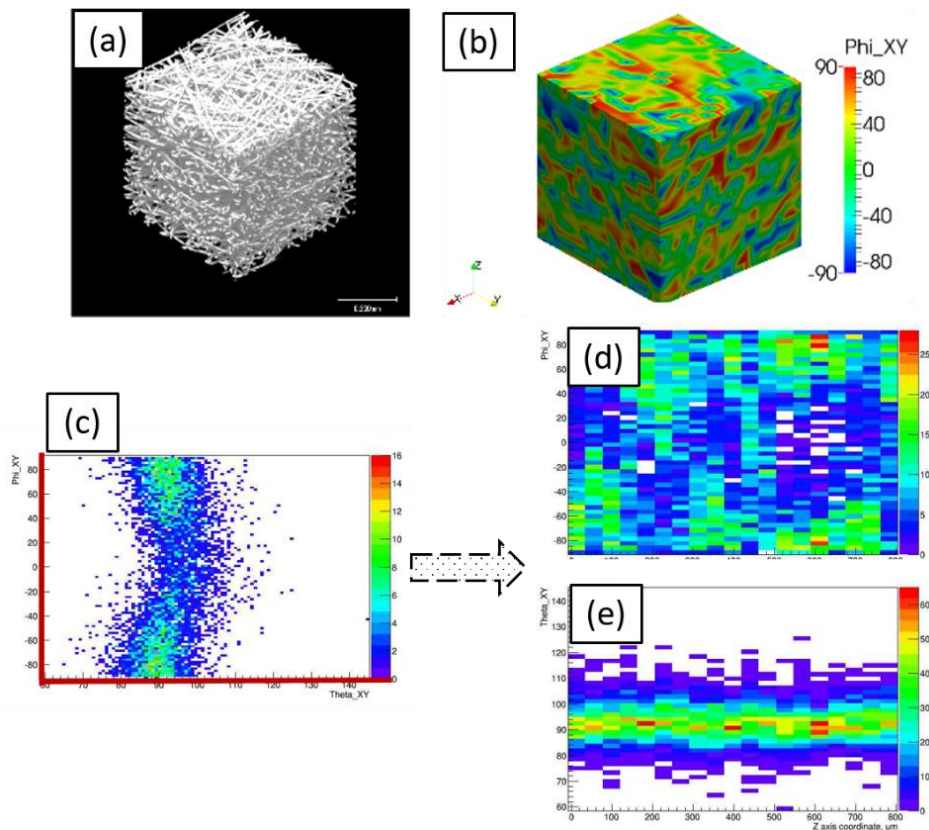
**Figure 2-16. CMT-2 3D model (a), $\varphi_{XY}$ quantified 3D model (b), two-dimensional histogram of $\varphi_{XY}$ and $\theta_{XY}$ (c) and the unfolded histograms of $\varphi_{XY}$ (d) and $\theta_{XY}$ (e).**

2.4.3.1.   Effect of molding pressure

In the first sub-section, the capability of VoxTex method is verified using CTT-6 manufactured with two different molding conditions ($M_3$ CTT-6 and $M_{10}$ CTT-6 as introduced). Using the stacked micro-CT images, the visualized 3D model of the material and histograms of fiber orientation distribution were calculated [19].

The visualized 3D micro model with in-plane fiber orientation of $M_{10}$ CTT-6 is shown in Figure 2-17. The angles are given in the global Cartesian coordinate system $(X, Y, Z)$ identical to the Cartesian system $(x_1, x_2, x_3)$ introduced previously. The color in the model (as well in Figure 2-22 (a)) indicated local in-plane fiber orientation angle $\varphi_{XY}$ (Phi_XY), with degree (°) as the unit in this study. Orientation changes layer by layer, but the not-fully-flat in-plane orientation and waviness through out-of-plane direction (Z axis) indicated the CTT also have orientation irregularity as it is the case with conventional DCFRTP.

The two-dimensional histogram where the in-plane ($\varphi_{XY}$) and out-of-plane ($\theta_{XY}$, Theta_XY) fiber orientation distribution angle are combined is shown in Figure 2-18, the color bar in this figure and figures hereinafter indicate the data density of the orientation. The orientation distribution shows special features. The angle $\theta_{XY}$ is concentrated around 90 degree with small dispersion, which means the CTT is almost in-plane oriented. Several clusters of $\varphi_{XY}$ are observed in the figure, and these clusters show irregularity in the in-plane angle. Because the fibers of CTT are almost in-plane oriented, so the distributions of $\varphi_{XY}$ and $\theta_{XY}$ are "unfolded" as described in section 2.4.1– through the out-of-plane direction to analyze their change through the thickness. Figure 2-19 shows the unfolded distribution of $\varphi_{XY}$ (a) and $\theta_{XY}$ (b) through z axis. The unfolded $\varphi_{XY}$ distribution indicates that the concentrated clusters of $\varphi_{XY}$ in Figure 2-18 do not mean local concentration of tapes in CTT. For example, the $\varphi_{XY}$ distribution cluster from 20 degree to 80 degree in Figure 2-18 is actually combined by three small clusters located at different z-positions (Figure 2-19). On the other hand, although the thickness of VOI is set close to the thickness of a single tape, the orientations of layers are still not independent. Figure 2-19 (a) shows that small clusters still exist in the model. The size of the clusters are generally 3 to 4 VOI, also a larger cluster (VOI 15 to 22, 30 to 70 degree) is found. Because the tapes in CTT are almost in-plane oriented (Figure 2-19 (b)), this result means some tapes with same orientation may stick

together during the wet-type paper-making process, or the tape waviness and tape splitting occurred locally. In addition, Figure 2-19 (a) indicates that the $\varphi_{XY}$ is not randomly distributed, this is because the reconstructed 3D model of CTT is smaller than the tapes due to the limited volume that can be imaged. The relatively small dimensions of the sample cannot ensure the statistical randomness of orientation distribution because of the size effect of the tapes and the internal geometry features of the composites should be analyzed under the multi-sample method. $\theta_{XY}$ shows lager scatter around the center layer of the model (VOI 13, Figure 2-19 (b)), which is considered to be caused not by the material feature but by the ring artefacts mentioned in the beginning of this section, which increase the isotropy of the calculated angles. Therefore, the scatter in VOI 13 will be discarded from the analysis of the results.
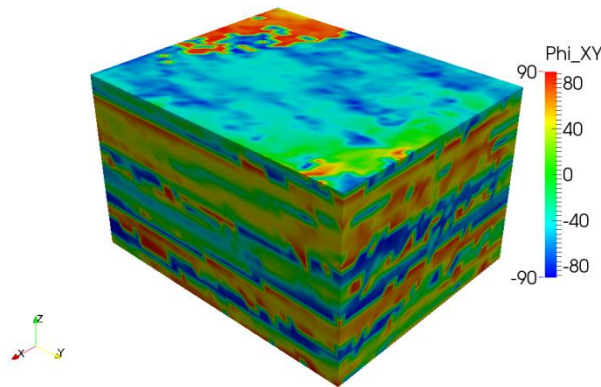


**Figure 2-17. Typical 3D micro model with visualized in-plane fiber orientation distribution of $M_{10}$ CTT-6, the Phi_XY ($\varphi_{XY}$) indicate in-plane orientation angle.**
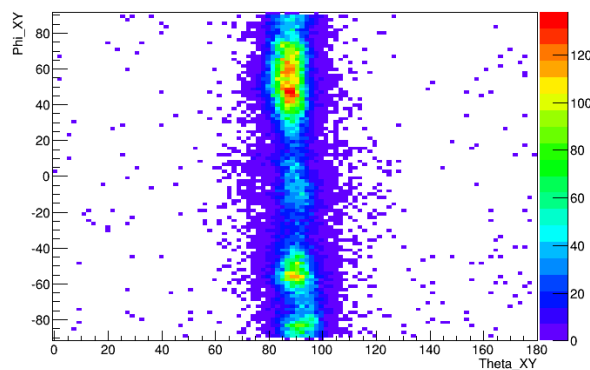


**Figure 2-18. Typical two-dimensional histogram combined the in-plane ($\varphi_{XY}$) and out-of-plane ($\theta_{XY}$) fiber orientation distribution in the total volume of the $M_{10}$ CTT-6 specimens.**
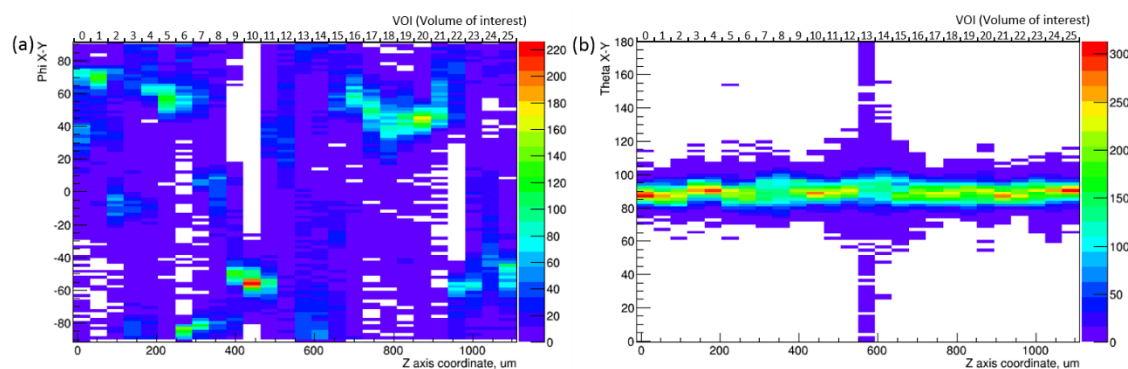
**Figure 2-19. Unfolded histograms of $\varphi_{XY}$ (a) and $\theta_{XY}$ (b) of $M_{10}$ CTT-6.**

To study the clusters of $\varphi_{XY}$ in detail, the 3D model with $\varphi_{XY}$ distribution (Figure 2-17) is combined with the unfolded $\varphi_{XY}$ histogram through z axis (Figure 2-19 (a)). The subsets of the 3D model separated by the VOI were extracted following the clusters that appeared in the unfolded $\varphi_{XY}$ histogram, which means that the 3D morphologies of the orientation concentration areas (the clusters in Figure 2-19 (a)) can be specified and extracted from the general 3D model (Figure 2-17). The VOI 4 to 7, 9 to 11 and 16 to 21 are shown in Figure 2-20. After the subsets were extracted, the threshold of $\varphi_{XY}$ is applied on the model to identify the fiber distributions in concentrated $\varphi_{XY}$ and the threshold ranges are also illustrated in Figure 2-20. The extracted 3D models with threshold of $\varphi_{XY}$ and the corresponding areas in unfolded $\varphi_{XY}$ histogram proved the assumption that the tapes can interact during the wet process and disturb the ideal uniformly random orientation distribution, which would exist if the placements of the tapes were independent. The existence of the $\varphi_{XY}$ distribution clusters through z axis is due to the tapes with the same orientation sticking together during the wet-type paper making process, as well as tape waviness and tape splitting taking place locally during the compression molding process. The 3D model of VOI 4 to 7 demonstrates 4 different layers (tapes) with the same orientation distribution pattern. In contrast, the 3D model of VOI 9 to 11 shows an integral part of tape with some scattered areas which are considered to be the tape waviness and splitting. On the other hand, the 3D models of VOI 16 to 21 exhibit both structural features: tapes are stuck together at the top of the model, while scattered areas are observed on the bottom side. The combination of the 3D model with the unfolded $\varphi_{XY}$ histogram shows a high capability for the quantitative internal geometry study of the CTT with complex structural features. By extracting the subsets models, the detail structures and tape positions are reconstructed visually.

For the further research of the micro-structure and combination with simulations, the unfolded histograms were quantified. The average values and standard deviations (SD) of both $\varphi_{XY}$ and $\theta_{XY}$ were calculated by each VOI (Figure 2-21). The quantified orientation distribution of $\varphi_{XY}$ reproduces the visualized histogram to a certain extent. The clusters in VOI 16 to 21 observed in the histograms are also shown as series of data with SD indicated by error bars. In contrast, the results of VOI 4, 6, 7 and 11 show significant mismatch between the peak values in Figure 2-19 (a) and the average value in Figure 2-21 (a). This is caused by the multimodality of the orientation distributions in these VOIs. The mismatch is caused by the multiple orientation concentrations in one VOI and the SD is significantly high even though the histogram show apparent orientation concentrations. On the other hand, when there is a single aligned integral part of tape in the VOI, the average value is perfectly matched with the peak in histogram, and the SD is small as the VOI 10. In addition, the average value and SD of $\theta_{XY}$ show concentrations same as the observed in the unfolded histogram. The increase of SD around the center layer is caused by the ring artefacts as discussed before.
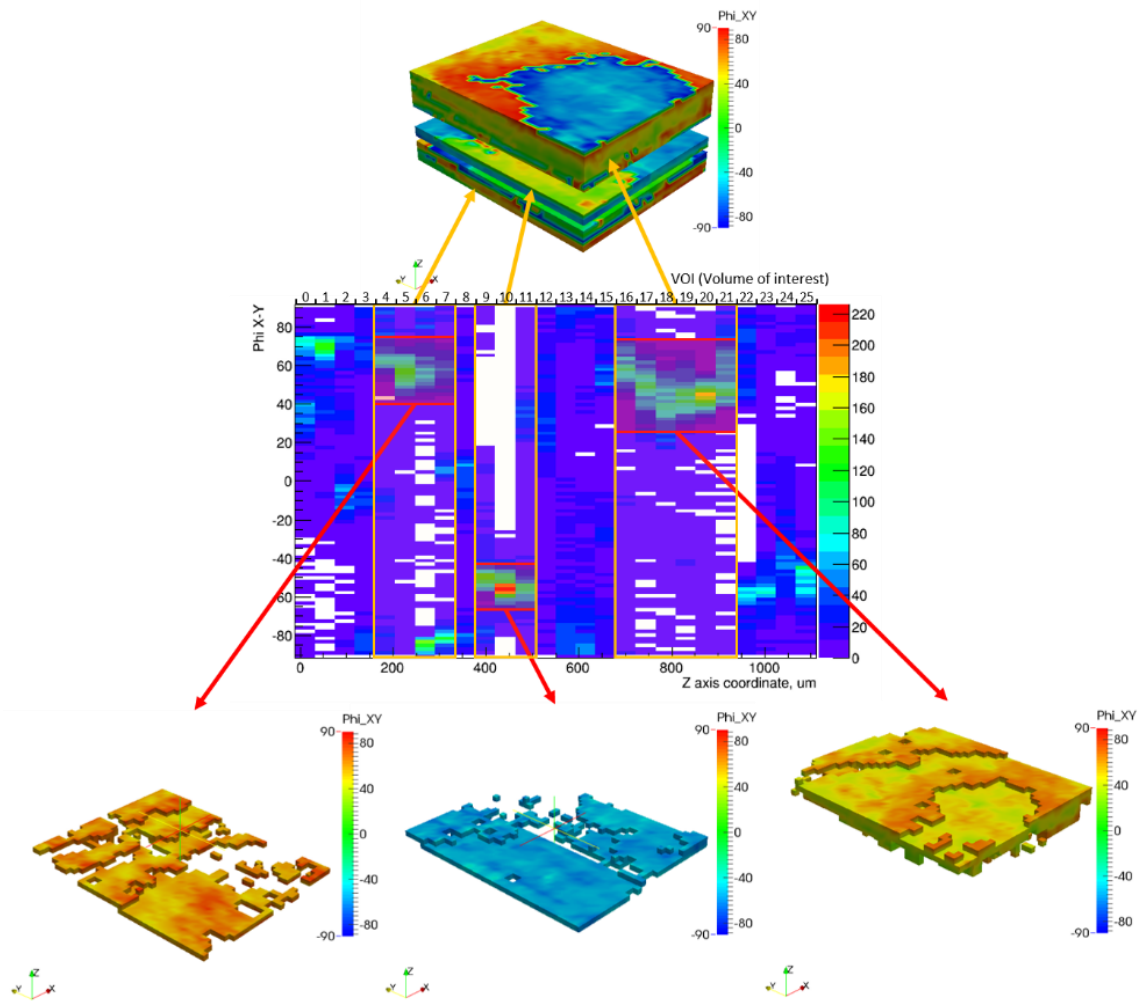
**Figure 2-20. Unfolded $\varphi_{XY}$ histogram and the corresponding clusters in visualized 3D model of $M_{10}$ CTT-6.**
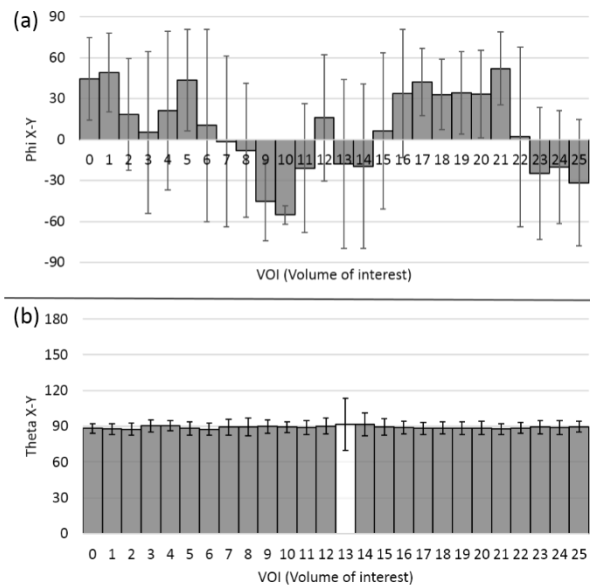
**Figure 2-21. Average values and standard deviations (SD) of $\varphi_{XY}$ (a) and $\theta_{XY}$ (b) of $M_{10}$ CTT-6.**

Additionally, the methodology is employed to characterize the micro-structural change caused by molding pressure: the differences between $M_3$ and $M_{10}$ specimens, produced with the molding pressure of 3 and 10 MPa respectively.

The $M_3$ CTT-6 3D model with $\varphi_{XY}$ distribution and the $\varphi_{XY}$-$\theta_{XY}$ two-dimensional histogram of $M_3$ CTT-6 are illustrated in Figure 2-22. The histogram of $M_3$ CTT-6 shows better $\theta_{XY}$ concentration and the clusters of $\varphi_{XY}$ are more scattered than $M_{10}$ CTT-6 because of the much lower molding pressure. The two-dimensional histogram of $\varphi_{XY}$-$\theta_{XY}$ also is unfolded through out-of-plane direction (Figure 2-23). Compared with the $\varphi_{XY}$ distribution of $M_{10}$ CTT-6 (Figure 2-19 (a)), the $\varphi_{XY}$ distribution of $M_3$ CTT-6 (Figure 2-23 (a)) exhibits better concentration along the z axis. Although the orientation of each layer in $M_3$ CTT-6 is still not independent, the clusters are relatively small (2 to 3 VOIs in general). The difference in $\theta_{XY}$ distributions of $M_3$ (Figure 2-23 (b)) and $M_{10}$ (Figure 2-19 (b)) CTT-6 is insignificant.

The effect of the higher concentrated $\varphi_{XY}$ distribution on the 3D structure of CTT is also studied by subsets of the model with $\varphi_{XY}$ thresholds (Figure 2-24). Both the stuck tapes and tape splitting, which are observed in $M_{10}$ model (Figure 2-20), are also observed in $M_3$ model. The model with $\varphi_{XY}$ thresholds of VOI 4 to 6 and VOI 6 to 8 in Figure 2-24 show as the well aligned tapes stuck together, while the cluster of VOI 13 to 18 exhibit scattered orientation concentration

areas with irregular model shape, which is `considered to be a structure disturbance caused by the tape splitting and tape waviness. But compared with the subset models of $M_{10}$ CTT-6, the $M_3$ models show better orientation concentration based on the color of the models (subset model VOI 4 to 6 in Figure 2-23).

The representative X-ray images of both $M_{10}$ and $M_3$ CTT-6 were selected and illustrated in Figure 2-25. Compared with the general one (Figure 2-25 (a)), the tape splitting mentioned before is clearly observed in $M_{10}$ image as randomized single fibers (Figure 2-25 (b)). In contrast, the image of $M_3$ CTT-6 shows no tape splitting but voids as the molding defects (Figure 2-25 (c)). The tape splitting generated based on the mechanism that high pressure during the molding process will split randomly distributed tapes that were stirred during the paper making process. Consequently, the tape splitting just observed in $M_{10}$ CTT-6. The voids appear because the low molding pressure cannot force the resin into the fissures along tapes. X-ray CT technics show potential to quantify voids volume and location of composites under different molding conditions [83], but there still have a number of problems to tackle for precise quantification and will discuss in further researches. The average values and SD of $\varphi_{XY}$ and $\theta_{XY}$ are also quantified for $M_3$ CTT-6 (Figure 2-26). The SD of $\varphi_{XY}$ in $M_3$ CTT-6 are lower on average than in $M_{10}$ because less tape splitting occurred in low molding condition. The SD of $\theta_{XY}$ is slightly lower in $M_3$ than in $M_{10}$, which indicates that the higher molding pressure causes a higher tape waviness because the tape splitting decreases the micro-structural regularity.

The comparison between the results of $M_3$ and $M_{10}$ CTT-6 indicates that the introduced methodology exhibits a significant capability to evaluate the differences in the internal geometry caused by the difference in molding pressure.
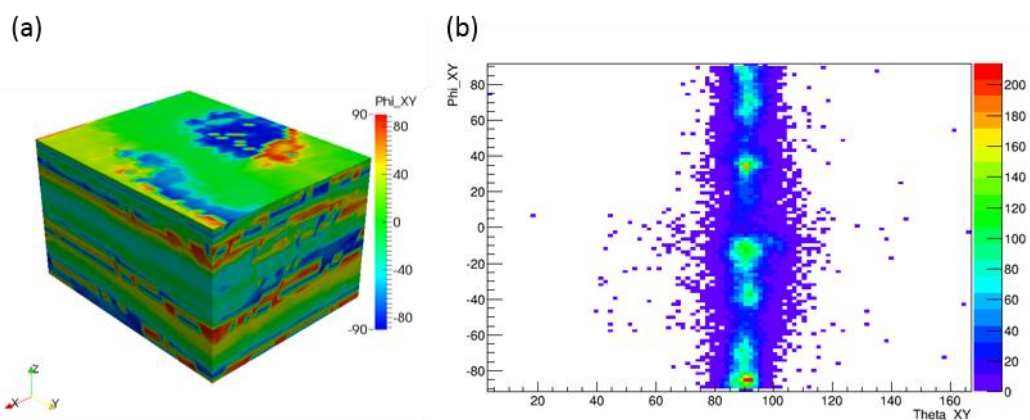


**Figure 2-22. Typical 3D model ($\varphi_{XY}$ visualized) (a) and two-dimensional histogram of $\varphi_{XY}$ and $\theta_{XY}$ (b) of $M_3$ CTT-6.**
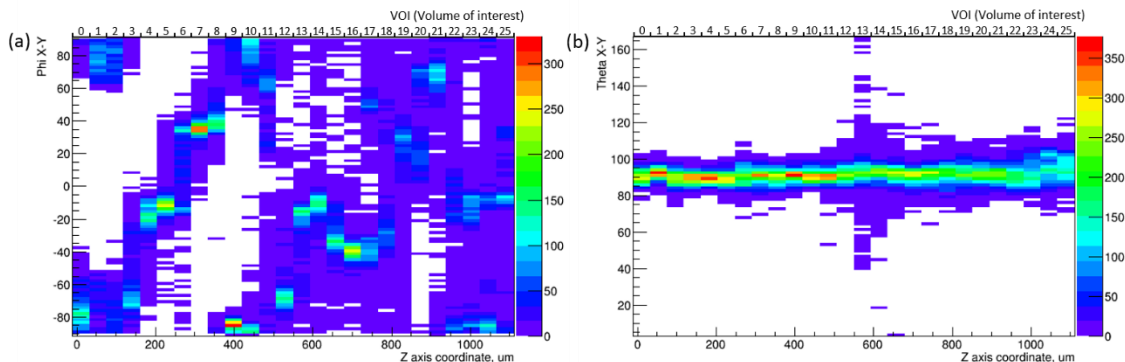
**Figure 2-23. Unfolded histograms of $\varphi_{XY}$ (a) and $\theta_{XY}$ (b) of $M_3$ CTT-6.**
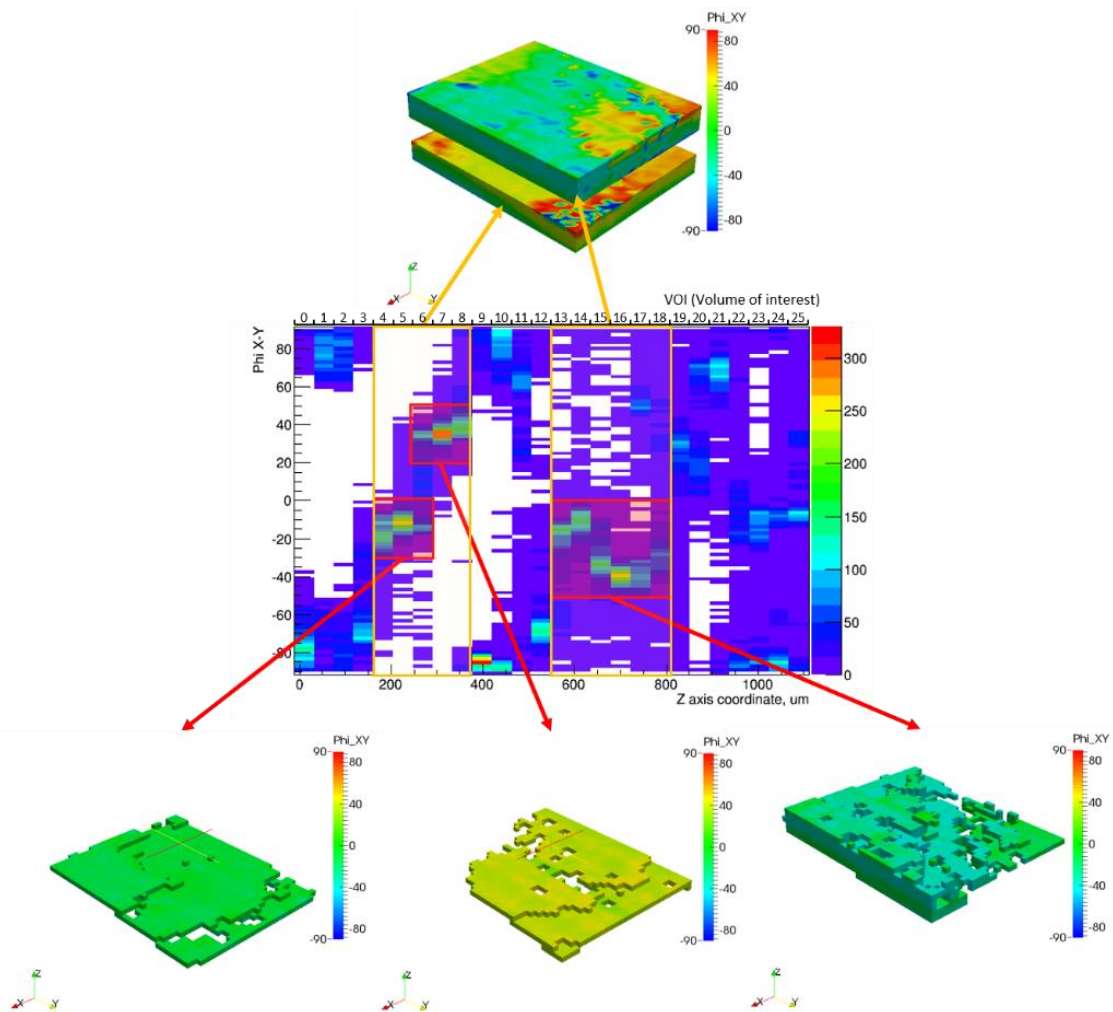


**Figure 2-24. Unfolded $\varphi_{XY}$ histogram and the corresponding clusters in visualized 3D model of $M_3$ CTT-6.**

57
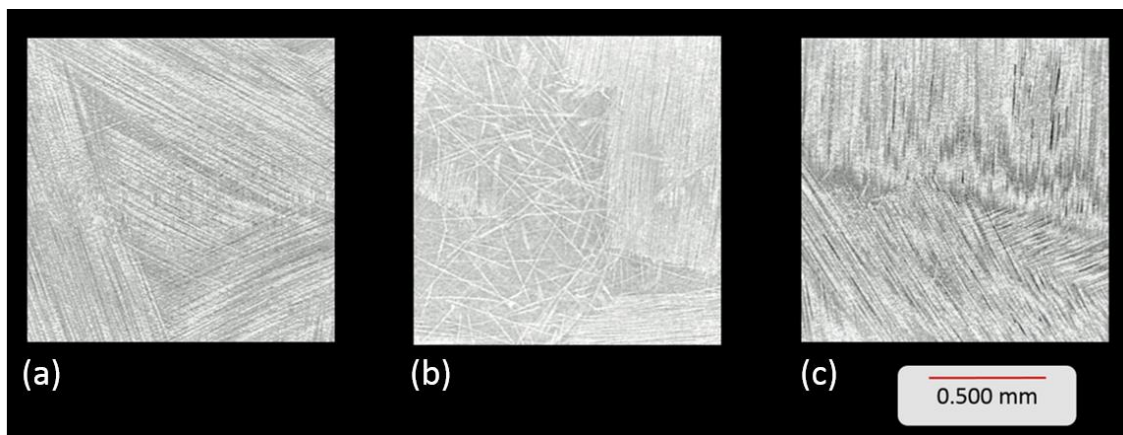
**Figure 2-25. X-ray images of a section of CTT with well-preserved tapes (a, from $M_{10}$ CTT-6), $M_{10}$ CTT-6 with tape splitting (b) and $M_3$ CTT-6 with voids (c). Grey value in the images reflects the X-ray attenuation coefficient of the material, which is a function of its density and elemental composition and the grey value range of the images is from -696 to 5447.**
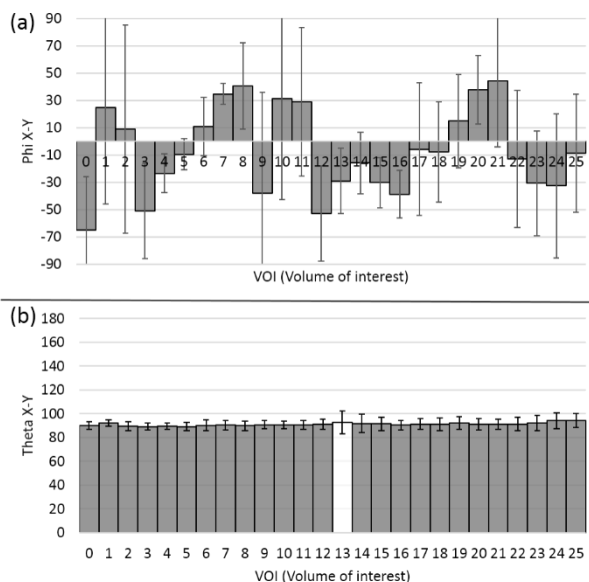


**Figure 2-26. Average values and standard deviations (SD) of $\varphi_{XY}$ (a) and $\theta_{XY}$ (b) of $M_3$ CTT-6.**

2.4.3.2.   Effect of tape length

After the capability was evaluated, the VoxTex method is applied for the verification of tape length effect on the internal geometry of CTT. In this sub-section, the CTT used for significance verification are adopted for the tape length study, i.e. the CTT-6, CTT-18, CTT-30 and CTT-6&30.

Histograms of the fiber orientation distribution and visualized 3D models of 15 samples for each tape length variant were generated. The internal geometric properties of CTT with different tape lengths were studied for all sample results, and two typical samples were selected to demonstrate the microstructural differences.

The unfolded histograms of $\varphi_{XY}$ orientation distribution as well as the $\varphi_{XY}$ visualized 3D models with thresholded subsets of CTT-6, CTT-18, CTT-30 and CTT-6&30 are illustrated for two typical samples from each variant (Figure 2-27–Figure 2-30). These figures indicate that, although the thickness of VOI is set close to the thickness of a single tape to isolate the orientation distribution of each layer, the orientations of the layers are still not independent. $\varphi_{XY}$ distribution clusters are a common phenomenon that can be found in all histograms here (the color boxes in (a) of Figure 2-27–Figure 2-30). As the tape length increases, the sizes of the orientation clusters become smaller and the orientation distributions show better concentration and independence. The CTT-6&30 exhibit similar results as the CTT-18.

To study the clusters of $\varphi_{XY}$ in the histograms in greater detail, 3D maps of $\varphi_{XY}$ distribution are combined in Figure 2-27–Figure 2-30 with the unfolded $\varphi_{XY}$ histogram through the $Z$ axis. The subsets of the 3D maps separated by the VOI were extracted based on the clusters in the unfolded $\varphi_{XY}$ histograms. The color scales of $\varphi_{XY}$ are also given on these maps to identify the tape orientation distributions in concentrated $\varphi_{XY}$ after the subsets were extracted. The 3D maps are illustrated in the (b) parts and the thresholded subsets are illustrated in the (c) parts of Figure 2-27–Figure 2-30. The extracted subsets indicate that the internal geometry of adjacent tape layers show diversity depending on the tape length.

In the CTT-6, large orientation clusters, which indicate orientation concentration, occurred within a certain range of thickness. Based on Figure 2-27, the subsets of the large orientation clusters have two different morphologies. One morphology is the scattered cluster, in which neatly

oriented layers cannot be found and the model consists of scattered small clusters (Figure 2-27 (c1)). Another morphology is tape attachment, exhibited for tapes located in different layers with the same orientation and attached together (Figure 2-27 (c2)). In the case of CTT-6, both these structural morphologies are most likely generated during the wet-type paper making process introduced previously. When the tapes were stirred in water, interactions between them may have caused tape breakage (which can cause scattered fiber orientation) and tape agglomeration (which can cause tape attachment), leading to the observed morphologies.
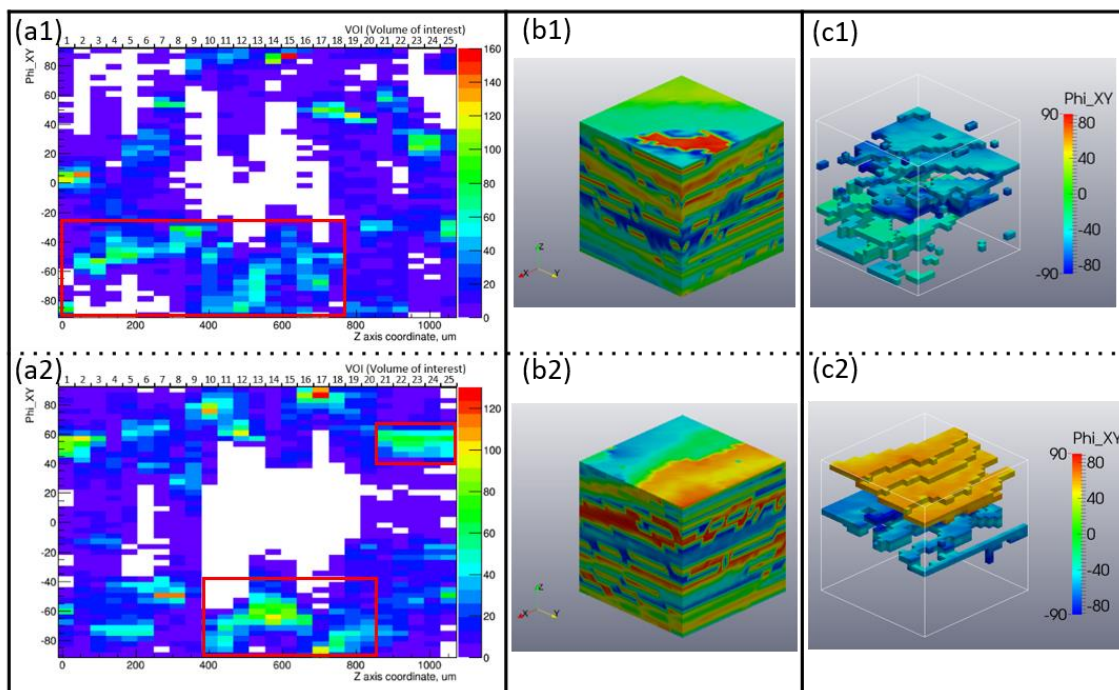


**Figure 2-27. Unfolded histograms of $\varphi_{XY}$ (a) and orientation-visualized 3D models (b, c) of two typical CTT-6 samples (the thresholded subset 3D models (c) correspond to the red boxes in (a)).**
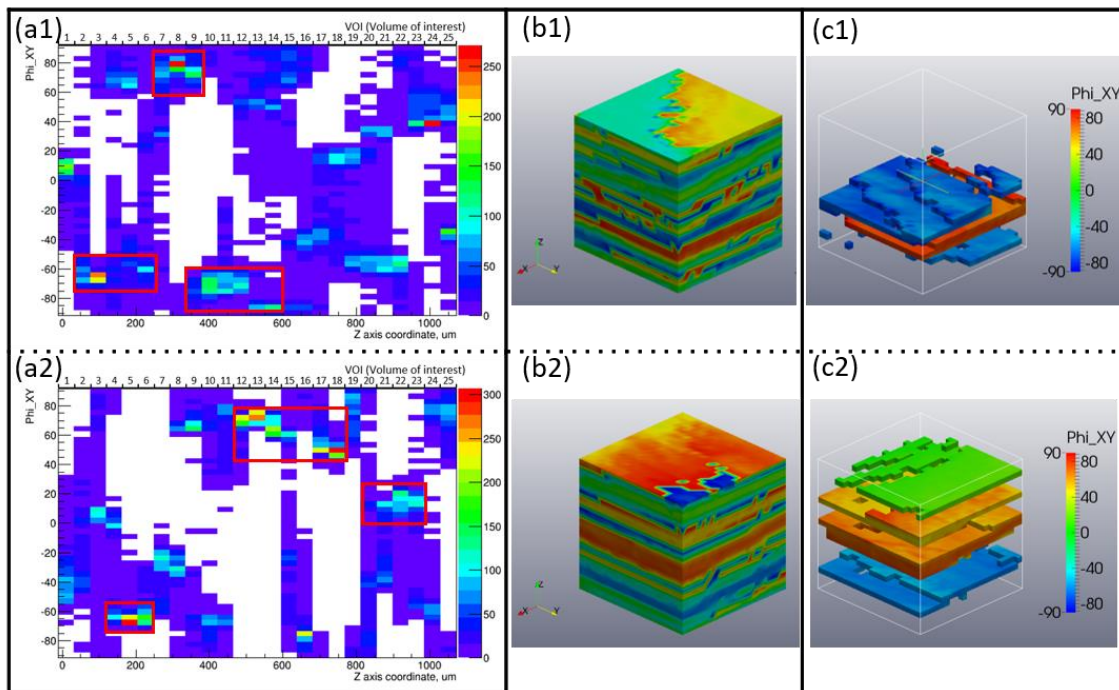
**Figure 2-28. Unfolded histograms of $\varphi_{XY}$ (a) and orientation-visualized 3D models (b, c) of two typical CTT-18 samples (the thresholded subset 3D models (c) correspond to the red boxes in (a)).**
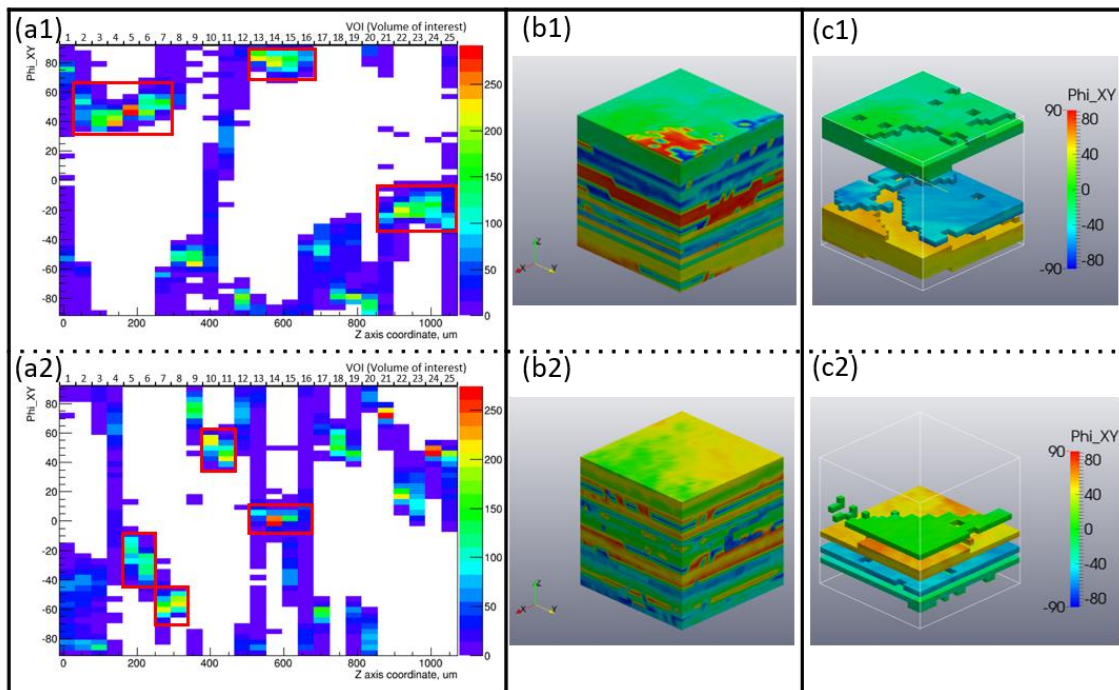
**Figure 2-29. Unfolded histograms of $\varphi_{XY}$ (a) and orientation-visualized 3D models (b, c) of two typical CTT-30 samples (the thresholded subset 3D models (c) correspond to the red boxes in (a)).**
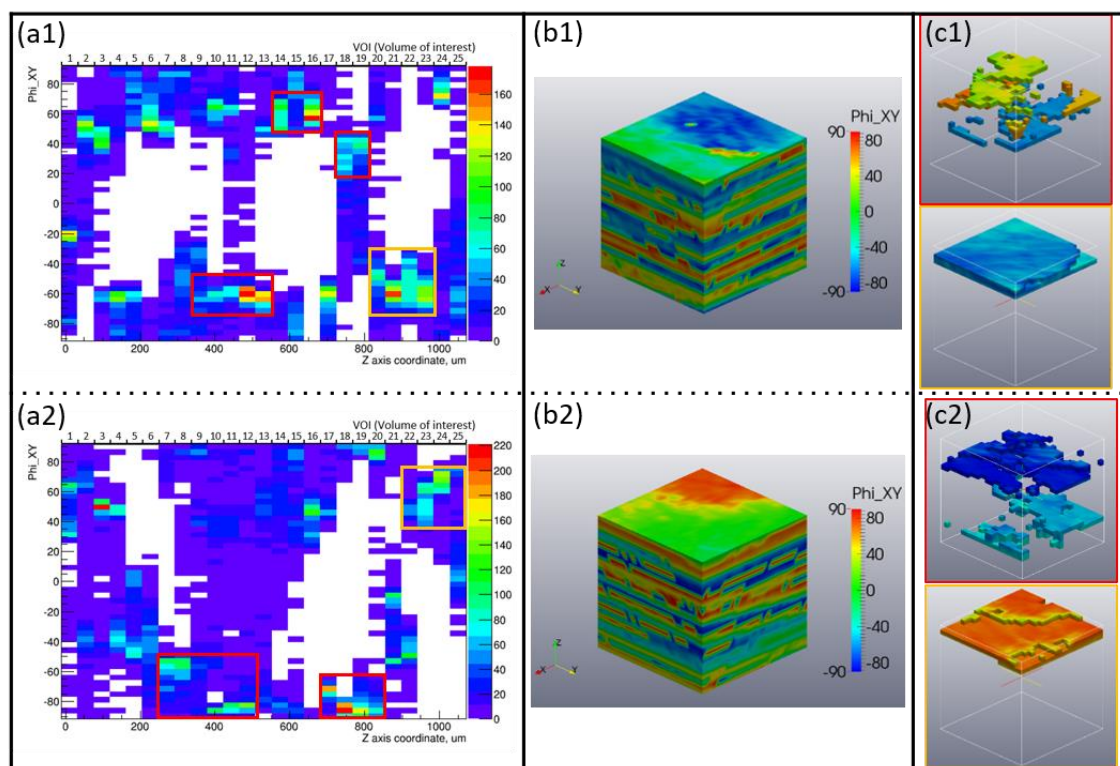
**Figure 2-30. Unfolded histograms of $\varphi_{XY}$ (a) and orientation-visualized 3D models (b, c) of two typical CTT-6&30 samples (the thresholded subset 3D models (c) correspond to the same-color boxes in (a)).**

As the tape length increases, the orientation cluster sizes decrease dramatically and the orientations of VOIs become more independent and concentrated. The independent small clusters like VOI 2-6, VOI 7-9 and VOI 10-14 in the CTT-18 samples (Figure 2-28 (a1)) as well as VOI 7-8 and VOI 10-11 in the CTT-30 samples (Figure 2-29 (a2)) showed independent adjacent orientation clusters. In addition, the subset models exhibited the corresponding layered tapes with totally different orientations (Figure 2-28 (c1), Figure 2-29 (c2)). The VOI 20-23 (Figure 2-28 (2)), VOI 7-8 and VOI 13-15 (Figure 2-29 (2)) clusters provided the orientation distributions and subset models of single tape morphologies, which cannot be found in the 6 mm samples. The subset model morphology of scattered clusters disappeared in the 18 mm and 30 mm samples, indicating that the tape interactions during the wet-type paper making process cause less breakage and damage in the case of longer tapes. When the 6 mm and 30 mm tapes were hybridized together, the internal structural geometry exhibited the combined morphologies of both of these tape lengths (Figure 2-30). The CTT-6&30 samples have both scattered clusters as observed in CTT-6

(histogram with red boxes in Figure 2-30 (a) and corresponding models in Figure 2-30 (c)) and concentrated tape layers (histogram with yellow boxes in Figure 2-30 (a) and corresponding models in Figure 2-30 (c)). This observation indicated that mixing the tape lengths leads to an apparent hybridization effect, wherein the internal geometric properties of both long and short tape lengths are retained in the resulting material structure.

Because CTT is transversely isotropic, the out-of-plane orientation $\theta_{XY}$ is expected to have an average value of 90°. However, the tape length also affects the width of the $\theta_{XY}$ distribution. The distribution histograms of $\theta_{XY}$ in the case of 15 samples of different tape lengths are plotted in Figure 2-31. As the tape length increases, $\theta_{XY}$ shows a more narrow distribution, and the standard deviation of the corresponding normal distribution fitting curve decreases. The $\theta_{XY}$ distribution histogram of CTT-6&30 show combined features of the 6 mm and 30 mm histograms, but is closer in character to the 30 mm result, analogous to the prior analysis of the $\varphi_{XY}$ distribution. The quantification of the $\theta_{XY}$ distribution can also provide internal geometric features like out-of-plane waviness, which can be further applied in the mechanical simulation of ROS composites for better simulation accuracy [84], and the detailed discussion of $\theta_{XY}$ distribution and out-of-plane waviness will be discussed in next section.

The tape length significantly affected the internal geometry of CTT. When the tape length is short, the existence of defects like scattered clusters or other structural irregularities will reduce the mechanical performance and result in primary damage. The similarity between the internal geometries of the CTT-18 and CTT-30 tapes indicated that improving the mechanical properties solely by increasing the tape length will reach a point of diminishing returns at a certain length, which also have been verified experimentally [79] and will be discussed in the next chapter.
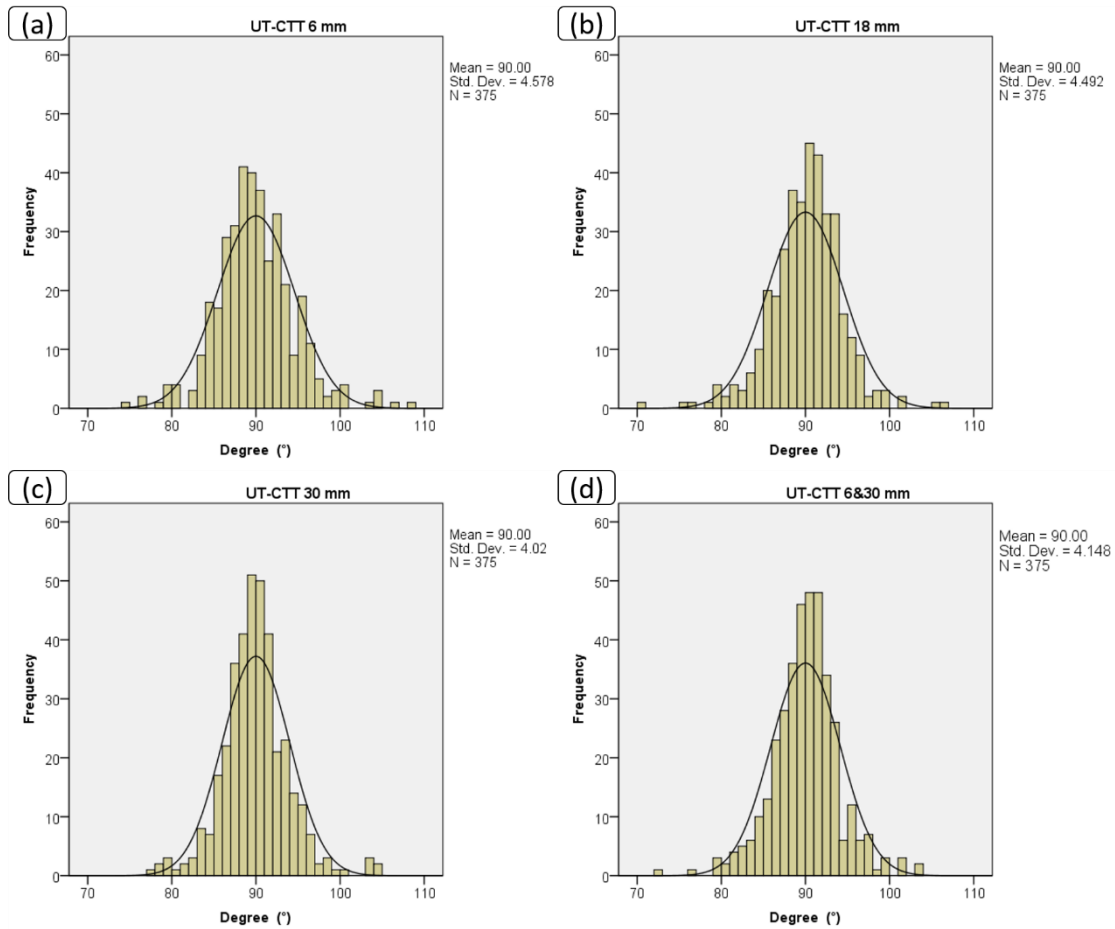
**Figure 2-31. Distribution histograms of out-of-plane orientation $\theta_{XY}$ of CTT with different tape lengths.**

### 2.4.3.3. Effect of tape thickness

The effect of tape lengths has been verified in the previous sub-section. In next step, the effect of tape thickness on the internal geometry of CTT is evaluated in detail.

Based on the previous studies, the tape thickness has great effects on the mechanical properties of CFRP composites [85, 86]. E specially in CTT, the tape thickness exhibit crucial effect on the tensile properties [78]. Consequently, the relationship between the internal geometry properties with the tensile properties of CTT with different thickness (CTT-18-Thin, CTT-18-Med and CTT-18-Thick) are to be evaluated using VoxTex method in this sub-section.

The tensile properties of CTT-18-Thin, CTT-18-Med and CTT-18-Thick have been evaluated in previous studies and the results of tensile moduli and tensile strengths are illustrated in Figure 2-32. The results indicated that with the increase of tape thickness, the modulus and strength decreased obviously, especially the tensile strength exhibit significant and linear decrease with the increase of tape thickness. Additionally, the coefficient of variation (CoV) of the samples with different thickness increased with the increase of tape thickness, and the coefficient of variation of CTT-18-Thick samples is markedly high compared with other two kinds of CTT.
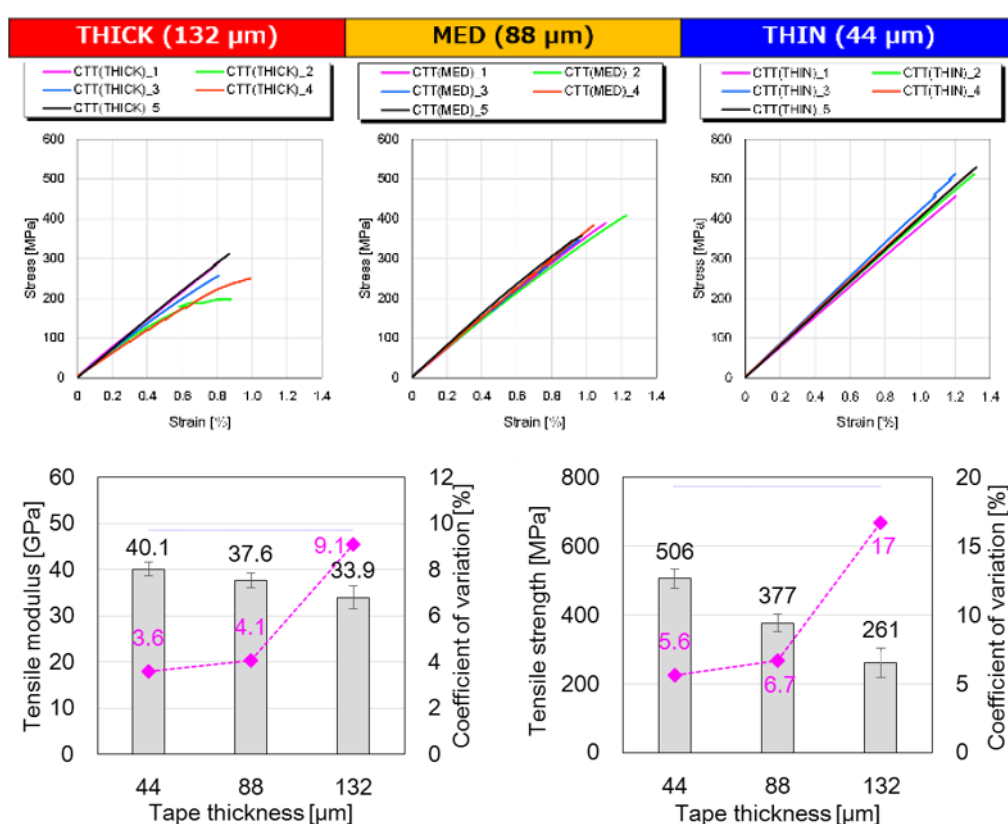


**Figure 2-32. Tensile properties of CTT-18-Thin, CTT-18-Med and CTT-18-Thick [78].**

To reveal the connection between the mechanical properties and the tape thickness, samples of CTT-18-Thin, CTT-18-Med and CTT-18-Thick were prepared for the X-ray micro-CT analysis. The VOI of all the CTT is fixed to 13 pixels as introduced before. Figure 2-33 illustrated the typical unfolded histogram of $\varphi_{XY}$, unfolded histogram of $\theta_{XY}$, and $\varphi_{XY}$-visualized 3D models of CTT-18-Thin, CTT-18-Med and CTT-18-Thick samples. From the figure, we can observe that

with the increase of tape thickness, the size of clusters in the unfolded histograms of $\varphi_{XY}$ also increased. This phenomenon is considered to be caused by the increased layer thickness, but from the histograms of CTT-18-Med and CTT-18-Thick, the clusters did not show the difference between 88 μm and 132 μm, but only subtle difference. The reason is the compression molding process for fabricating CTT can change the tape shape, especially in thick tape CTT. The unfolded histograms of $\theta_{XY}$ exhibit analogy result: the $\theta_{XY}$ concentration decreased with the increase of the tape thickness but the difference between CTT-18-Med and CTT-18-Thick is less apparent than the difference between CTT-18-Thin and CTT-18-Med. Additionally, the result of 3D model with visualized $\varphi_{XY}$ distribution also show this difference in layer separation between CTT-18 with different tape thickness. The change of tape thickness lead to the apparent change in $\theta_{XY}$ concertation, the $\theta_{XY}$ distribution is one of the most important factors for stress transfer and determination of the fracture of CTT materials [78]. Consequently, to give a quantified definition of $\theta_{XY}$ distribution can help understand the relationship between the mechanical properties and internal geometries of CTT. In this study, the out-of-plane waviness of CTT is defined based on the unfolded histogram of $\theta_{XY}$. Figure 2-34 illustrates the typical unfolded histogram of $\theta_{XY}$, because the $\theta_{XY}$ have a concertation close to 90° and certain range of distribution, the out-of-plane waviness of CTT is defined as a certain amplitude close to the distribution of $\theta_{XY}$ (red line in Figure 2-34). For efficient calculation, the out-of-waviness degree of CTT is calculated as the CoV of $\theta_{XY}$ collected by VoxTex.

The calculated out-of-waviness degrees of CTT with different thickness are compared with the tensile properties (moduli and strengths) together with their CoV in Figure 2-32, the results are plotted and illustrated in Figure 2-35. From the figure, a considerable linear relationship can be observed in both the tensile modulus as well as the tensile strength. Especially in the tensile strength, the out-of-plane waviness and tensile strength show high linearity. On the other side, the plots with the CoV of tensile properties and the out-of-plane waviness exhibit apparent concave down. This result verified the relationship between tensile properties and tape thickness in CTT (logically ROS-structured composites). We can speculate from this result that with the increase of tape thickness, the regularity of CTT's internal geometry decreased because of increased out-of-plane waviness, tape wrinkling and more resin rich areas due to the increased scale of tape boundary. These internal geometry irregularities (also can be considered as the structural defects of CTT) not only decrease the in-plane planarity which affect the tensile moduli but also play as the initial damage point in the materials. The linearity between the out-of-plane waviness and the tensile properties provide a new way for the modeling and numerical simulation of CTT for better accuracy with the consideration of internal geometry properties, this part will be discussed in detail in next chapter.

Finally, this sub-section introduced a methodology for the internal geometry analysis of CTT by VoxTex based micro-CT. It provides a convenient approach for quantified visualization modeling of the micro-3D structure with detailed multi-scale orientation information. The assessable features were summarized and listed in Table 2-3.
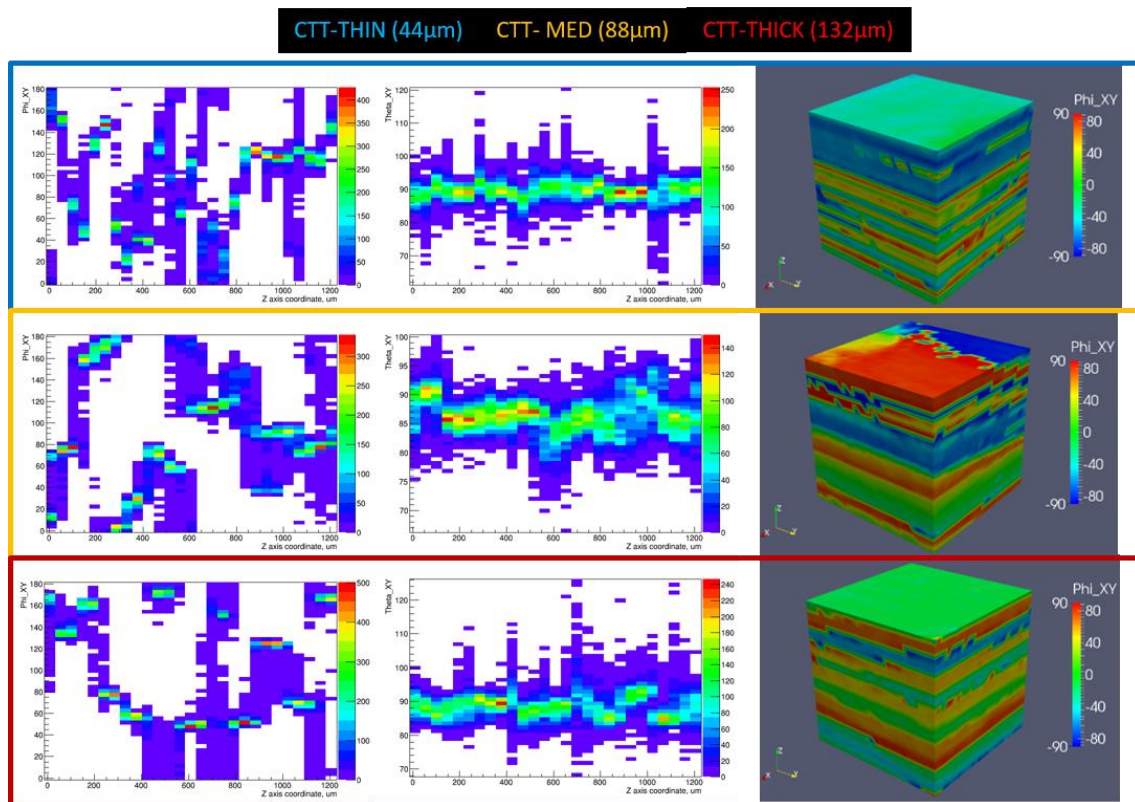


**Figure 2-33. Typical unfolded $\varphi_{XY}$ and $\theta_{XY}$ histograms and $\varphi_{XY}$-visualized 3D models of CTT-18-Thin, CTT-18-Med and CTT-18-Thick.**
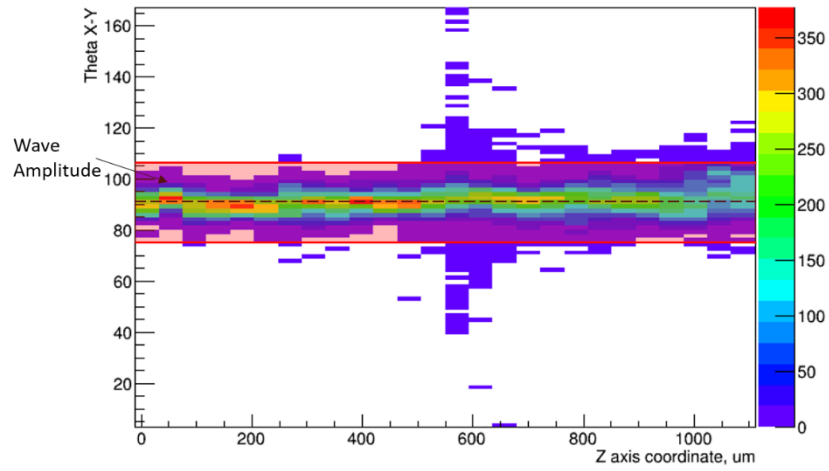
**Figure 2-34. Out-of-plane waviness of CTT.**
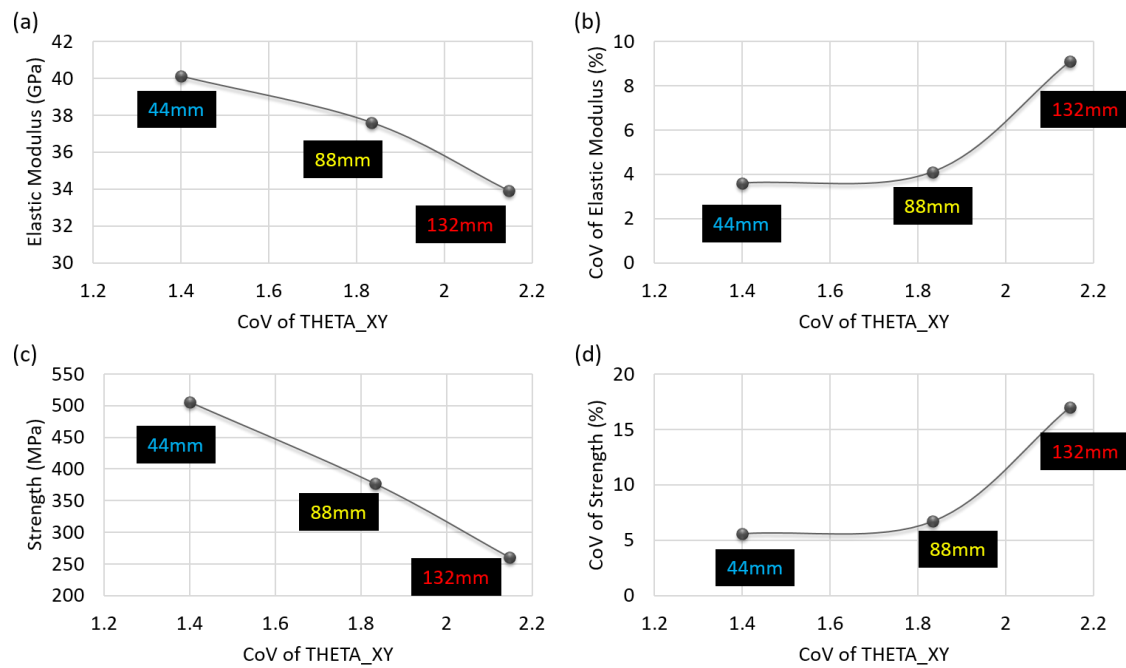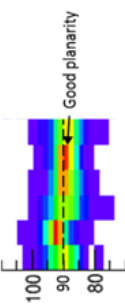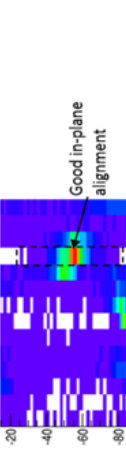


**Figure 2-35. The relationship between the tensile properties and their coefficient of variation (CoV) with the corresponding out-of-plane waviness (CoV of $\theta_{XY}$).**

**Table 2-3. Capability of VoxTex based X-ray micro-CT method.**

| Features | Required data | Example characterization | |
|---|---|---|---|
| Planarity of layers | Unfolded histograms of $\theta_{XY}$ | The layer have good planarity if the $\theta_{XY}$ of corresponding VOI is close to 90° |  |
| In-plane fiber deviations in the tapes | Unfolded histograms of $\varphi_{XY}$ | The fibers in tape have good in-plane alignment if the $\varphi_{XY}$ of corresponding VOI is concentrated to certain angle |  |
| Out-of-plane fiber deviations in the tapes | Unfolded histograms of $\theta_{XY}$ | The fibers in tape have good out-of-plane alignment if the $\theta_{XY}$ of corresponding VOI is concentrated to certain angle close to 90° |  |
| "splitting" of the tapes | Unfolded histograms of $\varphi_{XY}$ | Tape splitting was occurred if the $\varphi_{XY}$ of corresponding VOI is widespread and does not have significant concentration. |  |
| "sticking" of the tapes | Unfolded and quantified histograms of $\varphi_{XY}$ | Tapes in several layers are considered was stuck if the corresponding adjacent VOI exhibit cluster of $\varphi_{XY}$ distribution and the SD show similar value |  |
| Tape morphology after molding | Unfolded histograms of $\varphi_{XY}$ and 3D model | The integral, fractional and split tapes' morphology can be determined and built by combining the corresponding $\varphi_{XY}$ concentrations in the VOI with thresholded subsets of 3D model |  |

### 2.4.4. TRI/3D-BON

After the micro-CT analysis based on VoxTex method, the general image binarization based 3D-Bon method is used to conduct the comparative micro-CT analysis in this sub-section.

The VoxTex calculated the averaged orientation preference in a certain voxel based on the voxel model and VOI definition. On the other hand, the image binarization in 3D-BON is more focusing on labeling out the continuous gray value change (carbon fiber in composites). As a result, the 3D-BON is considered a more efficient method of the X-ray micro-CT analysis concerning the fiber-level morphology and provide better monofilament separation in 3D models.

To give a more specific comparison between the 3D-BON method and VoxTex method, the CMT-2 and CTT-12 specimens were prepared for the micro-CT analysis. Figure 2-36 illustrated the 3D models of CMT-2 and CTT-12 generated by 3D-BON, the fibers are separated from each other and marked with different colors. These model exhibit apparent difference with the VoxTex models (Figure 2-16 and Figure 2-17) that omit the fiber details. Consequently, comparing with the ROS-structured composites oriented VoxTex method, the 3D-BON have higher potential on internal geometry visualization for universal CFRP, especially in fiber-level.
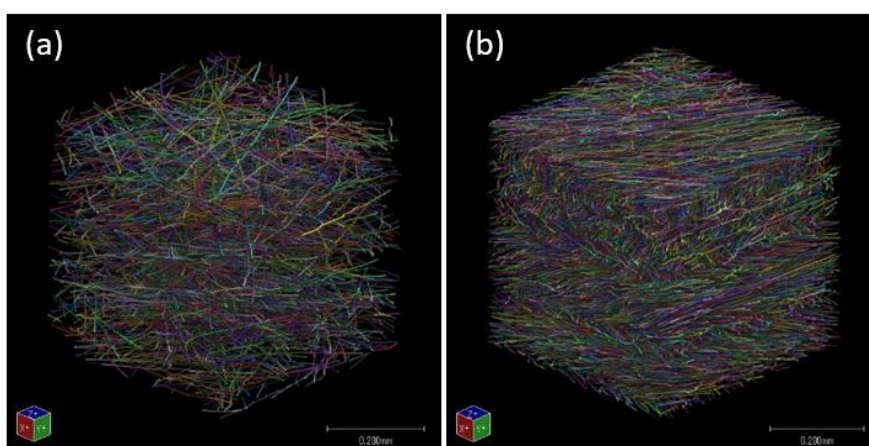


**Figure 2-36. Monofilament-separated 3D models of CMT-2 (a) and CTT-12 (b) generated by 3D-BON (fiber in the models are marked with different colors).**

In the next step, the $\varphi_{XY}$ and $\theta_{XY}$ distribution of CMT-2 and CTT-12 are calculated and combined with the 3D models. The results are illustrated in Figure 2-37. The original models are illustrated in panels (a1) and (b1) of Figure 2-37, and the $\varphi_{XY}$ and $\theta_{XY}$ distribution are quantified and indicated by a color scale as shown in Figure 2-37 (a2), (a3), (b2), and (b3). The structural models show obvious differences in internal geometries between the CMT and CTT. The CTT shows much higher fiber density, the fibers are straighter, and the structure is similar to that of a locally independent laminate. In contrast, the CMT model represents a typical mat-structure composite. The fiber orientation models also support this observation. Both the CMT-2 and the CTT-12 consist of randomly oriented fibers, but it is very clear from Figure 2-37 (b2) that the CTT have a visibly laminated structure, whereas the CMT is composed of randomly oriented carbon fibers (Figure 2-37 (a2)). In contrast, the out-of-plane fiber orientations of CMT-2 and CTT-12 have insignificant differences in that for both samples fibers are rarely oriented through the out-of-plane direction. In addition, the orientation cluster through out-of-plane direction of CTT observed in the VoxTex method cannot be recognized clearly in the $\varphi_{XY}$-visualized model in 3D-BON results (Figure 2-37 (b2)) because of the fibers in models decreased the capability for layer recognition.

The fiber orientation of CMT-2 and CTT-12 were calculated using 3D-BON, and the orientation tensors of all the materials were also calculated by the Equation 2-6. The averaged orientation tensors of CMT-2 and CTT-12 specimens are:

$$\boldsymbol{O_{CMT-2}} = \begin{bmatrix} 0.491 & -0.035 & -0.002 \\ -0.035 & 0.491 & 0.022 \\ -0.002 & 0.022 & 0.018 \end{bmatrix} \qquad \textbf{Equation 2-9}$$

$$\boldsymbol{O_{CTT-12}} = \begin{bmatrix} 0.496 & -0.063 & 0.005 \\ -0.063 & 0.496 & 0.002 \\ 0.005 & 0.002 & 0.008 \end{bmatrix} \qquad \textbf{Equation 2-10}$$

From the averaged orientation tensor of CMT-2 and CTT-12, the obvious difference can be found that the out-of-plane vector $v_{33}$ (refer to $\cos^2\theta$ in Equation 2-6) of CMT-2 is two times higher than CTT-12. Generally considering, with much higher $V_f$, the CTT-12 should have more out-of-plane orientation possibility as a random fiber system, but the opposite result provide a conclusion that the well-prepared (SM) CTT have better internal geometry regularity with lower out-of-plane

vector value.
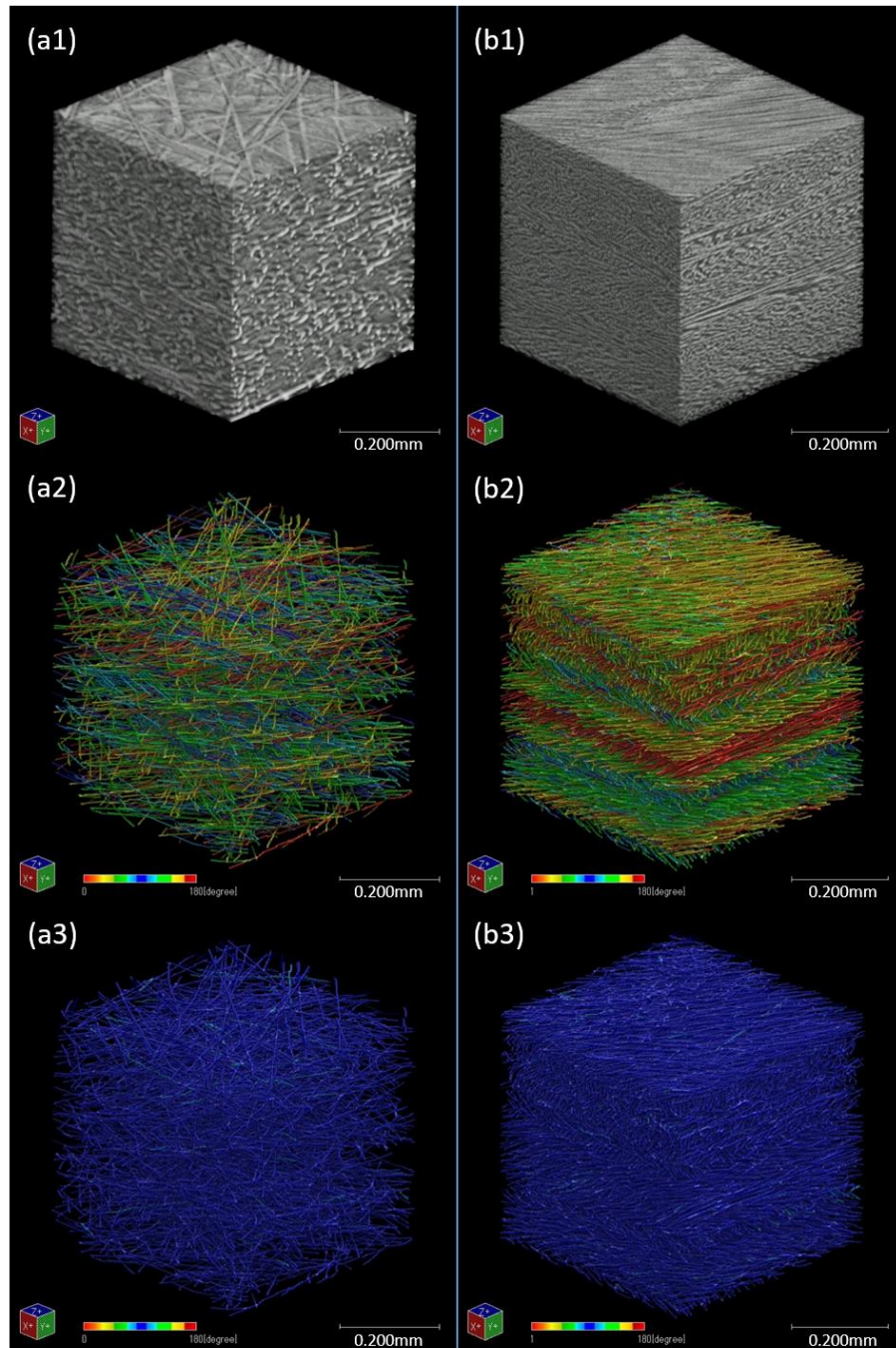


**Figure 2-37. Original 3D models (1), $\varphi_{XY}$ distribution visualized models (2), $\theta_{XY}$ distribution visualized models (3) of CMT-2 (a) and CTT-12 (b) (the color bar indicates the orientation angle degree).**

Furthermore, the averaged orientation tensors are regarded as the general representative orientation property and have been applied in the modeling and simulation of CFRP. The application of acquired orientation tensors on modeling and simulation of CMT and CTT will be discussed in detail in the next chapter.

Since the 3D-BON show different capability on the characterization of internal geometry properties, the comparison with VoxTex on same object material can help a better understanding of both the methodologies and the internal geometries. Introduced in the sub-section 2.4.3.3, internal geometries of CTT with three different thickness (i.e., CTT-18-Thin, CTT-18-Med and CTT-18-Thick) were evaluated and the relation between the internal geometries and the tensile properties were revealed. In comparison, the internal geometries of the same samples are also characterized using the 3D-BON method in this sub-section.

The orientation visualized 3D models of CTT-18-Thin, CTT-18-Med and CTT-18-Thick generated by 3D-BON are illustrated in Figure 2-38 and Figure 2-39. From the models, we can observe similar phenomenon with the VoxTex results that with the increase of tape thickness, the thickness of visible layers in the models increased, but the difference of layers thickness in models between CTT-18-Med and CTT-18-Thick is insignificant considering their tape thickness. And also the reason was clarified in sub-section 2.4.3.3 that the compression modeling effect on the tape morphology after molding mainly contributes to this appearance. Additionally, 3D-BON can provide more intuitive $\theta_{XY}$-visualized 3D models as shown in Figure 2-39. It is clear to find that with the increase of tape thickness, the out-of-plane oriented fibers (deviate from blue color that indicate 90°, and generally in green and red color in the samples) can be found more in the 3D models, which can help understand the orientation distribution change with the change of tape thickness.
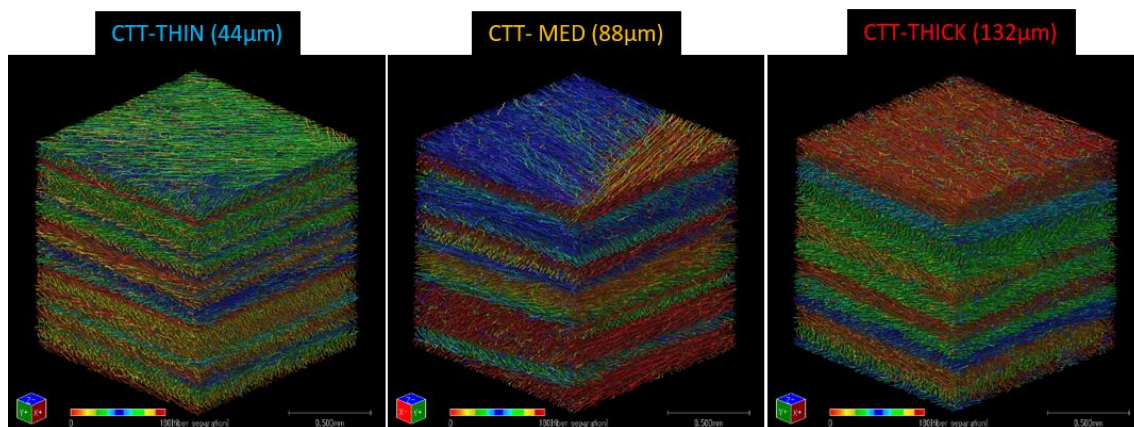
**Figure 2-38. Typical $\varphi_{XY}$-visualized 3D models of CTT-18-Thin, CTT-18-Med and CTT-18-Thick generated by 3D-BON.**
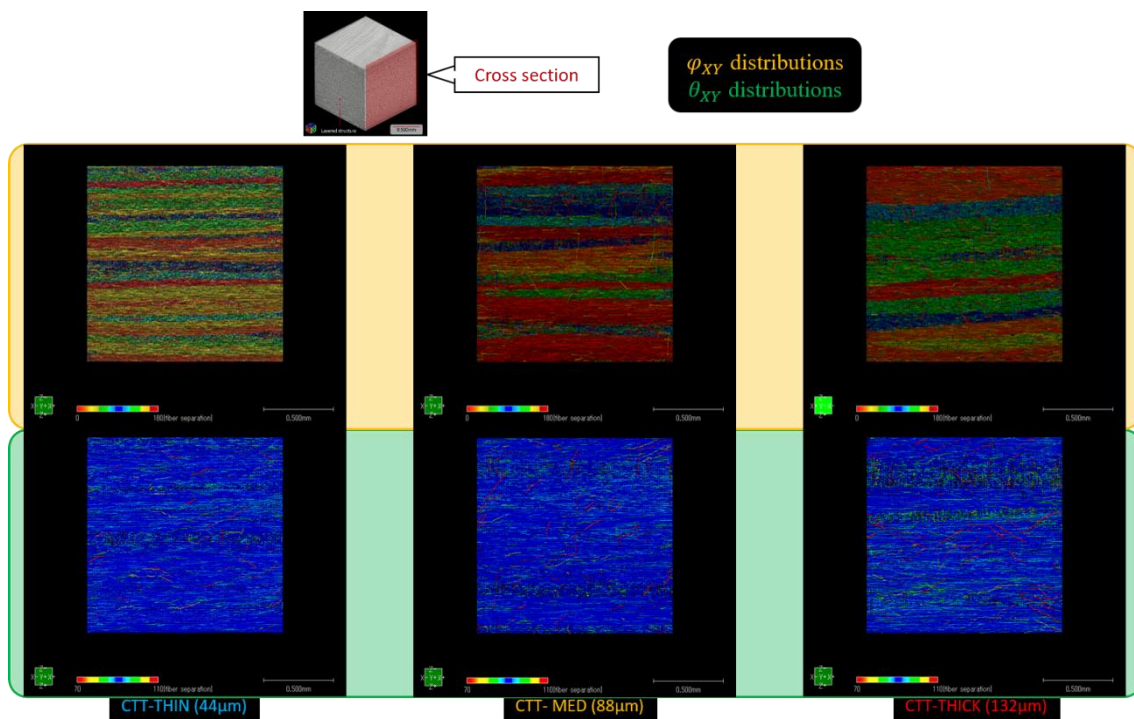


**Figure 2-39. Cross sections of typical 3D models of CTT-18-Thin, CTT-18-Med and CTT-18-Thick with visualized $\varphi_{XY}$ and $\theta_{XY}$ distributions.**

Moreover, to give a better quantification of the internal geometries using 3D-BON, the averaged orientation tensors of CTT-18-Thin, CTT-18-Med and CTT-18-Thick are calculated as below:

$$\boldsymbol{O_{CTT-18-Thin}} = \begin{bmatrix} 0.557 & 0.051 & -0.002 \\ 0.051 & 0.431 & -0.001 \\ -0.002 & -0.001 & 0.012 \end{bmatrix} \qquad \textbf{Equation 2-11}$$

$$\boldsymbol{O_{CTT-18-Med}} = \begin{bmatrix} 0.589 & -0.025 & -0.003 \\ -0.025 & 0.390 & -0.008 \\ -0.003 & -0.008 & 0.021 \end{bmatrix} \qquad \textbf{Equation 2-12}$$

$$\boldsymbol{O_{CTT-18-Thick}} = \begin{bmatrix} 0.463 & -0.009 & -0.002 \\ -0.009 & 0.491 & -0.005 \\ -0.002 & -0.005 & 0.046 \end{bmatrix} \qquad \textbf{Equation 2-13}$$

The averaged orientation tensors of CTT with different thickness have similar tendency with the out-of-plane waviness calculated through VoxTex method that the out-of-plane orientation vector $v_{33}$ increased with the increase of tape thickness. Hence, the relationship between the out-of-plane vector $v_{33}$ and the tensile properties are also plotted and the results are illustrated in Figure 2-40. The figure show some different result compared with the out-of-plane waviness (Figure 2-35).

From the figure, a considerable linear relationship can be observed between the tensile modulus and out-of-plane vector. But in the vector-strength plot, a concave down is found, which indicate the out-of-plane vector show a higher effect in the primary stage of increase. In the plots of the CoVs and the out-of-plane vector, the results are different from VoxTex. Both the CoV of tensile modulus and CoV of tensile strength show a considerable linear relationship with the out-of-plane vector $v_{33}$. This difference between 3D-BON and VoxTex on the tensile property fitting reveal the capability difference between these two methods. Consequently, for the further application of acquired internal geometry data on modeling and simulation, the 3D-BON and VoxTex results are considered to be suitable in different aspects.
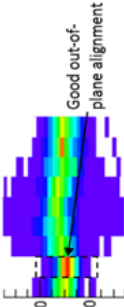
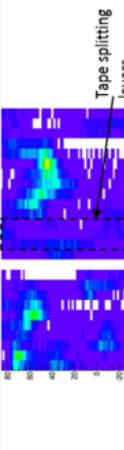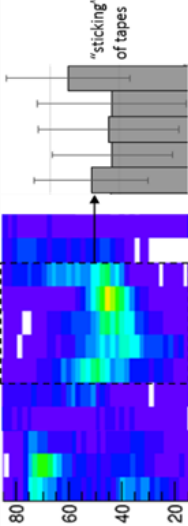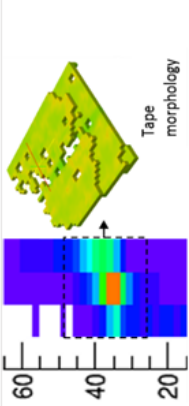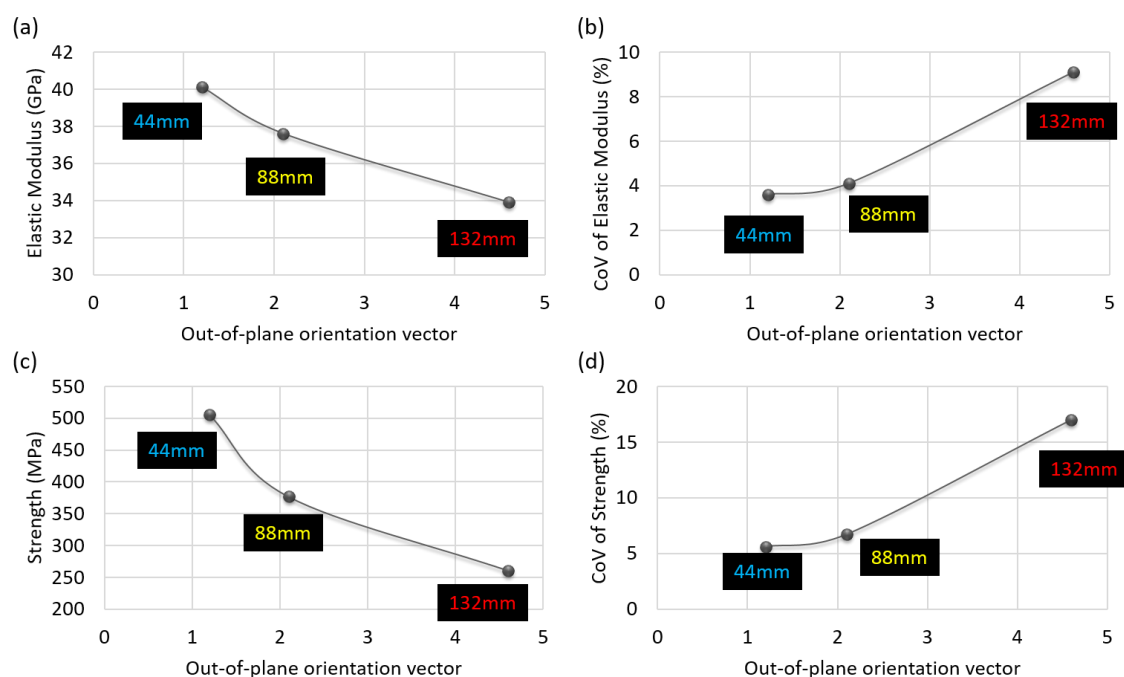**Figure 2-40. The relationship between the tensile properties and their coefficient of variation (CoV) with the corresponding out-of-plane orientation vector $v_{33}$.**

Additionally, because of the monofilament-separated modeling process in 3D-BON, the fiber-level detailed micro structure model of composites is possible to be generated. By exporting the 3D model, the CAD (computer-aided design) model of the corresponding composite can be generated combined with the mesh cutting process, which provide a possibility for a new approach of real-structure FEM analysis based on X-ray micro-CT (Figure 2-41). But at present, two main obstacles are still in the way for practical application. The first one is the problem about the significance of X-ray micro-CT analysis that was discussed in previous sub-sections, the real-structure CAD model also has the scale problem that restricted by the facility capability. The second one is the calculation efficiency. It is because even in the scanned X-ray volume with the physical size of 1.1×1.1×1.1 mm, the fiber density is still very high considering the 7 μm fiber diameter, and after the mesh cutting process the element number of the CAD model for FEM analysis is generally in million-scale, which is not efficient to run FEM simulation in laboratory level workstations. Hence, the real-structure FEM analysis based on X-ray micro-CT analysis is considered to need further development on the X-ray facility capabilities as well as the FEM methods, and therefore the detail discussion of this part will be omitted in the present study.
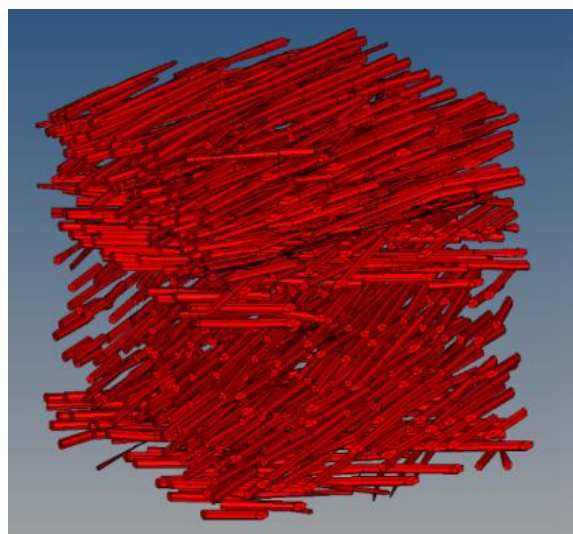
**Figure 2-41. CAD model sample of CTT-12 acquired from 3D-BON.**

## 2.5. Conclusions

In this chapter, the internal geometries of CMT and CTT, which are two kinds of DCFRTP with different components and fabrication processes, were evaluated in detail. Two different X-ray micro-CT methods, VoxTex method and TRI/3D-BON method, were developed in the micro-CT processes. The algorithm of image processing in VoxTex method based on the structure tensor calculation with a "voxel" definition, and in 3D-BON method based on the MIL concept image binarization. The VoxTex method is a brand new method developed in this study for the purpose of detailed internal geometry analysis of ROS-structured composites, and the comparison with general micro-CT analysis method 3D-BON method revealed the capability of different approaches on different DCFRTP.

The significance of required data is generally regarded as the crucial problem in X-ray micro-CT analysis of ROS composites, and this problem has been solved for the first time using a statistical multi-sample method in this study. The number for reliable X-ray micro-CT analysis of CTT has been decided.

The VoxTex method and 3D-BON method exhibited different capabilities on the quantification and visualization of internal geometries of CMT and CTT.

The "voxel model" based VOI definition and unfolded orientation histograms in VoxTex method bring an efficient approach for the analysis of layered properties in CTT. The effects of compression molding conditions, tape lengths and tape thicknesses on internal geometries of CTT were verified in detail. The micro structures were quantified and 3D models with visualized orientation distributions were generated. It was found that higher molding pressure will decrease the structure regularity due to the tape splitting, and the tape length exhibits positive effect on increase the layer independence through thickness direction. One of the crucial structural defects in ROS, the out-of-plane waviness, was defined and calculated using VoxTex data. The comparison between the out-of-plane waviness with the tensile properties of corresponding CTT with different tape thicknesses show considerable linearity and this relationship will be applied in the modeling and simulation in the next chapter.

The monofilament-separated image binarization process in 3D-BON method provided more detailed scale structural 3D models with visualized orientation distributions, and this method is considered more suitable for traditional DCFRTP like CMT. In contrast, the "fiber level" analysis also weakened layer-based evaluation capability, and less information can be acquired in the CTT micro-CT using 3D-BON method. However, using the fiber level detailed data, the averaged orientation tensors can be calculated using 3D-BON. As the representative orientation property, the orientation tensors are also applied for the modeling and simulation in the next chapter. The CTT with different tape thicknesses were also characterized using 3D-BON, and the relation between out-of-plane vector $v_{33}$ in the averaged orientation tensor with the tensile properties also show good agreement, but the out-of-plane vector in 3D-BON show better linearity with the CoV of tensile properties whereas the out-of-plane waviness in VoxTex show better linearity with the tensile properties themselves.

# **Note**

The contents of this Chapter are partially based on the following corresponding publications in the "**List of publications and awards**" listed at the end of this thesis:

(1) Journal Papers

〔Peer-reviewed〕

(1-2)     **Yi Wan** and Jun Takahashi, 'Deconsolidation behavior of carbon fiber reinforced thermoplastics', Journal of Reinforced Plastics and Composites, 2014, Vol. 33, No. 17, 1613-1624.

(1-4)     **Yi Wan**, Ilya Straumit, Jun Takahashi and Stepan V. Lomov, 'Micro-CT analysis of internal geometry of chopped carbon fiber tapes reinforced thermoplastics', Composites Part a-Applied Science and Manufacturing. 2016, Vol. 91, 211-221.

(1-5)     **Yi Wan** and Jun Takahashi, 'Tensile properties and aspect ratio simulation of transversely isotropic discontinuous carbon fiber reinforced thermoplastics', Composites sciences and technology. 2016, Vol. 137, 167-176.

〔Peer-reviewed    Under review *Italic under preparation*〕

(1-10)   **Yi Wan**, Ilya Straumit, Jun Takahashi and Stepan V. Lomov, 'Micro-CT analysis of the orientation unevenness in random chopped strand composites in relation to the strand length, Composites Part a-Applied Science and Manufacturing.

*(1-13)   **Yi Wan**, Ilya Straumit, Shinichiro Yamashita, Jun Takahashi and Stepan V. Lomov, 'Effect of internal geometry on the mechanical properties of chopped carbon fiber tapes reinforced thermoplastics with different tape thickness', Composites Part a-Applied Science and Manufacturing.*

*(1-14)   **Yi Wan**, Ilya Straumit, Hirofumi Suganuma, Yuto Nakashima, Jun Takahashi and Stepan V. Lomov, 'Internal geometry and mechanical properties of randomly oriented strands with different fabrication processes', Composites Part a-Applied Science and Manufacturing.*

(2) International Conference Proceeding：

〔peer-reviewed    ○: Presenter〕

(2-3)     ○ **Yi Wan**, Jun Takahashi and Isamu Ohsawa, 'Investigation about the springback effect on short fiber reinforced thermoplastics', the 13th Japan International SAMPE Symposium & Exhibition (JISSE13), 1802, Nagoya, Japan, (November 2013).

(2-4)     ○ **Yi Wan** and Jun Takahashi, 'Thermal deformation caused by residual stress in short

fiber reinforced thermoplastics', the 35th international conference of SAMPE Europe 2014 (SAMPE SEICO14), pp. 343-350, Paris, France, (March 2014).

(2-6)　　　○ **Yi Wan** and Jun Takahashi, 'Investigation of the deconsolidation effect of carbon mat reinforced thermoplastics', the 9th Asian-Australasian conference on composite materials (ACCM9), I-004, Suzhou, China, (October 2014).

(2-10)　　○ **Yi Wan**, Toshiro Ohori and Jun Takahashi, 'Mechanical properties and modeling of discontinuous carbon fiber reinforced thermoplastics', the 20th International Conference on Composite Materials (ICCM20), 3222-4, Copenhagen, Denmark, (July 2015).

(2-11)　　○ ワンイー, 髙橋淳, '森・田中理論を用いた CTT 材の最適テープ長決定方法', 日本複合材料学会第４０回複合材料シンポジウム, B1-09, 金沢, (2015 年 9 月).

(2-15)　　○ **Yi Wan** and Jun Takahashi, 'CFRTP mechanical properties simulation by Mori-Tanaka model and equivalent laminate methods', the 17th European Conference on Composite Materials (ECCM17), TUE-4_BIA_3.09-02, Munich, Germany, (June 2016).

(2-19)　　○ **Yi Wan** and Jun Takahashi, 'Modeling analysis and evaluation of tensile properties of discontinuous CFRTP using homogenization and de-homogenization methods', 2016 SAMPE International Education Program, The composites and advanced materials EXPO (CAMX), Anaheim, California, (September 2016).

(2-20)　　○ ワンイー, 髙橋淳, '熱可塑性樹脂複合材料のランダム配向ストランド（ROS）の微視的構造の定量化と可視化', 第 8 回日本複合材料会議, 東京,(2016年3月).

〔peer-reviewed　○: Presenter　Accepted〕

(2-21)　　○ **Yi Wan** and Jun Takahashi, 'Two micro CT methods analysis of internal geometry of randomly oriented strands', 3rd International Conference on Tomography of Materials and Structure), Lund, Sweden, (June 2017).

(2-22)　　○ **Yi Wan** and Jun Takahashi, 'Multi-scale internal geometry analysis and mechanical modeling of randomly oriented strands', the 21st International Conference on Composite Materials (ICCM21), Xi'an, China, (August 2017).

(2-26)　　○ **Yi Wan** and Jun Takahashi, 'Internal geometry analysis and mechanical property simulation of randomly oriented strands', the 15th European-Japanese Meeting on Composite Materials, London, UK, (September 2017).

# Chapter 3.   Mechanical Properties

## 3.1.  Introduction

In Chapter 3, the mechanical properties of DCFRTP are evaluated experimentally and analytically.

Adequate characterizations of the mechanical properties of DCFRTP required appropriate simulation methods combine with acquisition and analysis of components' properties. Based on the review in Chapter 1, Mori-Tanaka method and equivalent laminate method are considered to be the adequate methods for accurate and efficient simulation of mechanical properties of DCFRTP. In this chapter, these two methods are adopted for the material modeling of CMT and CTT with different fabrication processes and components. The theoretical basis and algorithms are introduced in detail, and the internal geometry properties of the corresponding composites characterized in Chapter 2 are applied in the modeling processes. The simulation results are compared with the experimental value of the tensile properties. Capabilities and application orientations of both the methods are evaluated at the end.

## 3.2. Specimens

The specimens for the tensile experiments and simulation modeling are prepared in this study.

To give a comprehensive study of the mechanical properties, the two CMT with different $V_f$ (CMT-1 and CMT-2) and four CTT with different tape length fabricated under 5 MPa molding pressures (CTT-12, CTT-18, CTT-24 and CTT-30) were prepared for the present study.

Five specimens were prepared for each kind of material. The CMT specimens were 1 mm in thickness and cut to 25 mm in width and the distance between end tabs was 80 mm with a 25 mm extensometer to measure accurate strain change. On the other hand, to eliminate the tape size effect in CTT, the specimens were molded to a 2 mm thickness and cut to a width of 35 mm. The distance between the end tabs was 100 mm, and a 50 mm extensometer was used.

To acquire sufficient data for simulation modeling, the tensile experiments on the PP and PA6 matrix materials were also conducted to obtain the elastoplastic performance parameters needed for the simulations. The dumbbell tensile specimens were manufactured with the corresponding resins used in the CMT (PP) and CTT (PA6) using injection molding processes (Hand Truder PM-1, TOYO SEIKI Co., Ltd.), and the tensile stroke rate was set to 1 mm/min. Because the fracture strains of these resins are much higher (higher than 30%) than those of the CF (about 2%) and the composites (less than 2%), a maximum strain of the matrix materials of only 5% was recorded by the 25 mm extensometer (MTS Systems Corp.) to ensure measurement accuracy.

Tensile tests were conducted using a universal testing machine (AUTOGRAPH AG-X plus, Shimadzu Co., Ltd.). The tensile experiment conditions of CMT and CTT were partially followed the JIS K 7073 (1.0 mm/min tensile test speed), and the tensile strengths were taken as the maximum stress before final breaking occurred. The detailed test conditions were listed in Table 3-1. After the specimens were broken, the fractographic analysis was conducted using a microscope (VHX−1000, Keyence Co., Ltd.). In addition, the tensile tests of the corresponding resins used in the CMT (PP) and CTT (PA6) were conducted following the standard JIS K 7113.

**Table 3-1. Tensile test conditions of CMT and CTT.**

| Materials | CMT | | CTT | |
|---|---|---|---|---|
| Reference standard | JIS K 7073 | | | |
| Testing machine | AUTOGRAPH AG-Xplus 250kN (Shimadzu Co.) | | | |
| Loading speed | 1 mm/min | | 1 mm/min | |
| Sample number | 5 | | 5 | |
| Specimen size | Width: | 25 mm | Width: | 35 mm |
| | Thickness: | 1.0 mm | Thickness: | 2.0 mm |
| | Length: | 150 mm | Length: | 200 mm |
| Extensometer | Gauge length: 25 mm (MTS Systems Corp.) | | Gauge length: 50 mm (MTS Systems Corp.) | |

## 3.3. Methods

Two different analytical simulation modeling methods were applied in the present study to evaluate the tensile properties of CMT and CTT. The general mean-field homogenization Mori-Tanaka (MT) method was conducted using the software Digimat (MSC Software Corporation) [87], and the de-homogenization equivalent laminate (EL) method was conducted with the software MCQ (AlphaSTAR Corporation) [67]. The algorithms of these two methods are introduced in this section. Also, the fiber orientation distribution (FOD) acquired in the previous chapter together with the fiber length distribution of CMT, equivalent aspect ratio calculation of CTT and plasticity fitting of the matrices are studied in this section.

### 3.3.1. General micromechanics of composite materials

The basic considerations in MT method and partially in EL method established on the mean-field homogenization methods, which were developed from the general micromechanics of heterogeneous materials. In this sub-section, the micromechanics applied in the present study were introduced.

General heterogeneous materials are considered to have micro structure consisting of a matrix material and multiple phases of so-called "inclusions", which can be short fibers, platelets, micro-cavities or micro-cracks (Figure 3-1). The objective of micromechanical modeling is to predict the interaction between the micro structure and the macroscopic (or overall or effective) properties.
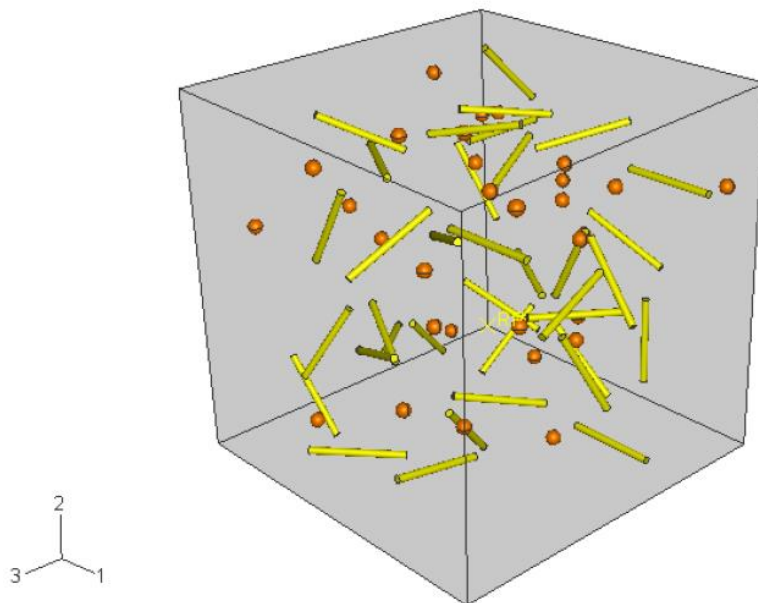


**Figure 3-1. Matrix material reinforced with multiple phases of inclusions [87].**

Consider a heterogeneous solid body whose microstructure consists of a matrix material and inclusions, subjected to given loads and boundary conditions (BCs). The objective is to predict the influence of the microstructure on the response of the body. It is computationally prohibitive to solve the mechanical problem if only focusing on the scale of the microstructure. Therefore, two scales are distinguished: the microscopic one that of the heterogeneities and the macroscopic one where the solid can be seen as locally homogeneous. Consider $x$ as the position vector. When a composite is loaded, the stress field $\sigma(x)$ and the corresponding strain field $\varepsilon(x)$ will be non-uniform on the microscopic conditions. To reveal these non-uniform fields is a formidable problem and consequently average stress and strain were introduced to obtain useful results [69, 88].

To conduct effective averaging of stress and strain, an element work as the link between the two scales is generally generated based on the concept of representative volume element (RVE) with

volume $V$. At macro scale, each material point is supposed to be the center of a RVE, which should be sufficiently large to represent the underlying heterogeneous microstructure, and small with respect to the size of the solid body (Figure 3-2).
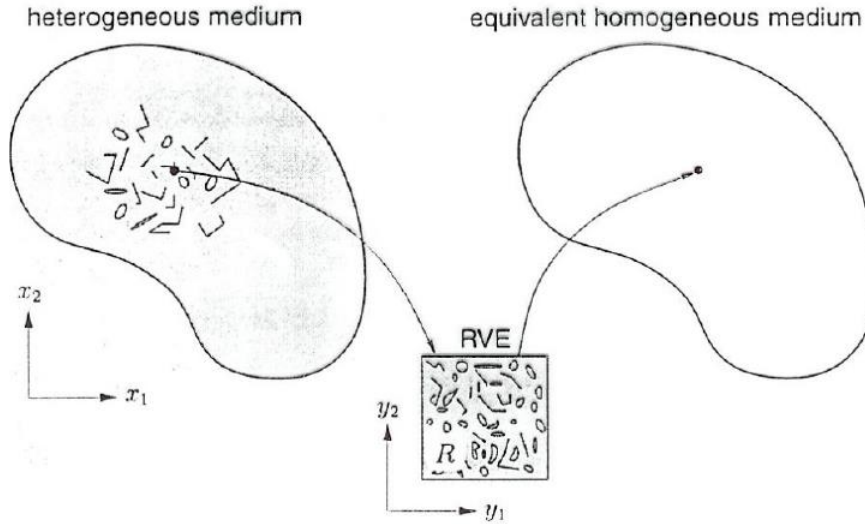


**Figure 3-2. Micro-macro transition. Upper left: microscopic scale, upper right: macroscopic scale, bottom: representative volume element (RVE) [89]**

The volume-averaged stress $\overline{\sigma}$ is defined as the averaged of the pointwise stress filed $\sigma(x)$ over the volume $V$:

$$\overline{\sigma} \equiv \frac{1}{V}\int_{V} \sigma(x)dV \qquad \textbf{Equation 3-1}$$

And the average strain $\overline{\varepsilon}$ is defined in the same way.

In the DCFRTP evaluated in this study (i.e. CMT and CTT), the void content is neglectable and the volume of fiber $(V^f)$ and the volume of matrix $(V^m$ or $V - V^f)$ can be used for the calculation of the average fiber and matrix stresses:

$$\overline{\sigma}^f \equiv \frac{1}{V^f}\int_{V^f} \sigma(x)dV \ \ and \ \ \overline{\sigma}^m \equiv \frac{1}{V^m}\int_{V^m} \sigma(x)dV \qquad \textbf{Equation 3-2}$$

Also the average strains for the fiber and matrix are defined similarly.

Therefore, the relationships between the fiber and matrix averages and the overall averages can be derived from these definitions that:

$$\bar{\sigma} = V_f \bar{\sigma}^f + V_m \bar{\sigma}^m \hspace{4cm} \textbf{Equation 3-3}$$

$$\bar{\varepsilon} = V_f \bar{\varepsilon}^f + V_m \bar{\varepsilon}^m \hspace{4cm} \textbf{Equation 3-4}$$

where $V_f$ and $V_m$ are the volume fractions of fiber and matrix respectively and $V_f + V_m = 1$.

An important related result named average strain theorem is given by Hill [88]. In this theorem, considering the averaging volume $V$ is subjected to surface displacement $u^0(x)$ consistent with a uniform strain $\varepsilon^0$. Then the average strain within the region is

$$\bar{\varepsilon} = \varepsilon^0 \hspace{4cm} \textbf{Equation 3-5}$$

This theorem is proved by substituting the definition of the strain tensor $\varepsilon$ in terms of the displacement vector $u$ into the definition of average strain $\bar{\varepsilon}$, and applying Gauss's theorem as:

$$\bar{\varepsilon}_{ij} \equiv \frac{1}{V} \int_S (u_i^0 n_j + n_i u_j^0) ds \hspace{3cm} \textbf{Equation 3-6}$$

where $s$ is the surface of $V$ and $n$ is unit vector normal to $ds$. The average strain within volume $V$ is totally determined by the displacements on the surface of the volume, so the uniform strain displacements must produce identical volume of average strain. That is, consider a difference between the average strain with the local strain $\varepsilon^D(x)$:

$$\varepsilon^D(x) = \varepsilon(x) - \bar{\varepsilon} \hspace{3.5cm} \textbf{Equation 3-7}$$

then there must be:

$$\bar{\varepsilon}^D = \frac{1}{V} \int_V \varepsilon^D(x) dV = 0 \hspace{3cm} \textbf{Equation 3-8}$$

For the average stress, this theorem is also valid that:

$$\bar{\sigma} = \sigma^0 \hspace{4cm} \textbf{Equation 3-9}$$

The micromechanics models are built for predicting the average mechanical properties of composites, and careful definitions are needed. The direct approach provided by Hashin is adopted in the present study [69, 90].

Consider the average stiffness of the composite as a tensor $C$, subject the $V$ of RVE to surface displacements consistent with a uniform strain $\varepsilon^0$, then using the $C$ to mapping this uniform strain to the average stress based on Equation 3-5, we can have:

$$\bar{\sigma} = C\bar{\varepsilon} \hspace{4cm} \textbf{Equation 3-10}$$

The average compliance $S$ (different from the surface $s$) is defined as $S = C^{-1}$, and having that:

$$\bar{\varepsilon} = S\bar{\sigma} \hspace{4cm} \textbf{Equation 3-11}$$

based on Equation 3-9.

An important concept, first introduced by Hill [88], that about the idea of strain and stress concentration tensors $\boldsymbol{A}$ and $\boldsymbol{B}$ is also introduced at this section. These tensors are used to describe the ratio between the average fiber strain (stress) with the corresponding averages strain (stress) in the composite:

$$\bar{\boldsymbol{\varepsilon}}^f = \boldsymbol{A}\bar{\boldsymbol{\varepsilon}}$$   **Equation 3-12**

$$\bar{\boldsymbol{\sigma}}^f = \boldsymbol{B}\bar{\boldsymbol{\sigma}}$$   **Equation 3-13**

$\boldsymbol{A}$ and $\boldsymbol{B}$ are fourth-order tensors and calculated from the microscopic strain (stress) fields.

For convenient, an alternate strain concentration tensor $\widehat{\boldsymbol{A}}$ is also introduced to describe the relation between the average fiber strain to the average matrix strain [69]:

$$\bar{\boldsymbol{\varepsilon}}^f = \widehat{\boldsymbol{A}}\bar{\boldsymbol{\varepsilon}}^m$$   **Equation 3-14**

Consequently:

$$\boldsymbol{A} = \frac{\widehat{\boldsymbol{A}}}{\left[(1 - V_f)\boldsymbol{I} + V_f\widehat{\boldsymbol{A}}\right]}$$   **Equation 3-15**

for the interchange between $\boldsymbol{A}$ and $\widehat{\boldsymbol{A}}$ ($\boldsymbol{I}$ is the fourth-order unit tensor).

Combining Equation 3-3, Equation 3-4, Equation 3-10 and Equation 3-12, the average stiffness of composite can be expressed based on the strain concentration tensors $\boldsymbol{A}$ and fiber and matrix properties:

$$\boldsymbol{C} = \boldsymbol{C}^m + V_f(\boldsymbol{C}^f - \boldsymbol{C}^m)\boldsymbol{A}$$   **Equation 3-16**

Similar for the average compliance:

$$\boldsymbol{S} = \boldsymbol{S}^m + V_f(\boldsymbol{S}^f - \boldsymbol{S}^m)\boldsymbol{B}$$   **Equation 3-17**

Using the Equation 3-16 and Equation 3-17, the basic upper and lower boundaries of composite modulus can be calculated based on the Voigt average model and Reuss average model, respectively [69, 88, 90, 91]. The Voigt average assumes that the fiber and the matrix both subjected the same uniform strain, which means that $\bar{\boldsymbol{\varepsilon}}^f = \bar{\boldsymbol{\varepsilon}}$, $\boldsymbol{A} = \boldsymbol{I}$, and the modulus of composite is:

$$\boldsymbol{C}^{Voigt} = \boldsymbol{C}^m + V_f(\boldsymbol{C}^f - \boldsymbol{C}^m) = V_f\boldsymbol{C}^f + V_m\boldsymbol{C}^m$$   **Equation 3-18**

based on Equation 3-16.

While the Reuss average assumes that the fiber and the matrix both subjected the same uniform stress, which means that $\overline{\boldsymbol{\sigma}}^{\mathrm{f}} = \overline{\boldsymbol{\sigma}}$, $\boldsymbol{B} = \boldsymbol{I}$, and the modulus of composite is:

$$\boldsymbol{S}^{Reuss} = \boldsymbol{S}^m + V_f\left(\boldsymbol{S}^f - \boldsymbol{S}^m\right) = V_f\boldsymbol{S}^f + V_m\boldsymbol{S}^m \qquad \textbf{Equation 3-19}$$

Based on these preliminary studies of the micromechanics of composite materials, the mean-filed homogenization methods are introduced in the next sub-section.

### 3.3.2. Mean-field homogenization Mori-Tanaka method

The problem of homogenization in micromechanics of composites can be stated under a continuum mechanics viewpoint that, at the macro scale, in each macro material point, if we know the macro strain, we need to compute the macro stress, and vice-versa (Figure 3-3).
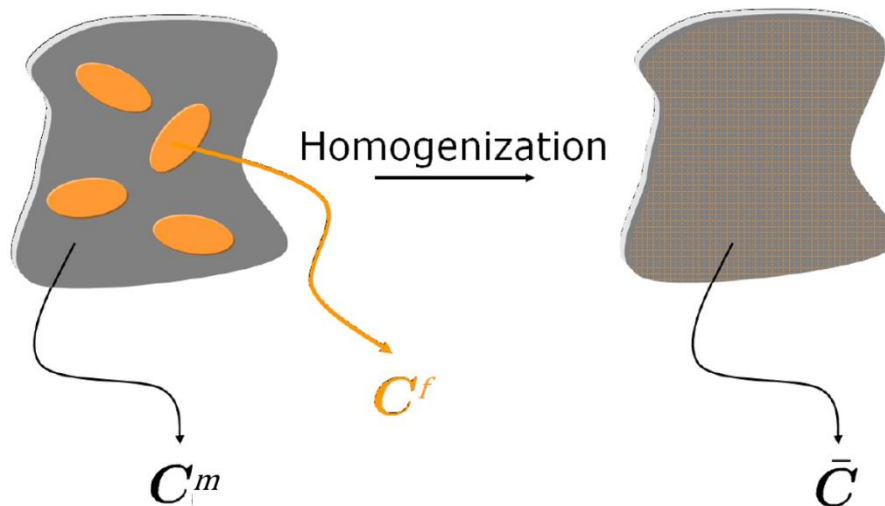


**Figure 3-3. Homogenization in linear elasticity. Left: heterogeneous material under given boundary conditions (BCs). Right: equivalent homogeneous material having the same effective stiffness under the same BCs [87].**

This is the fundamental problem of homogenization in linear elasticity: find an equivalent homogeneous material which has the same effective macro stiffness as the real heterogeneous composite, under the same boundary conditions. There are a few scale-transition methods which address this problem: asymptotic or mathematical homogenization theory, method of cells, sub-cells and transformation field analysis, direct finite element analysis, and mean-field homogenization (MFH). The MFH method is generally considered as a high efficient semi-

analytical method and is applied in the present study.

The purpose of MFH method is to compute approximate but accurate estimates of the volume averages of the stress and strain fields. It is important to emphasize that MFH does not solve the RVE (micromechanics) problem in detail, and therefore does not compute the detailed micro stress and strain fields in each phase.

Regarded as the fundamental result in several different models of MFH methods, the Eshelby's equivalent inclusion [92, 93] was developed as a solution for the elastic stress field in and around an ellipsoidal particle in an infinite matrix. Approximating the cylindrical fiber as an elongated ellipsoid, the Eshelby's result can be used to model the stress and strain fields around fiber reinforced composites.

In Eshelby's result, a homogeneous inclusion problem is posed first to describe the idea (Figure 3-4). Inside a stress-free infinite solid body with uniform stiffness $\boldsymbol{C^m}$, a particular small region is cut out and regarded as the inclusion with the rest part regarded as the matrix. Adding some type of transformation on the inclusion, then a uniform strain $\boldsymbol{\varepsilon^T}$ (named as the transformation strain or the eigenstrain) would be generated with no surface traction and stress. Then put the transformed inclusion back to the cut-out area of the matrix, this transformation would bring some non-uniform strain field $\boldsymbol{\varepsilon^C(x)}$ in the whole body which relative to its shape before the transformation [94]. Within the matrix, the stress is calculated using the uniform stiffness tensor:

$$\boldsymbol{\sigma^m(x) = C^m \varepsilon^C(x)} \qquad \textbf{Equation 3-20}$$

While in the inclusion, the strain $\boldsymbol{\varepsilon^C}$ is regarded uniform and the inclusion stress is uniform as:

$$\boldsymbol{\sigma^I = C^m(\varepsilon^C - \varepsilon^T)} \qquad \textbf{Equation 3-21}$$

The key result from Eshelby was revealed that within an ellipsoidal inclusion, the strain $\boldsymbol{\varepsilon^C}$ is related to the transformation strain $\boldsymbol{\varepsilon^T}$ by:

$$\boldsymbol{\varepsilon^C = E\varepsilon^T} \qquad \textbf{Equation 3-22}$$

where $\boldsymbol{E}$ is the Eshelby's tensor, and it depends only on the aspect ratio of inclusion and the matrix elastic constants. Detailed derivation and further applications have been given by Mura [95] and other researchers [96-99].

$\varepsilon^C(x)$

$\varepsilon^T$
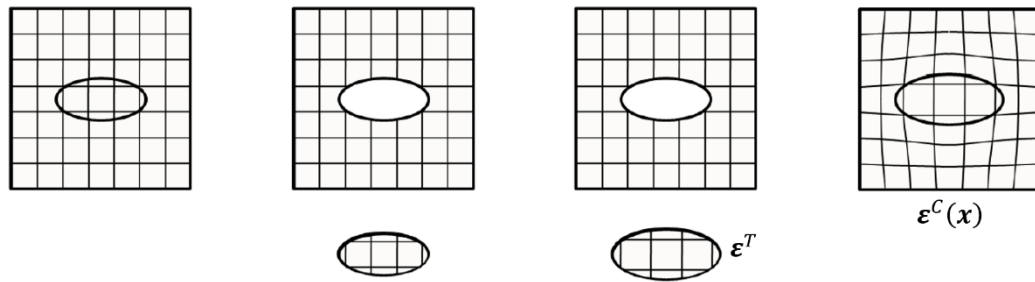
**Figure 3-4. Eshelby's inclusion problem: cut off an ellipsoidal volume from an infinite solid body with uniform stiffness, adding a transformation on the inclusion and put it back [87].**

In the next step, Eshelby provided an equivalence between the homogeneous inclusion problem introduced above with inhomogeneous inclusion (Figure 3-5). Consider two infinite bodies of matrix with same stiffness $C^m$, one has a homogeneous inclusion with certain transformation strain $\varepsilon^T$, and another has an inhomogeneous inclusion with no transformation strain but different stiffness $C^f$. Subject both two bodies with a uniform strain $\varepsilon^A$ at infinity. What needs to be found is the transformation strain $\varepsilon^T$ that give the two inclusions same stress and strain distributions.
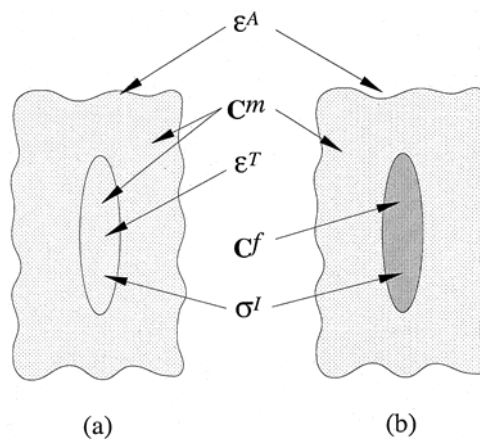


**Figure 3-5. Eshelby's equivalent inclusion problem: two bodies with different inclusion stiffness, find the $\varepsilon^T$ to satisfy the identical stress and strain distribution under far-field strain $\varepsilon^A$ [69].**

For the homogeneous inclusion one, the inclusion stress is calculated with the applied strain based on the Equation 3-21:

$$\sigma^I = C^m(\varepsilon^A + \varepsilon^C - \varepsilon^T) \qquad \textbf{Equation 3-23}$$

91

While in the inhomogeneous inclusion problem, because there is no $\varepsilon^{\mathrm{T}}$ but different stiffness $\boldsymbol{C}^{\mathrm{f}}$, the stress is:

$$\sigma^{I} = \boldsymbol{C}^{f}(\varepsilon^{A} + \varepsilon^{C}) \qquad \textbf{Equation 3-24}$$

Considering a fiber reinforced composite. Based on the Equation 3-16, find the strain concentration tensor $\boldsymbol{A}$ can help bring the stiffness of the composite. Therefore, consider far-field strain $\varepsilon^{A}$ is identical to the average strain of the composite:

$$\bar{\varepsilon} = \varepsilon^{A} \qquad \textbf{Equation 3-25}$$

Also because the strain in the fiber is uniform, based on Equation 3-10 and Equation 3-24, we have:

$$\varepsilon^{f} = \varepsilon^{A} + \varepsilon^{C} \qquad \textbf{Equation 3-26}$$

Combine the Equation 3-23 and Equation 3-24 to consider the situation of equivalence between the stresses in the homogeneous and the inhomogeneous inclusions:

$$\boldsymbol{C}^{f}(\varepsilon^{A} + \varepsilon^{C}) = \boldsymbol{C}^{m}(\varepsilon^{A} + \varepsilon^{C} - \varepsilon^{T}) \qquad \textbf{Equation 3-27}$$

Using the Equation 3-22, Equation 3-25 and Equation 3-26 to reveal the relationship between $\bar{\varepsilon}$ and $\varepsilon^{\mathrm{f}}$:

$$\varepsilon^{f} = \frac{\bar{\varepsilon}}{\left[I + \frac{E}{C^{m}}(C^{f} - C^{m})\right]} \qquad \textbf{Equation 3-28}$$

Based on Equation 3-12, the strain concertation tensor for Eshelby's equivalent inclusion is then:

$$A^{Eshelby} = \frac{1}{\left[I + \frac{E}{C^{m}}(C^{f} - C^{m})\right]} = \left[I + ES^{m}(C^{f} - C^{m})\right]^{-1} \qquad \textbf{Equation 3-29}$$

Inputting Equation 3-29 in Equation 3-16, the stiffness of fiber reinforced composite can be calculated [100]. Using these equations to evaluate the effects of inclusion's aspect ratio on stiffness was studied by Chow et. al. [101].

However, the Eshelby's result only focused on a single inclusion surrounded by infinite matrix, the more complicated problem is to find the way to consider multiple inclusions (fibers) inside the matrix and the interactions between fibers as well as to the matrix for high accuracy results. Under these considerations, the Mori-Tanaka (MT) method is introduced.

Mori and Tanaka provided an original proposal to solve the multi-inclusion problem in the mean-field homogenization [74], and Benveniste extended the proposal to provide simplified and practical Mori-Tanaka approach [75].

Considering an average applied stress $\overline{\sigma}$, there is a reference strain $\varepsilon^0$, which is defined as the strain in a homogeneous body of matrix under this stress:

$$\overline{\sigma} = C^m \varepsilon^0 \qquad\qquad \textbf{Equation 3-30}$$

However, in a short fiber reinforced composite system, the average matrix strain $\overline{\varepsilon}^{\mathbf{m}}$ differs from the reference strain because of the fibers interaction. And this difference is described using a perturbation strain $\tilde{\varepsilon}^{\mathbf{m}}$:

$$\overline{\varepsilon}^m = \varepsilon^0 + \tilde{\varepsilon}^m \qquad\qquad \textbf{Equation 3-31}$$

In addition, a fiber in the composite should have another additional perturbation strain $\tilde{\varepsilon}^{\mathbf{f}}$ considering the inclusion process:

$$\overline{\varepsilon}^f = \varepsilon^0 + \tilde{\varepsilon}^m + \tilde{\varepsilon}^f \qquad\qquad \textbf{Equation 3-32}$$

Combined with Equation 3-27, the equivalent inclusion solution of this short fiber composite should also consider the transformation strain $\varepsilon^{\mathrm{T}}$, and the relation between the fibers and matrix become:

$$C^f\left(\varepsilon^0 + \tilde{\varepsilon}^m + \tilde{\varepsilon}^f\right) = C^m\left(\varepsilon^0 + \tilde{\varepsilon}^m + \tilde{\varepsilon}^f - \varepsilon^T\right) \qquad\qquad \textbf{Equation 3-33}$$

We can find that the $\varepsilon^{\mathrm{A}}$ in Equation 3-27 is related to $\varepsilon^0 + \tilde{\varepsilon}^{\mathbf{m}}$ in Equation 3-33 and the $\tilde{\varepsilon}^{\mathbf{f}}$ related to $\varepsilon^{\mathrm{C}}$. Combined with Equation 3-22, we also have:

$$\tilde{\varepsilon}^f = E\varepsilon^T \qquad\qquad \textbf{Equation 3-34}$$

Consequently, regarding Equation 3-31, Equation 3-32 and Equation 3-34, we can make an assumption that in multi-fiber system, the far-field strain of each fiber $\overline{\varepsilon}$ is considered to be identical to the average strain of the matrix itself $\overline{\varepsilon}^{\mathbf{m}}$. This indicated that in a composite, each inclusion regards the average matrix strain as the far field strain in the local aspect and this is the assumption in Mori-Tanaka method.

From the Equation 3-29 and Equation 3-12, we can find that:

$$\overline{\varepsilon}^f = A^{Eshelby}\overline{\varepsilon} \qquad\qquad \textbf{Equation 3-35}$$

While in the Mori-Tanaka method, the relation based on the assumption is:

$$\bar{\varepsilon}^f = A^{Eshelby}\bar{\varepsilon}^m \qquad \text{Equation 3-36}$$

Also consider the strain concentration tensor in Mori-Tanaka method we have:

$$\bar{\varepsilon}^f = A^{MT}\bar{\varepsilon} \qquad \text{Equation 3-37}$$

Combined with the Equation 3-14 and Equation 3-15, the relationship between $A^{MT}$ and $A^{Eshelby}$ become:

$$\widehat{A}^{MT} = A^{Eshelby} \qquad \text{Equation 3-38}$$

and

$$A^{MT} = \frac{A^{Eshelby}}{\left[(1 - V_f)I + V_f A^{Eshelby}\right]} \qquad \text{Equation 3-39}$$

This is the basic equation in Mori-Tanaka method, and consequently, the stiffness of a short fiber composite is calculated in Mori-Tanaka method with the combination of Equation 3-16, Equation 3-29 and Equation 3-39:

$$C = C^m + V_f\Big(C^f - C^m\Big)\Big\{\Big[(1 - V_f)I + \frac{V_f}{[I + ES^m(C^f - C^m)]}\Big][I + ES^m(C^f - C^m)]\Big\}^{-1} \qquad \text{Equation 3-40}$$

In addition, to consider the orientation properties in the stiffness, the orientation tensor introduced in the previous section is applied in the Mori-Tanaka method as it is not possible and necessary to quantify the orientation of each fiber in the composite [102]. The orientation tensors are theoretically given in terms of the orientation vector that is parallel to the fiber axis and defined over the RVE.

The orientation dependent stiffness of composite $C^o_{ijkl}$ in the coordinate system $x_1, x_2, x_3$ is related to the stiffness $C^{o'}_{pqrs}$ in the local fiber coordinate system through the transformation rule of fourth-order tensors as:

$$C^o_{ijkl} = p_{ip}p_{jq}p_{kr}p_{ls}C^{o'}_{pqrs} \qquad \text{Equation 3-41}$$

where the $p$ is from the fiber orientation distribution function in the Euler angles $\psi(p)$ in Equation 2-8.

To obtain the weighted orientation average stiffness, the integration operation is conducted to the stiffness tensor with the fiber orientation distribution function $\psi(p)$ based on the Equation 2-7:

$$\overline{C}^o_{ijkl} = \int_0^{2\pi} \int_0^{2\pi} p_{ip} p_{jq} p_{kr} p_{ls} C^{o\prime}_{pqrs} \psi(p) dp \qquad \textbf{Equation 3-42}$$

Consequently, the stiffness calculated from Mori-Tanaka method with the consideration of orientation tensor can be expressed in terms of an orientation dependent part and an orientation independent part, of which the orientation dependent part comes from the Equation 3-42:

$$C_{ijkl} = C^1_{ijkl} + \overline{C}^o_{ijkl} \qquad \textbf{Equation 3-43}$$

where the orientation independent stiffness of composite $C^1_{ijkl}$ is calculated from the Mori-Tanaka method by Equation 3-40.

The orientation tensors used for the MT method modeling of CMT and CTT in the present study are all calculated by the 3D-BON method introduced in Chapter 2.

Moreover, the fiber length is also considered in the Mori-Tanaka method in this study. But for CTT material, the fiber length is fixed in a certain value in each kind of tape length, so only in CMT exists the fiber distribution. To simplify the calculation, the fiber length of CMT is counted as a pointwise distribution and the average value of stiffness is calculated integrally.

Because only the tensile properties were considered in this study, the component failures were considered as maximum stress based component failure indicators of the fibers and matrices during the simulations:

$$f^f = \frac{\sigma_{ij}{}^f}{X_{ij}{}^f} \qquad \textbf{Equation 3-44}$$

$$f^m = \frac{\sigma_{ij}{}^m}{X_{ij}{}^m} \qquad \textbf{Equation 3-45}$$

where $f^f$ and $f^m$ are the failure indicators of fibers and matrices, respectively. $\sigma^f$ and $\sigma^m$ are the stress states of fibers and matrices in direction $ij$, $X^f$ and $X^m$ are the strengths of fibers and matrices in the corresponding stress direction. The failure indicators $f$ are real-valued functions comparing a given stress state $\sigma$ combination to strengths $X$. They are written in a normalized dimensionless form in such a way that an indicator value smaller than 1 means a safe state, while failure is deemed to occur as soon as the chosen indicator reaches or exceeds 1.

In this study, the focus was on the simulation of tensile properties of DCFRTP, and this uniaxial

stress state ensures the applicability of simple component failure indicators. The fiber strengths are provided by the corresponding manufacturers. Because the matrix materials are homogeneous, the axial tensile strength, in-plane tensile strength, and transverse shear strength are regarded as having the same value. However, the strength of the matrices is difficult to determine because the fracture strains of the resins are much higher than those of the fibers and composites. The equivalent matrix strength $\sigma_m^*$ is therefore determined as the mean tensile stress in the matrix at the fiber breaking strain [103]. Additionally, when the strength under complex stress conditions is studied, failure criteria such as those reported previously [104, 105] should also be taken into consideration.

For convenient modeling and calculating in the simulation of Mori-Tanka method in the present study, a software Digimat-MF (MSC Software Corporation) integrated the functions based on the introduction of Mori-Tanka method in this sub-section is adopted.

### 3.3.3.    Equivalent laminate method

Because the general mean-filed homogenization methods only compute the approximate estimates of the volume averages of the stress and strain fields and neglect the RVE (micromechanics) problem in detail, the subtle features of short fiber composites are ignored in the Mori-Tanaka method. Efforts have been made to conduct more accurate modeling of DCFRTP in decades. Especially with the development of ROS composites, the complex internal geometries of this kind of materials bring difficulties in the traditional mean-filed homogenization approaches.

Under this situation, a new kind approach based on the classical laminate theory (CLT) together with micromechanics is developed and called the equivalent laminate (EL) method aimed at high accuracy modeling of DCFRTP [67, 84].

Although the algorithm of EL methods differ from each other (generally in the micromechanics modeling), the main progress of the approach are the same. As illustrated in Figure 3-6, the EL method generally using micromechanics models (Mori-Tanaka, Shear-lag, etc.) to modeling the composite in each layer or the hypothetical layer if the DCFRTP have no apparent layered-structure. After the layer modeling, the entire composite is modeled based on CLT together with the consideration of other material features like internal geometry defects (out-of-plane waviness, agglomeration, etc.). Because the CLT process in EL method is generally regarded as the opposite operation compared with the homogenization process, the EL method is also called as the "De-

Homogenization" method (Figure 3-7).

In the present study, the software MCQ (AlphaSTAR Corporation) integrated the micromechanics method derived by Tandon and Weng [106] combining the Eshelby's theory and modified MT model is adopted for the EL modeling.
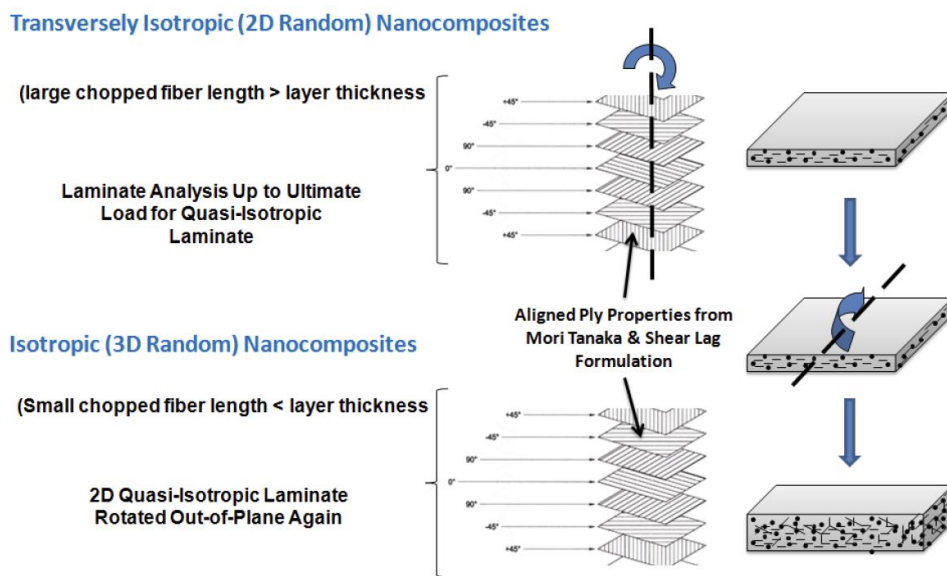


**Figure 3-6. General approach of equivalent laminate (EL) method [67].**
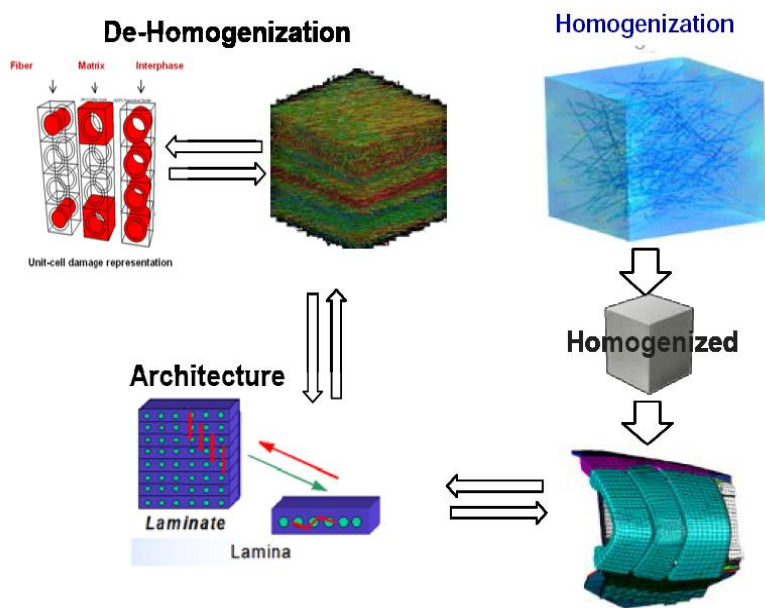


**Figure 3-7. Homogenization process and De-Homogenization (equivalent laminate) process [84].**

The modified MT method provided by Tandon and Weng [106] developed equations for the complete set of elastic constants of a short-fiber composite. Regarding the fourth-order stiffness tensor of both the fiber and matrix are taken to be isotropic, they can be written as:

$$C_{ijkl}^m = \lambda^m \delta_{ij}\delta_{kl} + \mu^m(\delta_{ik}\delta_{jl} + \delta_{il}\delta_{jk}) \qquad \textbf{Equation 3-46}$$

$$C_{ijkl}^f = \lambda^f \delta_{ij}\delta_{kl} + \mu^f(\delta_{ik}\delta_{jl} + \delta_{il}\delta_{jk}) \qquad \textbf{Equation 3-47}$$

where $\lambda^m$, $\mu^m$ and $\lambda^f$, $\mu^f$ are the Lamé's constants of the matrix and inclusions, respectively, and $\delta_{ij}$ is the Kronecker delta, having the property $\delta_{ij} = 1$ when $i = j$ and $\delta_{ij} = 0$ when $i \neq j$.

In addition, combined the Equation 3-25 and Equation 3-26 in the Eshelby's equivalent inclusion problem, we can get the $\varepsilon_{ij}^T$ represented in terms of $\varepsilon_{ij}^A$:

$$\varepsilon_{ij}^T = \frac{\left(C_{ijkl}^m - C_{ijkl}^f\right)}{\left[C_{ijkl}^m + \left(C_{ijkl}^f - C_{ijkl}^m\right)\right]}\varepsilon_{kl}^A \qquad \textbf{Equation 3-48}$$

And in the Mori-Tanaka assumption, $\varepsilon_{ij}^A$ is identical to $\varepsilon_{ij}^m$. Combined with Equation 3-29 and Equation 3-40, set $ij = 11$, 22 and 33 firstly, based on Equation 3-46 and Equation 3-47 we can have:

$$D_1\varepsilon_{11}^m + \varepsilon_{22}^m + \varepsilon_{33}^m + B_1\varepsilon_{11}^T + B_2\varepsilon_{22}^T + B_2\varepsilon_{33}^T = 0 \qquad \textbf{Equation 3-49}$$

$$\varepsilon_{11}^m + D_1\varepsilon_{22}^m + \varepsilon_{33}^m + B_3\varepsilon_{11}^T + B_4\varepsilon_{22}^T + B_5\varepsilon_{33}^T = 0 \qquad \textbf{Equation 3-50}$$

$$\varepsilon_{11}^m + \varepsilon_{22}^m + D_1\varepsilon_{33}^m + B_3\varepsilon_{11}^T + B_5\varepsilon_{22}^T + B_4\varepsilon_{33}^T = 0 \qquad \textbf{Equation 3-51}$$

where

$$B_1 = V_f D_1 + D_2 + (1 - V_f)(D_1 E_{1111} + E_{2211} + E_{2211}) \qquad \textbf{Equation 3-52}$$

$$B_2 = V_f + D_3 + (1 - V_f)(D_1 E_{1122} + E_{2222} + E_{2233}) \qquad \textbf{Equation 3-53}$$

$$B_3 = V_f + D_3 + (1 - V_f)(E_{1111} + E_{2211} + D_1 E_{2211}) \qquad \textbf{Equation 3-54}$$

$$B_4 = V_f D_1 + D_2 + (1 - V_f)(E_{1122} + D_1 E_{2222} + E_{2233}) \qquad \textbf{Equation 3-55}$$

$$B_5 = V_f + D_3 + (1 - V_f)(E_{1122} + E_{2222} + D_1 E_{2233}) \qquad \textbf{Equation 3-56}$$

where $\boldsymbol{E}_{\text{ijkl}}$ is the Eshelby's tensor and

$$D_1 = 1 + \frac{2(\mu^f - \mu^m)}{(\lambda^f - \lambda^m)} \qquad \textbf{Equation 3-57}$$

$$\boldsymbol{D}_2 = \frac{(\lambda^m + 2\mu^m)}{(\lambda^f - \lambda^m)} \qquad \textbf{Equation 3-58}$$

$$\boldsymbol{D}_3 = \frac{\lambda^m}{(\lambda^f - \lambda^m)} \qquad \textbf{Equation 3-59}$$

Solving Equation 3-49, Equation 3-50 and Equation 3-51 simultaneously, the $\boldsymbol{\varepsilon}_{11}^T$, $\boldsymbol{\varepsilon}_{22}^T$ and $\boldsymbol{\varepsilon}_{33}^T$ cab be obtained:

$$\boldsymbol{\varepsilon}_{11}^T = \frac{[A_1 \boldsymbol{\varepsilon}_{11}^m - A_2(\boldsymbol{\varepsilon}_{22}^m + \boldsymbol{\varepsilon}_{33}^m)]}{A} \qquad \textbf{Equation 3-60}$$

$$\boldsymbol{\varepsilon}_{22}^T = \frac{[2A_3 \boldsymbol{\varepsilon}_{11}^m - (A_4 + A_5 A)\boldsymbol{\varepsilon}_{22}^m + (A_4 - A_5 A)\boldsymbol{\varepsilon}_{33}^m]}{2A} \qquad \textbf{Equation 3-61}$$

$$\boldsymbol{\varepsilon}_{33}^T = \frac{[2A_3 \boldsymbol{\varepsilon}_{11}^m - (A_4 - A_5 A)\boldsymbol{\varepsilon}_{22}^m + (A_4 + A_5 A)\boldsymbol{\varepsilon}_{33}^m]}{2A} \qquad \textbf{Equation 3-62}$$

where

$$A = 2B_2 B_3 - B_1(B_4 + B_5) \qquad \textbf{Equation 3-63}$$

$$A_1 = D_1(B_4 + B_5) - 2B_2 \qquad \textbf{Equation 3-64}$$

$$A_2 = (1 + D_1)B_2 - (B_4 + B_5) \qquad \textbf{Equation 3-65}$$

$$A_3 = B_1 - D_1 B_3 \qquad \textbf{Equation 3-66}$$

$$A_4 = (1 + D_1)B_1 - 2B_3 \qquad \textbf{Equation 3-67}$$

$$A_5 = \frac{(1 - D_1)}{(B_4 - B_5)} \qquad \textbf{Equation 3-68}$$

Similarly, setting $ij = 12$, $\boldsymbol{\varepsilon}_{12}^T$ is:

$$\varepsilon_{12}^{T} = \frac{\varepsilon_{12}^{m}}{\frac{\mu^{m}}{\mu^{f} - \mu^{m}} + V_{f} + 2(1 - V_{f})E_{1212}}$$

**Equation 3-69**

and for $\varepsilon_{13}^{T}$ and $\varepsilon_{23}^{T}$ is in the same fashion.

Based on the equations above, the elastic constants can be calculated. There are five independent elastic constants associated with the transversely isotropic composites (i.e., CMT and CTT in present study). These are the longitudinal Young's modulus $E_{11}$, the transverse Young's modulus $E_{33}$, the in-plane shear modulus $G_{12}$, the out-of-plane shear modulus $G_{13}$, and the plane-strain bulk modulus $K_{23}$.

For instance, to determine the longitudinal Young's modulus $E_{11}$, applying the $\overline{\sigma}_{11}$ and set other $\overline{\sigma}_{ij} = 0$. The 11-component of Equation 3-10 is:

$$\overline{\sigma}_{11} = E_{11}\overline{\varepsilon}_{11}$$

**Equation 3-70**

The strain components in the comparison material from Equation 3-30 are:

$$\varepsilon_{11}^{m} = \frac{\overline{\sigma}_{11}}{E^{m}}, and \ \varepsilon_{22}^{m} = \varepsilon_{33}^{m} = \frac{-\nu^{m}\overline{\sigma}_{11}}{E^{m}}$$

**Equation 3-71**

where $\nu^{m}$ and $E^{m}$ are the Poisson's ratio and Young's modulus of the matrix, respectively.

Then, from Equation 3-28, Equation 3-60, Equation 3-70 and Equation 3-71, $E_{11}$ is calculated:

$$E_{11} = \frac{E^{m}}{1 + \frac{V_{f}(A_{1} + 2\nu^{m}A_{2})}{A}}$$

**Equation 3-72**

Similarly, other elastic constants in the CMT and CTT are calculated following these procedures.

In addition, the waviness in the fiber orientation distribution is also considered in the EL method. The method to calculate the effective elastic modulus of composites containing fiber waviness is provided by Shi et al. [107]. In this method, the way to calculate the curved fiber is to separate the curved area to infinitesimal segmentations (Figure 3-8). Consider a fiber with waviness embedded in the matrix subject to the average matrix stress $\overline{\sigma}^{m}$ in the far-field. The fiber is curved around $x_3$ axis in a certain coordinate system $O - x_1x_2x_3$ (which is independent to the general coordinate system, Figure 3-8(a)). Then, the strain in the infinitesimal fiber (Figure 3-8 (b)) is approximated by that in a long and straight fiber of the same orientation embedded in the matrix and the matrix is subjected to $\overline{\sigma}^{m}$ (Figure 3-8(c)). The fiber is along $x_2'$ axis in the local coordinate system $O - x_1'x_2'x_3'$, with Euler angles $\varphi$ and $\theta$, where $\varphi$ is the angle between $x_1$

and $x_1'$ and $\theta$ is the angle between $x_3$ and $x_3'$. Consequently, the average strain in the curved fiber is obtained by integrating with respect to the angle $\varphi$. Regarding the strain of an infinitesimal segment in the curved fiber $\boldsymbol{\varepsilon}^f(\theta, \varphi)$, the strain can be related to the stress $\overline{\boldsymbol{\sigma}}^m$ in Mori-Tanaka method based on Equation 3-36 and Equation 3-11:

$$\boldsymbol{\varepsilon}^f(\theta, \varphi) = \boldsymbol{A}^{Eshelby}(\theta, \varphi)\boldsymbol{\varepsilon}^m = \boldsymbol{A}^{Eshelby}(\theta, \varphi)\boldsymbol{S}^m\overline{\boldsymbol{\sigma}}^m \qquad \textbf{Equation 3-73}$$

For the curved fiber, the average strain $\overline{\boldsymbol{\varepsilon}}^f$ can be obtained from the integration of $\boldsymbol{\varepsilon}^f(\theta, \varphi)$:

$$\overline{\boldsymbol{\varepsilon}}^f(\theta) = \frac{1}{\varphi_l}\left[\int_0^{\varphi_l} \boldsymbol{A}^{Eshelby}(\theta, \varphi)\boldsymbol{S}^m d\varphi\right]\overline{\boldsymbol{\sigma}}^m \qquad \textbf{Equation 3-74}$$

where $\varphi_l$ is the total polar angle along the fiber. Similarly, the average stress $\overline{\boldsymbol{\sigma}}^f$ in curved fiber is given by:

$$\overline{\boldsymbol{\sigma}}^f(\theta) = \frac{1}{\varphi_l}\left[\int_0^{\varphi_l} \boldsymbol{C}^f(\theta, \varphi)\boldsymbol{A}^{Eshelby}(\theta, \varphi)\boldsymbol{S}^m d\varphi\right]\overline{\boldsymbol{\sigma}}^m \qquad \textbf{Equation 3-75}$$

The average stress and strain tensors in the composite can then be written in terms of $\overline{\boldsymbol{\sigma}}^m$ based on Equation 3-3 and Equation 3-4 as:

$$\overline{\boldsymbol{\sigma}} = \left[\frac{V_f}{\varphi_l}\int_0^{\varphi_l} \boldsymbol{C}^f(\theta, \varphi)\boldsymbol{A}^{Eshelby}(\theta, \varphi)\boldsymbol{S}^m d\varphi + \left(1 - V_f\right)\boldsymbol{I}\right]\overline{\boldsymbol{\sigma}}^m \qquad \textbf{Equation 3-76}$$

$$\overline{\boldsymbol{\varepsilon}} = \left[\frac{V_f}{\varphi_l}\int_0^{\varphi_l} \boldsymbol{A}^{Eshelby}(\theta, \varphi)d\varphi + \left(1 - V_f\right)\boldsymbol{I}\right]\boldsymbol{S}^m\overline{\boldsymbol{\sigma}}^m \qquad \textbf{Equation 3-77}$$

Eliminate the $\overline{\boldsymbol{\sigma}}^m$ from Equation 3-76 and Equation 3-77, the effective elastic modulus tensor for the composite with fiber waviness is calculated as:

$$\boldsymbol{C} = \frac{\left[\frac{V_f}{\varphi_l}\int_0^{\varphi_l} \boldsymbol{C}^f(\theta, \varphi)\boldsymbol{A}^{Eshelby}(\theta, \varphi)\boldsymbol{S}^m d\varphi + \left(1 - V_f\right)\boldsymbol{I}\right]}{\left[\frac{V_f}{\varphi_l}\int_0^{\varphi_l} \boldsymbol{A}^{Eshelby}(\theta, \varphi)d\varphi + \left(1 - V_f\right)\boldsymbol{I}\right]\boldsymbol{S}^m} \qquad \textbf{Equation 3-78}$$

The waviness amplitude calculated was introduced in Chapter 2 and input to the EL method in this Chapter.

The software MCQ (AlphaSTAR Corporation) is used to conduct convenient modeling and calculate in the simulation of equivalent laminate method in the present study with the algorithms and functions introduced above integrated.
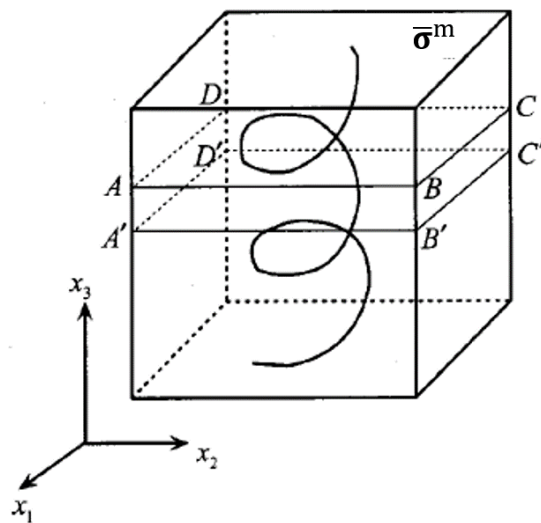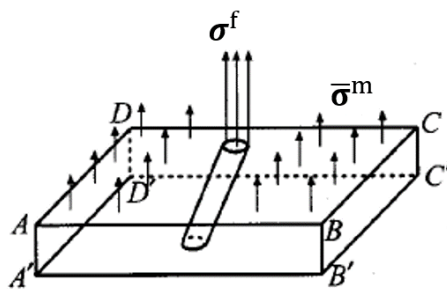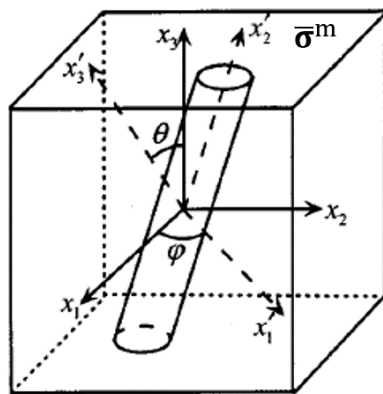
**Figure 3-8. Calculation model of the strain in a curved fiber: a curved fiber in the RVE (a); a slice of infinitesimal thickness (b); the approximate model for calculating the strain in the slice (c) [107].**

### 3.3.4. Structure and component evaluations

In the next step, the structure properties and component properties are also evaluated to collect the data necessary for accurate modeling in both MT method and EL method.

The values of $V_f$ for both the CMT and CTT were calculated using the "ash test". The ash test is used to determine the actual $V_f$ of composites by measuring the sample volume V using a densitometer and the weight of carbon fibers ($M_{CF}$) by burning the resin off. The following equation is used for the calculation:

$$V_f = \frac{M_{CF}/\rho_{CF}}{V}$$

**Equation 3-79**

where $\rho_{CF}$ is the density of the carbon fibers used in the material and is provided by the corresponding carbon fibers manufacturers.

On the other hand, the aspect ratios of the reinforcement of the CMT and CTT need to be determined because the mean-field homogenization in both MT method and EL method needs the aspect ratio of inclusions to conduct calculations. For CMT materials, because the reinforcements are randomly oriented carbon fiber monofilaments, the aspect ratio can be simply calculated using the following equation:

$$K_{CMT} = \frac{l}{d}$$

**Equation 3-80**

where $K_{CMT}$ is the aspect ratio of the reinforcement in CMT materials, $l$ is the fiber length, and $d$ is the fiber diameter. However, after the compression molding, brakeage is generally occurred in the carbon fiber monofilaments. Consequently, there is fiber length distribution inside the CMT material. In this study, the fiber length distributions were collected using a microscope to count the length of carbon fibers (Figure 3-9), and 1000 fibers were counted for both CMT-1 and CMT-2.
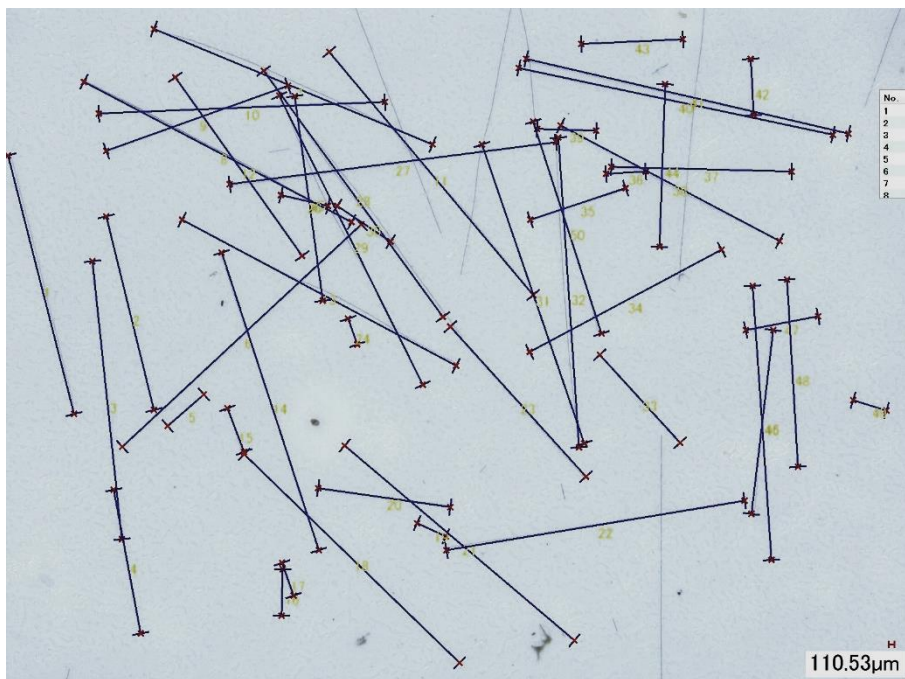
**Figure 3-9. Fiber lengths counting of CMT using microscope.**
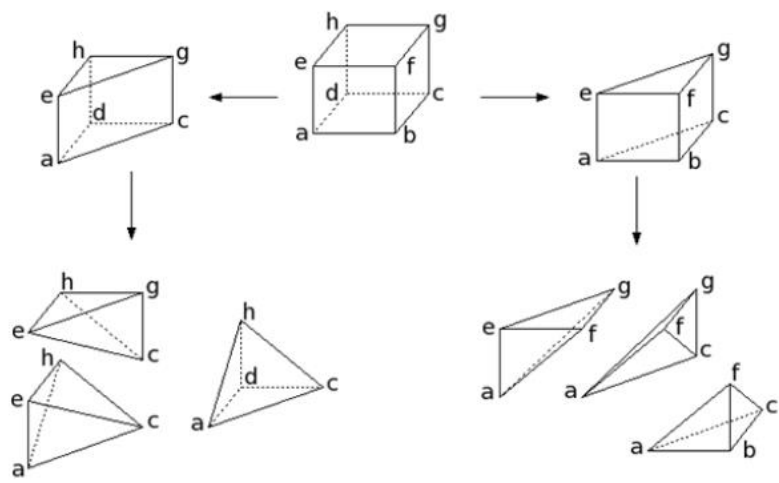


**Figure 3-10. A reference cubic 3D object (*abcdefgh*) and the possible contained tetrahedrons.**

Conversely, because the reinforcement in CTT is not fiber but prepreg tape, the definition of the aspect ratio will be different because interphases exist between the CF and resin as well as between each tape. In a preliminary structure study [108], we chose the tape as the basic inclusion and calculated the aspect ratio of the tape based on the definition of the 3D aspect ratio generally used in finite element methods [109] (Figure 3-10). Therefore, the equivalent tape aspect ratio is

calculated by the following equation:

$$K_{CTT} = \frac{h_{max}}{2\sqrt{6}r_{max}}$$

**Equation 3-81**

where $K_{CTT}$ is the equivalent aspect ratio of the reinforcement in CTT, $r_{max}$ is the largest inradius of the tetrahedrons contained in the tape structure, and $h_{max}$ is the largest edge length of the corresponding tetrahedron. Because the tape is cuboid, based on the general geometry theorems, $K_{CTT}$ is derived as (Figure 3-10):

$$K_{CTT} = \frac{h_{max} * S_{max}}{\sqrt{6}abc}$$

**Equation 3-82**

where S is the largest surface area of the tetrahedron, and a, b, and c are the tape length, width, and thickness, respectively. Consequently, by comparing the surface area of each tetrahedron in the cuboid tape, the aspect ratio of the tape structure in this study can be calculated as follows:

$$K_{CTT} = \sqrt{a^2 + b^2 + c^2} \left( ab + a\sqrt{b^2 + c^2} + b\sqrt{c^2 + a^2} \right.$$
$$\left. + \sqrt{a^2b^2 + b^2c^2 + c^2a^2} \right) \left( 2\sqrt{6}abc \right)^{-1}$$

**Equation 3-83**

Additionally, after the tensile experiments on the PP and PA6 matrix materials were conducted, the elastoplastic performance parameters needed for the simulations are calculated. As mentioned in the previous sub-section, the fracture strains of these resins are much higher (higher than 30%) than those of the CF (about 2%) and the composites (less than 2%), hence a maximum strain of the matrix materials of only 5% was recorded by the 25 mm extensometer to ensure measurement accuracy. The stress-strain curves of the matrices are fitted based on the $J_2$-plasticity model, which is given by [110]:

$$\sigma_{eq} = \begin{cases} \boldsymbol{C} : \varepsilon^e & J_2(\sigma) \leq \sigma_Y \\ \sigma_Y + kp + R_\infty[1 - e^{-mp}] & J_2(\sigma) > \sigma_Y \end{cases}$$

**Equation 3-84**

where $J_2(\sigma)$ is the von Mises equivalent stress, $\sigma_{eq}$ and $\sigma_Y$ denote the equivalent Cauchy stress and the yield stress, respectively, $\varepsilon^e$ is the elastic strain, $\boldsymbol{C}$ is Hooke's operator, and $k$, $R_\infty$, and $m$ denote the linear hardening modulus, hardening modulus, and hardening exponent, respectively. The parameter $p$ represents the accumulated plastic strain, and it is expressed as:

$$p(t) = \int_0^t \dot{p}(\tau)d\tau$$

**Equation 3-85**

with

$$\dot{p} = \left( \frac{2}{3}\dot{\varepsilon}^p : \dot{\varepsilon}^p \right)^{1/2}$$

**Equation 3-86**

The $J_2$-plasticity model curves were plotted using the experimental data, and the parameters used in the fitting $J_2$-plasticity curves were applied to the simulation processes of both MT method

and EL method.

## 3.4. Results and discussions

### 3.4.1. Experimental results

Tensile tests of CMT and CTT and the experimental evaluations of their material structures and components were conducted firstly in this chapter. The results are introduced and discussed in detail in this section.

3.4.1.1. Structure and component evaluations

The structures and components of CMT-1, CMT-2, CTT-12, CTT-18, CTT-24 and CTT-30 are evaluated in detail.

The average $V_f$ of all the materials are first measured using the ash test and the results are listed in Table 3-2. From the figure, we can find that the $V_f$ of CMT-1 and CMT-2 are close to the catalog value provided by the company (10% and 20 %, respectively). On the other hand, the $V_f$ of CTT in different tape lengths fall within the narrow range of 52% to 55% and are close to the average $V_f$ of the pre-impregnated sheets. And there is no apparent relationship between the $V_f$ and the tape length.

**Table 3-2. Fiber volume fraction ($V_f$) of CMT and CTT**

|  | CMT-1 | CMT-2 | CTT-12 | CTT-18 | CTT-24 | CTT-30 |
|---|---|---|---|---|---|---|
| $V_f$ (%) | 11.1 | 19.4 | 52.2 | 55.1 | 52.8 | 53.1 |

In the next step, the aspect ratios of CMT and CTT are measured and calculated. In CMT materials, as introduced in sub-section 3.3.4, due to the fiber breakage occurred during the compression molding process, the aspect ratio distributions are evaluated with 1000 samples. And the distributions were plotted in Figure 3-11. The results show the difference between the CMT samples for different values of $V_f$. When $V_f$ is higher, the probability of obtaining short fibers (with a relatively low aspect ratio) is increased. This is because, in order to ensure that the required impregnation condition is met, fiber breakage is more probable occured at higher $V_f$ values with denser fiber packing in the out-of-plane direction. High transverse compressive stress will occur

owing to the increase in molding pressure and fiber interaction during the molding processes.
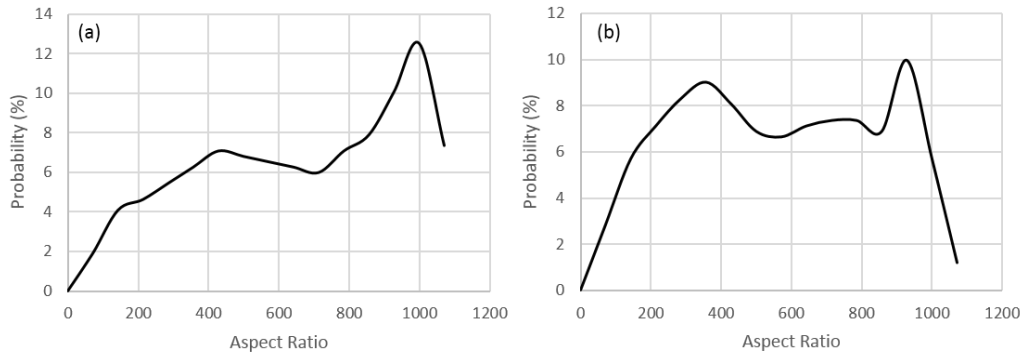


**Figure 3-11. Aspect ratio distribution of CMT-1 (a) and CMT-2 (b).**

On the other hand, the 3D aspect ratios of tapes were calculated as the equivalent aspect ratio of CTT. The relationship between the tape length and aspect ratio was plotted in Figure 3-12. From the figure, we can find that the equivalent aspect ratio and tape length have a linear relationship in long tape length and have slight concave down in the initial area. In conclusion, the aspect ratio of CMT and CTT are listed in Table 3-3.
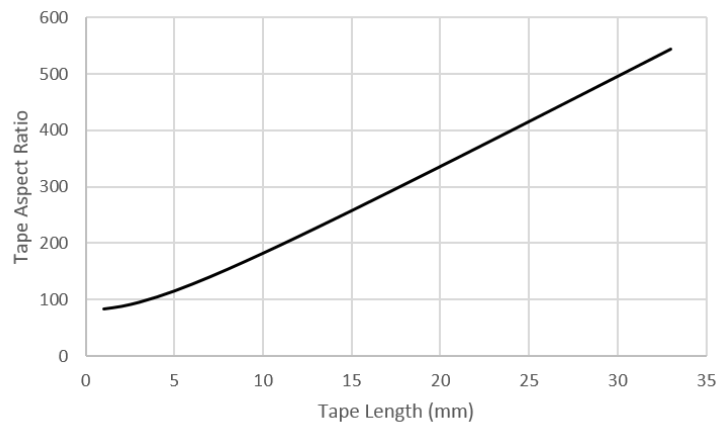


**Figure 3-12. Relationship between equivalent aspect ratio and tape length in CTT.**

**Table 3-3. Aspect ratio of inclusions in CMT and CTT.**

|                      | CMT-1 | CMT-2 | CTT-12 | CTT-18 | CTT-24 | CTT-30 |
|----------------------|-------|-------|--------|--------|--------|--------|
| Tape length (mm)     |   -   |       | 12     | 18     | 24     | 30     |
| Tape width (mm)      |   -   |       |        | 5      |        |        |
| Tape thickness (mm)  |   -   |       |        | 0.044  |        |        |
| Aspect ratio (K)     | Figure 3-11 |  | 212.3  | 305.1  | 400.0  | 496.7  |

After the structure properties were evaluated, the component properties of CMT and CTT were studied. Tensile tests of the matrix resins of CMT (PP) and CTT (PA6) were conducted and the stress-strain curves were collected. Fitting of the stress-strain curves of both PP and PA6 were done by the $J_2$-plasticity hardening model given by Equation 3-84 introduced before, and the fitting curves were illustrated in Figure 3-13. The parameters used in the $J_2$-plasticity hardening model to ensure the fitting condition of curves are listed in Table 3-4. The results show very good agreement between the experimental and calculated curves. And the equivalent matrix strengths $\sigma_{m\,PP}^*$ and $\sigma_{m\,PA6}^*$ were calculated based on the stress-strain curves as $\sigma_{m\,PP}^* = 26$ MPa and $\sigma_{m\,PA6}^* = 55$ MPa, which is the fracture strain of the corresponding carbon fibers embedded in the composites because the fracture of matrix itself is much higher than the fracture of composites [103].
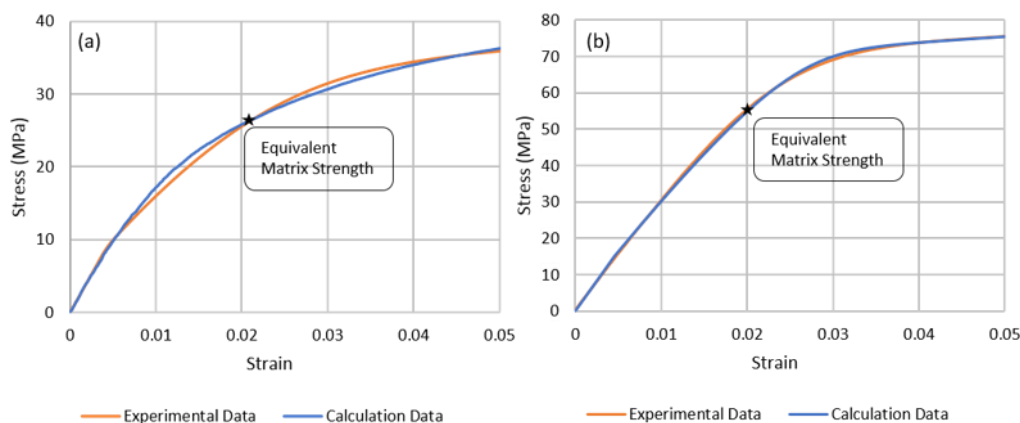


**Figure 3-13. Comparison of the experimental and calculation fitted stress-strain curves of matrices PP (a) and PA6 (b).**

**Table 3-4. Properties of polymer matrices.**

|  | PP | PA6 |
|---|---|---|
| Density (g/cm$^2$) | 0.90 | 1.14 |
| Poisson's Ratio $v$ | 0.35 | 0.40 |
| Young's Modulus $E$ (GPa) | 2.10 | 3.31 |
| Yield Stress $\sigma_Y$ (MPa) | 9.2 | 15.0 |
| Hardening Modulus $R_\infty$ (MPa) | 24 | 56 |
| Hardening Exponent $m$ | 135 | 350 |
| Linear Hardening Modulus $k$ (MPa) | 100 | 160 |
| Equivalent matrix tensile strength $\sigma_m^*$ (MPa) | 26 | 55 |

Moreover, the properties of the carbon fibers embedded in the CMT and CTT are listed in Table 3-5 collected from the catalog values of the corresponding manufacturers. The maximum stress based component failure indicators of the composites is defined as the component properties through the tensile direction due to the simple stress condition in the tensile tests as mentioned in Equation 3-44 and Equation 3-45, the tensile strengths data in Table 3-4 and Table 3-5 are inputted to the indicators in the simulations.

**Table 3-5. Properties of carbon fibers.**

|  | Young's Modulus $E$ (GPa) | Tensile Strength $\sigma$ (MPa) | Fracture Strain $\varepsilon_f$ (%) | Diameter $d$ (μm) | Density $\rho$ (g/cm$^2$) |
|---|---|---|---|---|---|
| CMT (T700) | 230 | 4900 | 2.1 | 7 | 1.80 |
| CTT (TR 50) | 240 | 4900 | 2.0 | 7 | 1.82 |

3.4.1.2.   Tensile experiments

Tensile experiments were conducted with five specimens in each kind of CMT and CTT. After the experiments, the stress-strain curves were collected to calculate the elastic moduli and tensile strengths. The fractographies of all the specimens were also analyzed.

Because the experimental mechanical properties are compared with the simulation results in detail

in the next sub-section, the fractographies are mainly studied in this sub-section.

Comparing the failure models, we found that there is no significant difference between the CMT-1 and CMT-2, which is the general result because the CMT is regarded as the traditional DCFRTP Figure 3-14. The fracture of CMT is generally the combination of fiber breakage together with the fiber debonding. These two fracture models occurred due to the random fiber dispersion in the composites, and no apparent resin rich or un-impregnated area was observed.
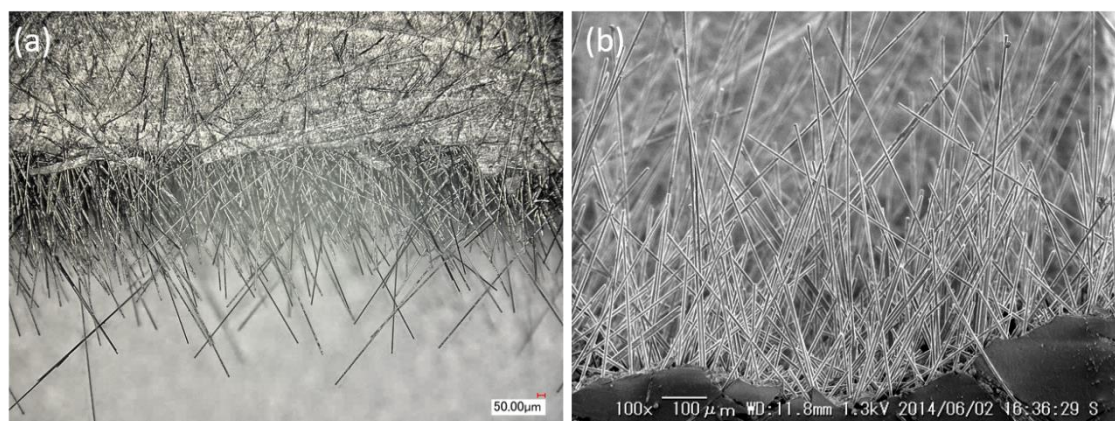


**Figure 3-14. Typical fractography of CMT using microscope (a) and SEM (b).**

On the other hand, the fracture of CTT exhibit some differences. Due to the complex multi-scale internal geometry of CTT, three basic failure models were observed during the tensile experiments: fiber breakage, tape splitting, and tape debonding (Figure 3-15). The tape splitting failure model is regarded as the debonding between the fibers and matrix in a tape structure, which can also be considered as the interphase debonding (between fiber phase and matrix phase). Similarly, the tape debonding is the resin-separation between individual tapes, so we can consider it as the interface debonding (between the surfaces of each tape).

Generally, these tensile failure models usually occur simultaneously in CTT composites. However, the occurrence frequencies of these failure models exhibit the molding condition dependency and tape morphology dependency revealed in a previous study [79]. With high molding pressure (5 MPa as the CTT used in this section and 10 MPa CTT introduced in Chapter 2), the fiber breakage becomes the dominant fracture model, the tape tearing could be observed in some parts, while the tape debonding was hardly detected in the composites. On the other hand, although the fiber breakage could be observed in the low molding pressure (3 MPa CTT introduced in Chapter 2), the interphase and interface debonding failures also played very important roles. Moreover, for

some 3 MPa CTT specimens characterized by poor mechanical performance, the interphase and interface debonding processes were considered to be the dominant failure models. In addition, the fiber breakage was more likely to occur in the specimens with longer tape length and less tape debonding can be observed. The tape length dependency of the tensile failure model is considered due to the randomly oriented tapes at the fracture cross section. Because with longer tape, the elongate tape boundary can prevent the fracture propagation in the failure progress, and if the tape boundary is longer enough, the failure model will shift from the interphase and interface debonding to fiber breakage to acquire lower fracture energy.

But it is still difficult to give a quantification on the tape length dependency of the failure models of CTT. Because in DCFRTP (especially ROS composites), the compression molding process still shows a significant effect on the failure model that the fabricating processes affect the tape morphology and emerge internal geometry defects even with the identical molding condition.

In the next sub-section, the internal geometry properties acquired in Chapter 2 are applied to the analytical models of CTT as well as CMT to compare the simulation results with experimental data and find out that if the consideration of internal geometry can increase the simulation accuracy on DCFRTP.
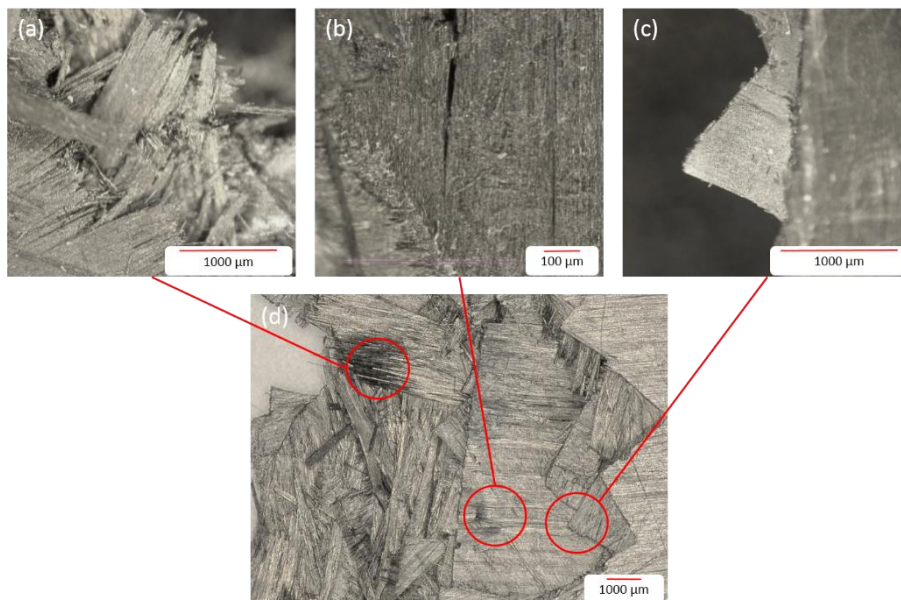


**Figure 3-15. Fiber breakage (a), tape splitting (interphase debonding) (b), and tape debonding (interface debonding) (c) [111] in the tensile specimen of CTT (d).**

### 3.4.2. Comparison with simulation results

The experimental data of the Young's modulus and tensile strength of CMT and CTT were characterized by the tensile tests. The simulation results calculated from the Mori-Tanaka method and Equivalent laminate method using the components and data on structural properties measured above were also collected. All these data were summarized and listed in Table 3-6 and illustrated in the histograms in Figure 3-16 and Figure 3-17.

**Table 3-6. Young's moduli and tensile strengths of CMT and CTT from experiments and simulations.**

|  |  | Experiment (5 samples) | Mori-Tanaka | Equivalent Laminate |
|---|---|---|---|---|
| Young's modulus (GPa) | CMT-1 | 9.7 | 10.5 | 10.8 |
|  | CMT-2 | 14.1 | 16.8 | 17.5 |
|  | CTT-12 | 42.5 | 46.6 | 48.9 |
|  | CTT-18 | 48.8 | 49.5 | 51.7 |
|  | CTT-24 | 45.6 | 47.5 | 49.4 |
|  | CTT-30 | 47.2 | 47.8 | 49.7 |
| Tensile strength (MPa) | CMT-1 | 157 | 176 | 156 |
|  | CMT-2 | 205 | 269 | 210 |
|  | CTT-12 | 436 | 494 | 479 |
|  | CTT-18 | 501 | 500 | 498 |
|  | CTT-24 | 480 | 498 | 499 |
|  | CTT-30 | 522 | 501 | 535 |
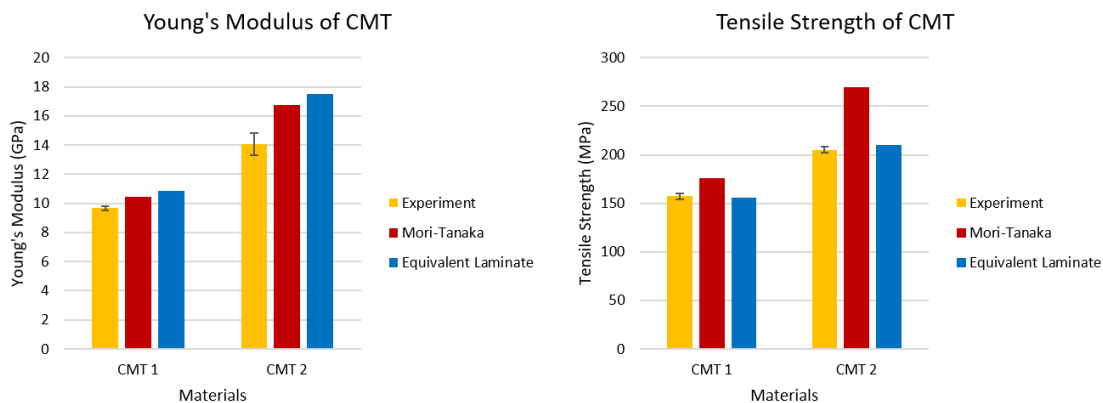
**Figure 3-16. Comparison of Young's moduli and tensile strengths of CMT from experiments and simulations.**
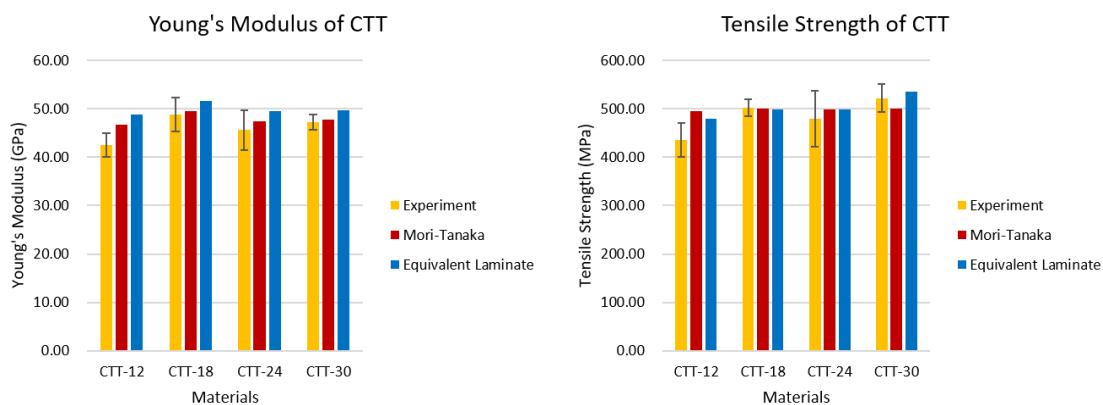


**Figure 3-17. Comparison of Young's moduli and tensile strengths of CTT from experiments and simulations.**

The experimental values of Young's modulus and tensile strength for CMT show very typical trends as the general type of DCFRTP, indicating that the modulus and strength both increase with an increase in $V_f$, but the mechanical properties are not proportional to the $V_f$ that CMT-2 are considered less efficient in the fiber reinforcement mechanism. In contrast, the CTT show outstanding mechanical properties, with high values for both modulus and strength compared with CMT and other DCFRTP with similar structures [82, 112, 113]. The tape length has an insignificant effect on the Young's modulus in UT-CTT, and the fluctuation is considered to be mainly due to the differences in the real $V_f$ (Table 3-2). The tensile strength, however, increases with an increase in tape length even though the tape length is much longer than the critical fiber

length for stress transmission [114]. This can be attributed to structural reinforcement in which tape overlap and tape boundary will decrease with the increase of tape length, and lead to an increase in the fracture propagation distance, thereby leading to a slight increase in strength (Figure 3-18)[79]. This assumption was also verified in Chapter 2, and the internal geometry data collected in Chapter 2 were applied in the MT method and EL method in this Chapter to reveal the relationship between tape length and mechanical properties of CTT in detail.
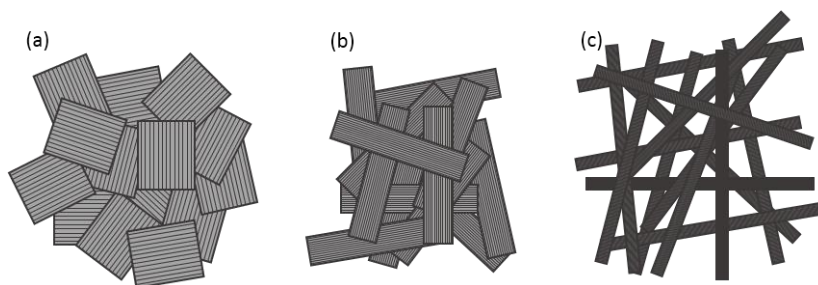


**Figure 3-18. Schematics of CTT-6 (a), CTT-24 (b), and imaginary CTT-120 (c).**

The results of stiffness simulations exhibit certain level of overestimation results in both MT method and EL method in CMT-1 and CMT-2. These higher simulation results increase with the increase in $V_f$ that average simulation results are 8% higher in CMT-1 and 20% in CMT-2 in MT method, and 11% higher in CMT-1 and 24% in CMT-2 in EL method. This result is considered general in the analytical simulation of traditional DCFRTP ([57, 76, 77]). The reason of these inaccuracy is considered due to effects from the complex internal geometries and internal defects. It is also clear that the EL method generated higher overestimation results compare with the MT method.

On the other hand, the stiffness simulations show very good agreement in both MT method and EL method with the experimental values for CTT at all tape lengths. Analogy to the results of CMT, an average of 4% difference is generated from the simulation data to experimental values in MT method; and an average difference of 9% is generated in EL method. The difference between both the MT method and EL method results show neglectable Young's moduli values compare with the experimental data. In addition, although the results from MT method and EL method just generated small overestimate on the Young's modulus of CTT, but there is still the similar overestimation tendency with the simulation of CMT.

Comparison of the strength data shows some difference in the results of MT method and EL method. In CMT, the tensile strengths in MT simulation are much higher than the experimental

data (13% higher in CMT-1 and 31% in CMT-2), while the EL method generated considerable fitting in tensile strengths of CMT in both $V_f$ (1% lower in CMT-1 and 2% higher in CMT-2). But combined with the Young's moduli simulation results, the good match in tensile strengths come out with a highly underestimate fracture strain in EL method. In CTT, the average values show good agreement (average of 5% difference) with the experimental results at all tape lengths in MT simulation results, but the MT method only shows a negligible increase in strength with the increase in tape length. Conversely, although the tensile strength of CTT-12 is a little higher than experimental data in EL simulation, the general trend and values exhibit considerable matching with the experimental results (average of 4% difference) with the similar increase in strength with the increase in tape length Figure 3-17.

These comparisons between the experimental results and the Mori-Tanaka model simulation revealed different trends [76, 77]. In previous studies, the Mori-Tanaka model was shown to be accurate when the volume fraction, $V_f$, of the reinforcement is less than 20% and the aspect ratio is less than 100. When these parameters are increased, the simulation results in inaccurate estimations. In this study, for CMT, the simulation did not yield accurate estimations when the aspect ratio ranged from 0 to 1000 and $V_f$ was lower than 20%, which is in accordance with the previous results. However, for CTT, the simulation gave accurate estimations of the tensile properties when the equivalent aspect ratio ranged from 200 to 500 and $V_f$ was higher than 50%. This result indicates the feasibility of the Mori-Tanaka model in simulations for CTT, which have high $V_f$ values and high aspect ratios.

The experimental and MT simulation stress-strain curves are shown in Figure 3-19 for CMT samples. The stress-strain curves were measured and simulated up to the failure point. The main difference between the experimental curves and MT simulation curves is that the experimental curves are concave-down at higher stresses, and the simulated curves remain linear until fracture occurs. This phenomenon indicates that in the experiments, plastic progression occurred before the fracture, while the mean-field homogenization method cannot reproduce this composite behavior. The strain at fracture point from the experimental results also show slight decrease with the increase of $V_f$.

On the other hand, the experimental and MT simulation stress-strain curves of CTT samples exhibit different results (Figure 3-20). Both the simulated and experimental curves for CTT with different tape lengths generally show good linearity and slope. Also the strain at fracture points (1.2 in average) are lower than that of CMT (1.8 in average). The simulation curves reached the similar failure point with the experimental samples, which is analogy with the moduli and

strengths comparison discussed above. While subtle increase and concentration of the linearity (stiffness at high level stress) were also observed with the increase of tape length that slight curves' concave-down were found in the experimental curves of CTT-12 samples.

The difference between the comparison of experimental and simulation stress-strain curves in CMT and CTT indicated the difference in material features. As studied in detail in Chapter 2, the internal geometry of CTT have much better structural regularity compare with the ROS fabricated with bulking molding process and traditional DCFRTP like CMT. This structural regularity of internal geometry can help decrease the internal defects of the composites therefore increase the energy required for reaching the failure of material. The high mechanical properties and stress-strain curves' linearity from tensile experiments of CTT verified this consideration. Moreover, the high linearity of stress-strain curves also indicate that CTT can be well described by the shear-lag theory of Cox [48] and the yielding and slip theory of Kelly and co-workers [103, 115] based on their theory definitions.
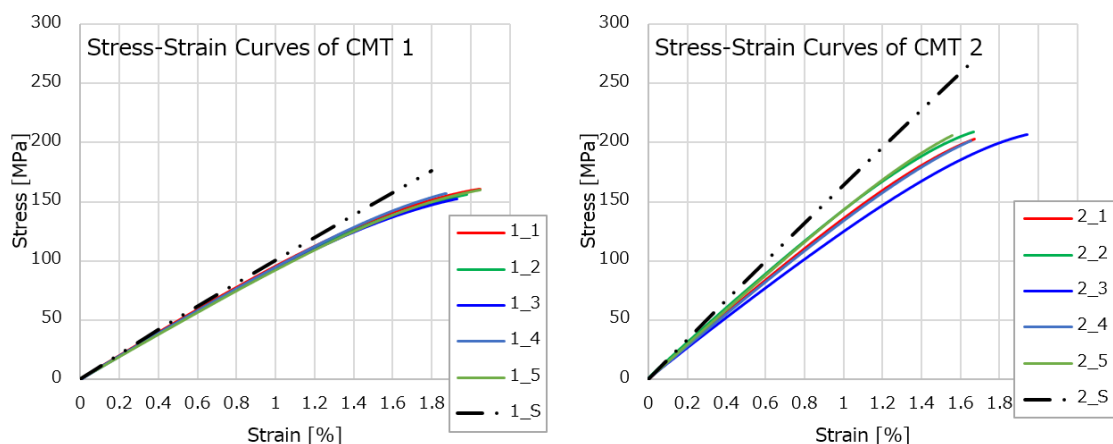


**Figure 3-19. Comparison of stress-strain curves of CMT from experiments and Mori-Tanaka simulations.**
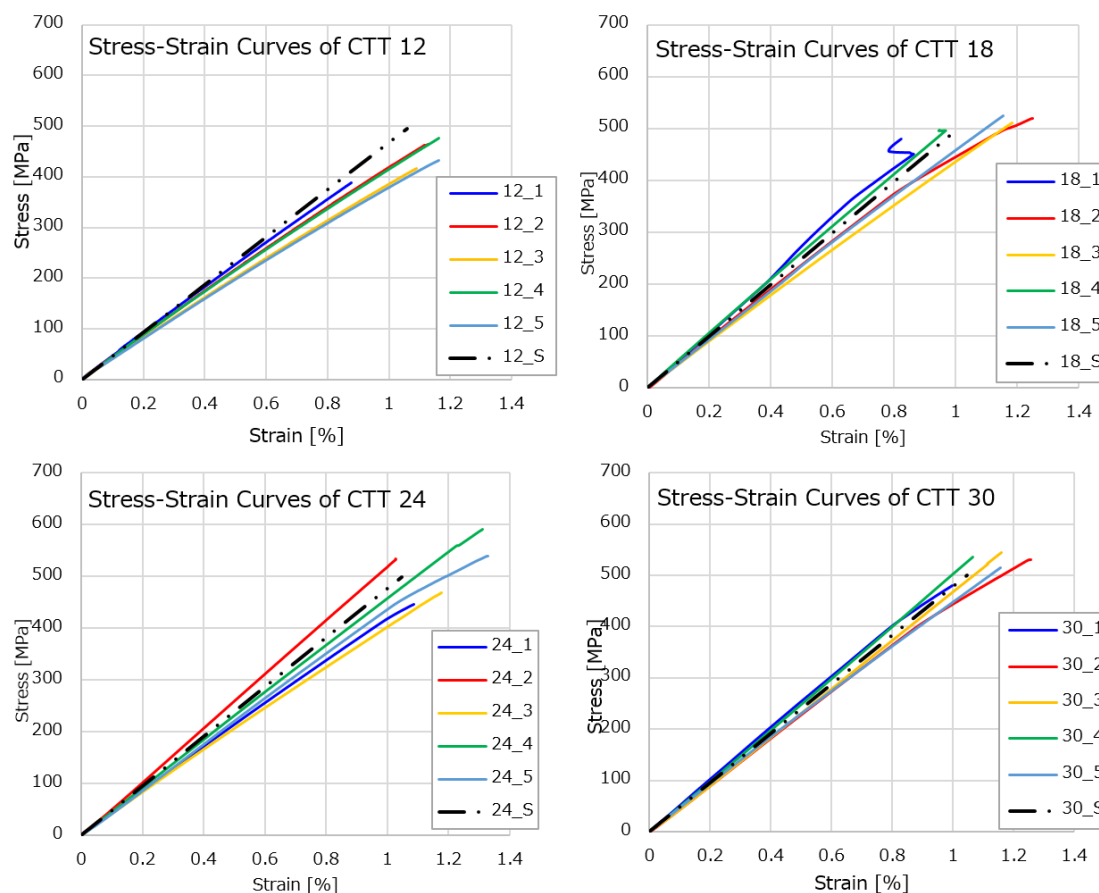
**Figure 3-20. Comparison of stress-strain curves of CTT from experiments and Mori-Tanaka simulations.**

In addition, using the CLT for equivalent laminate simulation in EL method can not only provide the required mechanical properties of CTT but also useful information with the equivalent laminates. The progressive failure can give clear results concerning the failure models and their progressive conditions in each specific layer of the equivalent laminate. Figure 3-21 illustrated the progressive failure condition of the laminate generated to equivalent with CTT-12. The figure indicated that the longitudinal tensile failure and transverse failure are the dominate failure models in the present tensile simulation. The relationship between the equivalent laminate positions and the failure models is regarded to be influenced by the equivalent laminate stacking sequence. Although in the present study, only the simple tensile stress condition was applied, but in further researches, this equivalent progressive failure charts can provide categorical failure models of the equivalent laminates, and hence corresponding failure models CTT worthy for reference. Furthermore, the laminate stacking sequence of the equivalent laminate can be generated in EL

117

method, too (Figure 3-22). This laminate stacking sequences open the way for experimental verification of the reliability and repeatability of EL method (of which the laminate-equivalent assumption is considered lack of theoretical basis by some researchers) and is also undergoing in author's extending works.
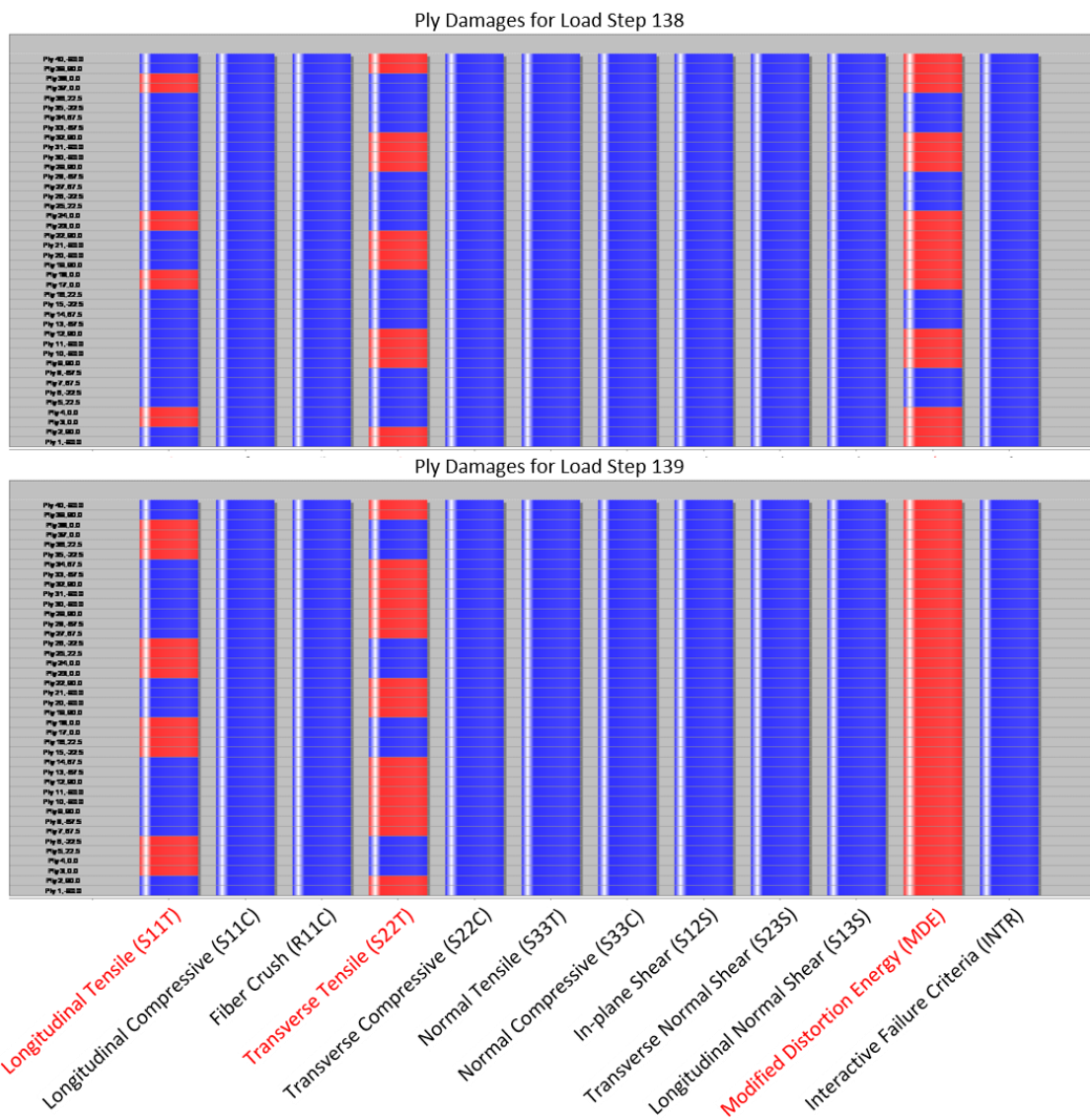


**Figure 3-21. Equivalent progressive failure of CTT-12 from equivalent laminate simulations.**
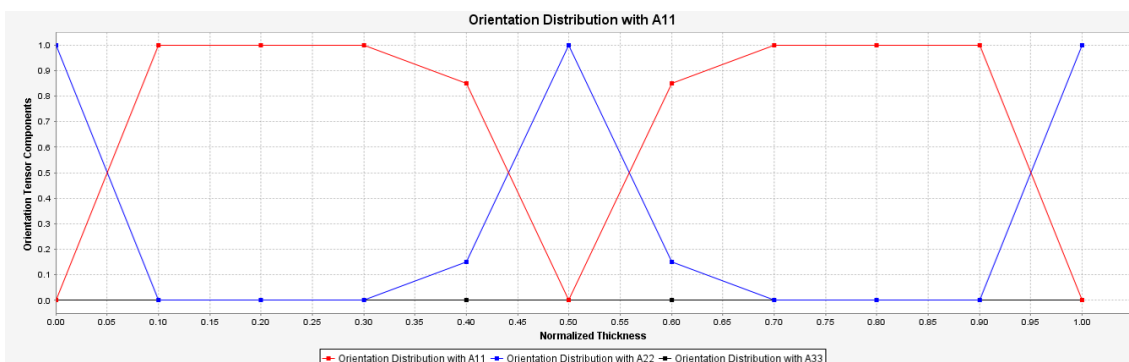
**Figure 3-22. Equivalent laminate sequence of CTT-12 from equivalent laminate simulations.**

Because both the MT method and the EL method yielded considerable agreements with the experimental results for CTT, we decided to use these two methods to predict the tape length dependency of CTT on Young's modulus and tensile strength. To simplify the calculation, the tapes in CTT are considered 2D (in-plane) randomly oriented with 5° waviness in EL method. The $V_f$ is fixed to 50% and the tape thickness is set to 50 μm together with 5 mm tape width. The tape length dependency of Young's modulus and tensile strength results are illustrated in Figure 3-23. In general, both the MT method and EL method reproduced the relationship between the tape length and the tensile properties in certain level. There are steeply initial increase of both the Young's modulus and tensile strength with the increase of tape length, and eventually reaching a plateau at higher tape lengths. Similar with the comparison simulation results, the tensile strength from EL simulation exhibit more apparent tape length dependency, and the higher value of tensile strengths from MT results imply greater overestimate and less tape length sensitivity of the tensile strength of CTT. On the other hand, the simulations of Young's moduli exhibit converse results. The Young's moduli calculated by EL method are higher than MT results in all the range, also the MT method exhibit better tape length sensitivity on Young's moduli compare with EL method (which also indicate the moduli change in EL results in Figure 3-17 is generated by the change of $V_f$) that more significant increase were observed in MT simulation results.
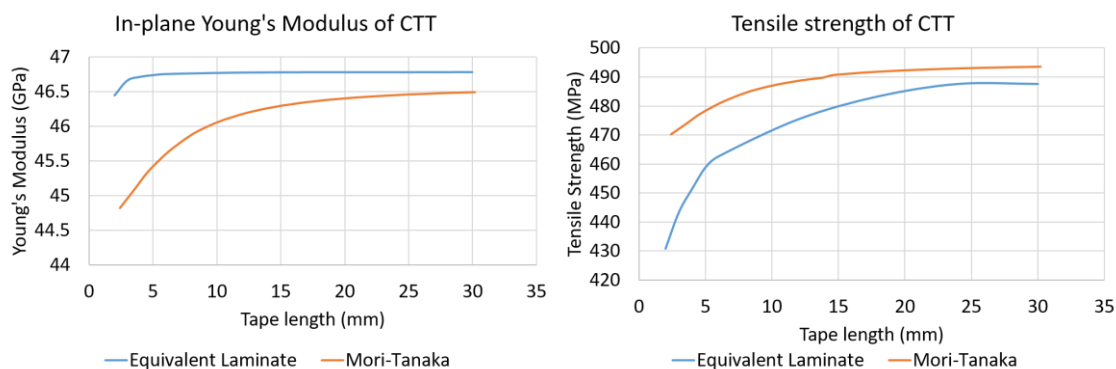
**Figure 3-23. Tape length dependency of Young's modulus and tensile strength simulated by MT method and EL method. With fixed 2D randomly oriented (5° waviness in EL method), 50% $V_f$, 50 μm tape thickness and 5 mm tape width.**

These simulation difference between the MT method and EL method is considered to be influenced by their modeling definitions, which means that the equivalent continuous-system assumption overestimating the moduli of discontinuous systems compare with MT homogenization even if the internal defects like out-of-plane waviness is considered during the modeling processes. But in contrast, the internal defect consideration combined with the equivalent laminate theory can provide better accuracy on the aspect ratio dependency of tensile strength compared with the general mean-filed homogenizations. Comparing together with the experimental results, additional defects-definition factors should be considered carefully to achieve more accurate simulations.

Furthermore, the simulation results provided a possible approach for industries to decide the optimal tape length of one kind of ROS for application as a compromise between the manufacturing considerations and mechanical properties based on the simulation results (MT method and EL method) together with the fabricating method selected for the manufacturing (SM process or BM process). Which regarded the methods introduced in the present study as a preliminary assessment of the suitability of DCFRTPs for industrial applications.

## 3.5. Conclusions

In this chapter, the tensile properties of CMT and CTT were characterized both experimentally and analytically. Two different analytical modeling methods, Mori-Tanaka method and Equivalent Laminate method, were conducted together with the comparison tensile tests not only to obtain the mechanical properties of the two DCFRTP but also verify the capability and accuracy of the simulation models. The MT method is one of the most general mean-field homogenization micromechanics methods for DCFRTP, using the Eshelby's equivalent theory to simplify the complex fiber inclusion problem. The EL method is a kind of new approach developed in recent years for mechanical property prediction of DCFRTP (especially for ROS-structured composites), which defines the mechanical property of each layer using developed micromechanics and applies classical laminate theory on the corresponding equivalent laminate to simulate the DCFRTP properties while avoiding detail modeling on the sophisticated internal geometries. Both the MT method and EL method show advantages on accuracy and efficiency on DCFRTP simulation in different aspects and this chapter provided a comprehensive comparison between this two method on the simulation of tensile properties of CMT and CTT with different components and fabrication processes.

The tensile tests revealed the difference between the traditional DCFRTP (CMT) with the ROS (CTT). The CTT exhibit considerable tensile moduli and strength compared with CMT. Higher moduli with lower fracture strain were observed in CTT while the CMT show typical properties of DCFRTP. The outstanding mechanical properties of CTT indicated the potential of industrial applications.

To ensure the accuracy of simulation modeling, the internal geometry properties obtained from X-ray micro-CT analysis together with structure and component properties were evaluated in detail and input to both the MT method and EL method. The orientation tensors calculated from 3D-BON were input to MT method and the out-of-plane waviness collected from VoxTex were imported to EL method. Aspect ratio distributions of CMT and 3D equivalent aspect ratios of tape in CTT were defined and evaluated respectively. The non-linear properties of matrix resins were characterized experimentally.

The experiments and the simulations of CMT demonstrated similar results with the previous reports that homogenization micromechanics results in inaccurate estimations of the mechanical properties of DCFRTP. While in CTT, considerable improvements were achieved in both the general MT method and the EL method.

The MT method and EL method show different advantages on the simulation results. In tensile moduli of CTT, the MT method provided results with good accuracy while the EL model results in slight overestimating. In the tensile strength, although the average values of both simulations were good, but the EL method demonstrated considerable tape length dependency on the results while the MT method cannot reproduce the tape length effect. The mechanisms of the results of both methods were discussed in detail and the simplification processes during the modeling are considered to be the main reason caused these simulation results. Moreover, employing additional specific defects-definition factors is considered a feasible and efficient way to increase the simulation accuracy of both MT method and EL method.

The simulation methods also provided an approach to deciding the optimal strand aspect ratio of ROS for industrial applications with the comprehensive consideration of mechanical simulation results with manufacturing conditions.

# **Note**

The contents of this Chapter are partially based on the following corresponding publications in the "**List of publications and awards**" listed at the end of this thesis:

(1) Journal Papers

〔Peer-reviewed〕

(1-3)　　**Yi Wan** and Jun Takahashi, 'Tensile and compressive properties of chopped carbon fiber tapes reinforced thermoplastics with different fiber lengths and molding pressures', Composites Part a-Applied Science and Manufacturing. 2016, Vol. 87, 271-281.

(1-5)　　**Yi Wan** and Jun Takahashi, 'Tensile properties and aspect ratio simulation of transversely isotropic discontinuous carbon fiber reinforced thermoplastics', Composites sciences and technology. 2016, Vol. 137, 167-176.

〔Peer-reviewed　Under review *Italic under preparation*〕

*(1-12)　**Yi Wan** and Jun Takahashi,　'Mean filed homogenization and de-homogenization methods for predicting tensile properties of randomly oriented strands', Composites sciences and technology.*

(2) International Conference Proceeding：

〔peer-reviewed　○: Presenter〕

(2-5)　　○ **Yi Wan** and Jun Takahashi, 'Fiber length effect on tensile and compressive strength of short fiber reinforced thermoplastics', the 16th European conference on composite materials (ECCM16), 25.1.1-R11, Seville, Spain, (June 2014).

(2-7)　　○ **Yi Wan** and Jun Takahashi, 'Effect of tape length and impregnation conditions on mechanical properties of carbon fiber tape reinforced thermoplastics', the 12th International Conference on Textile Composites (TEXCOMP-12), Poster 4, Raleigh, NC, U.S.A., (May 2015).

(2-8)　　○ **Yi Wan** and Jun Takahashi, 'Bending and impact properties of randomly orientated discontinuous carbon fiber reinforced thermoplastics with thin-ply structure', the 23rd Annual International Conference on Composites/NANO Engineering (ICCE-23), pp. 743-744, Chengdu, China, (July 2015).

(2-10)　○ **Yi Wan**, Toshiro Ohori and Jun Takahashi, 'Mechanical properties and modeling of discontinuous carbon fiber reinforced thermoplastics', the 20th International Conference on Composite Materials (ICCM20), 3222-4, Copenhagen, Denmark, (July 2015).

(2-11)　○ <u>ワンイー</u>, 髙橋淳, '森・田中理論を用いた CTT 材の最適テープ長決定方法', 日本複合材料学会第４０回複合材料シンポジウム, B1-09, 金沢, (2015 年 9 月).

(2-15)　○ **<u>Yi Wan</u>** and Jun Takahashi, 'CFRTP mechanical properties simulation by Mori-Tanaka model and equivalent laminate methods', the 17th European Conference on Composite Materials (ECCM17), TUE-4_BIA_3.09-02, Munich, Germany, (June 2016).

(2-19)　○ **<u>Yi Wan</u>** and Jun Takahashi, 'Modeling analysis and evaluation of tensile properties of discontinuous CFRTP using homogenization and de-homogenization methods', 2016 SAMPE International Education Program, The composites and advanced materials EXPO (CAMX), Anaheim, California, (September 2016).

〔peer-reviewed　○: Presenter　Accepted〕

(2-22)　○ **<u>Yi Wan</u>** and Jun Takahashi, 'Multi-scale internal geometry analysis and mechanical modeling of randomly oriented strands', the 21st International Conference on Composite Materials (ICCM21), Xi'an, China, (August 2017).

(2-26)　○ **<u>Yi Wan</u>** and Jun Takahashi, 'Internal geometry analysis and mechanical property simulation of randomly oriented strands', the 15th European-Japanese Meeting on Composite Materials, London, UK, (September 2017).

<div align="right">

# Chapter 4.   Conclusions

</div>

This thesis discusses the internal geometries and mechanical properties of discontinuous carbon fiber reinforced thermoplastics. The two main subjects, internal geometry analyses (Chapter 2) and mechanical property characterizations (Chapter 3) are respectively summarized in terms of outputs. Finally, future prospects of discontinuous carbon fiber reinforced thermoplastics on both material research aspect and industrial application aspect are presented.

## 4.1.  General conclusions

The internal geometry analyses provide comprehensive quantifications and visualizations of CMT and CTT using two X-ray micro-CT methods, the VoxTex and TRI/3D-BON. The algorithm of image processing in VoxTex method based on the "voxel model" combined with structure tensor calculation, and in 3D-BON method based on the general image binarization. The internal geometries of CMT and CTT with different components and fabrication processes were evaluated in detail. The significance of X-ray micro-CT analysis, which is generally regarded as the crucial problem of DCFRTP, is being proved for the first time using a statistical mulit-sample method in this study. The number for reliable X-ray micro-CT analysis has been decided. The VoxTex

method and 3D-BON method showed different advantages on the quantification and visualization of internal geometries of CMT and CTT. The "voxel model" based VOI definition and unfolded orientation histograms in VoxTex method bring an efficient approach for the analysis of layered properties in CTT. The effects of compression molding conditions, tape lengths and tape thicknesses on internal geometries of CTT were verified in detail. The micro structures were quantified and 3D models with visualized orientation distributions were generated. It was found that higher molding pressure can decrease the structure regularity due to the tape splitting, and the tape length exhibits positive effect on increase the layer independence through thickness direction. The out-of-plane waviness was defined as the structural defect and calculated using VoxTex data. The comparison between the out-of-plane waviness and the tensile properties of corresponding CTT with different tape thicknesses show considerable linearity, which was applied in the modeling and simulations. The monofilament-separated image binarization process in 3D-BON method provided more detailed scale structural 3D models with visualized orientation distributions, and this method is considered more suitable for traditional DCFRTP like CMT. The averaged orientation tensors can be calculated using 3D-BON with the fiber level detailed data. As the representative orientation property, the orientation tensors are also applied for the modeling and simulation. The out-of-plane vector $v_{33}$ also show good agreement with the tensile properties in CTT with different thickness.

The tensile properties of CMT and CTT were characterized both experimentally and analytically with two different analytical modeling methods, the Mori-Tanaka method and the Equivalent Laminate method. The MT method is the general mean-field homogenization micromechanics method for DCFRTP and the EL method is a new approach combining classical laminate theory with the micromechanics developed in recent years for mechanical property prediction of DCFRTP (especially for ROS-structured composites). Both the MT method and EL method show advantages on accuracy and efficiency of DCFRTP simulation in different aspects and comprehensive comparison between this two method on the simulation of tensile properties of two kinds of CMT and CTT with different components and fabrication processes were conducted. The CTT exhibit higher Young's moduli with lower tensile fracture strain compare with CMT. The outstanding mechanical properties indicated the potential of industrial application of CTT. The orientation tensors calculated from 3D-BON were input to MT method and the out-of-plane waviness collected from VoxTex were imported to EL method. Aspect ratio distributions of CMT and 3D equivalent aspect ratios of tape in CTT were defined and evaluated respectively. The non-linear properties of matrix resins were characterized experimentally. The experiments and the simulations of CMT demonstrated similar results with the previous reports that homogenization micromechanics results in inaccurate estimations of the mechanical properties of DCFRTP. In

CTT, considerable improvements were achieved in both the general MT method and the EL method, which indicated that the CTT have good CAE capability. In tensile moduli of CTT, the MT method provided results with good accuracy while the EL model results in slight overestimating. In the tensile strength, although the average values of both simulations were good, but the EL method demonstrated considerable tape length dependency on the results while the MT method cannot reproduce the tape length effect. The simplification processes during the modeling are considered to be the reason caused these simulation results. The optimal strand aspect ratio of ROS for industrial applications can be decided by the simulation methods based on the comprehensive consideration of mechanical simulation results with manufacturing conditions.

## 4.2. Material research aspect

The VoxTex method is a novel method developed in this thesis for the purpose of detailed internal geometry analysis of ROS-structured composites. The VOI definition and the unfolded histograms applied in this method provide efficient multi-scale internal geometries analysis of CTT and show huge potential on the X-ray micro-CT study of ROS composites. The relationship between the internal geometries, material parameters (inclusions shapes, molding conditions) and mechanical properties of CTT revealed using X-ray micro-CT at the first time. The analytical simulation modeling combined with the X-ray micro-CT results open the new way for accurate prediction of mechanical properties. The simulations by MT method and EL method show different advantages on the simulation and the methods can be selected based on the research purposes, targets and method capabilities. By employing additional specific defects-definition factors, the simulation accuracy of both MT method and EL method is considered to further increase. With the combination of the two X-ray micro-CT methods with the two analytical simulation methods, comprehensive methodologies are generated to provide feasible solutions for DCFRTP characterization.

## 4.3. Industrial application aspect

The two X-ray micro-CT methods provided feasible and efficient approaches for evaluating the internal geometry of DCFRTP. As non-destructive inspections, these X-ray micro-CT methods can help engineers to verify and locate the internal defects caused during the fabricating effectively and further provide the solutions to avoid them. The two analytical simulation methods

introduced in this thesis have considerable calculation efficiency and simulation accuracy. Combined with the X-ray micro-CT detections, the comprehensive material characterization solutions can be given for the purpose of mass-production applications. The different advantages of both the X-ray micro-CT methods and analytical simulation methods offer multiple choices for engineers to characterize DCFRTP under the consideration of method capabilities and application objectives. Moreover, the analyses of internal geometries and mechanical properties in this thesis can show the way to improve the performance and extend the potential of the corresponding DCFRTP.

# Acknowledgments

# References

[1]     Jun Takahashi. Expectations and challenge of thermoplastic CFRP.   SAMPE Japan symposium "Future of automobile pioneered by advanced materials". Tokyo, Japan. 2016.

[2]     J. Takahashi, T. Ishikawa. Next challenge in CFRTP for mass production automotive application.   SEICO 14 SAMPE EUROPE 35th International Conference and Forum. Paris, France2014.

[3]     A. Bernasconi, F. Cosmi, P. J. Hine. Analysis of fibre orientation distribution in short fibre reinforced polymers: A comparison between optical and tomographic methods. Composites Science and Technology. 2012;72(16):2002-2008.

[4]     S. Fakirov, C. Fakirova. Direct determination of the orientation of short glass fibers in an injection-molded poly(ethylene terephthalate) system. Polymer Composites. 1985;6(1):41-46.

[5]     W. E. Roseveare. Contributions to the physics of cellulose fibres. P. H. HERMANS. Elsevier, New York-Amsterdam, 1946. In English. 221 pp. Journal of Polymer Science. 1947;2(3):354-354.

[6]     B. Möginger, P. Eyerer. Determination of the weighting function g(βi,r,vf) for fibre orientation analysis of short fibre-reinforced composites. Composites. 1991;22(5):394-399.

[7]     Günther Fischer, Peter Eyerer. Measuring spatial orientation of short fiber reinforced thermoplastics by image analysis. Polymer Composites. 1988;9(4):297-304.

[8]     R. S. Bay, C. L. Tucker. STEREOLOGICAL MEASUREMENT AND ERROR-ESTIMATES FOR 3-DIMENSIONAL FIBER ORIENTATION. Polymer Engineering and Science. 1992;32(4):240-253.

[9]     N. C. Davidson, A. R. Clarke, G. Archenhold. Large-area, high-resolution image analysis of composite materials. Journal Of Microscopy-Oxford. 1997;185:233-242.

[10]    G. Zak, C. B. Park, B. Benhabib. Estimation of three-dimensional fibre-orientation distribution in short-fibre composites by a two-section method. Journal of Composite Materials. 2001;35(4):316-339.

[11]    A. Clarke, N. Davidson, G. Archenhold. MEASUREMENTS OF FIBER DIRECTION IN REINFORCED POLYMER COMPOSITES. Journal Of Microscopy-Oxford. 1993;171:69-79.

[12]    A. R. Clarke, G. Archenhold, N. C. Davidson. A NOVEL TECHNIQUE FOR DETERMINING THE 3D SPATIAL-DISTRIBUTION OF GLASS-FIBERS IN

POLYMER COMPOSITES. Composites Science and Technology. 1995;55(1):75-91.

[13]    C. Eberhardt, A. Clarke. Fibre-orientation measurements in short-glass-fibre composites. Part I: automated, high-angular-resolution measurement by confocal microscopy. Composites Science and Technology. 2001;61(10):1389-1400.

[14]    P. J. Hine, N. Davidson, R. A. Duckett, I. M. Ward. MEASURING THE FIBER ORIENTATION AND MODELING THE ELASTIC PROPERTIES OF INJECTION-MOLDED LONG-GLASS-FIBER-REINFORCED NYLON. Composites Science and Technology. 1995;53(2):125-131.

[15]    S. Kleindel, D. Salaberger, R. Eder, H. Schretter, C. Hochenauer. Prediction and Validation of Short Fiber Orientation in a Complex Injection Molded Part with Chunky Geometry. International Polymer Processing. 2015;30(3):366-380.

[16]    U. Gandhi, D. Sebastian, V. Kunc, Y. Y. Song. Method to measure orientation of discontinuous fiber embedded in the polymer matrix from computerized tomography scan data. Journal of Thermoplastic Composite Materials. 2016;29(12):1696-1709.

[17]    E. G. Kim, J. K. Park, S. H. Jo. A study on fiber orientation during the injection molding of fiber-reinforced polymeric composites (Comparison between image processing results and numerical simulation). Journal of Materials Processing Technology. 2001;111(1-3):225-232.

[18]    Takahiro Hayashi, Takayuki Kobayashi, Jun Takahashi. Quantification of the void content of composite materials using soft X-ray transmittance. Journal of Thermoplastic Composite Materials.0(0):0892705716644670.

[19]    Yi Wan, Ilya Straumit, Jun Takahashi, Stepan V. Lomov. Micro-CT analysis of internal geometry of chopped carbon fiber tapes reinforced thermoplastics. Composites Part A: Applied Science and Manufacturing. 2016;91, Part 1:211-221.

[20]    H. B. Shen, S. Nutt, D. Hull. Direct observation and measurement of fiber architecture in short fiber-polymer composite foam through micro-CT imaging. Composites Science and Technology. 2004;64(13-14):2113-2120.

[21]    A. Bernasconi, F. Cosmi, D. Dreossi. Local anisotropy analysis of injection moulded fibre reinforced polymer composites. Composites Science and Technology. 2008;68(12):2574-2581.

[22]    F. Cosmi, A. Bernasconi, N. Sodini. Phase contrast micro-tomography and morphological analysis of a short carbon fibre reinforced polyamide. Composites Science and Technology. 2011;71(1):23-30.

[23]    Ilya Straumit, Stepan V. Lomov, Martine Wevers. Quantification of the internal structure and automatic generation of voxel models of textile composites from X-ray computed tomography data. Composites Part A: Applied Science and Manufacturing.

2015;69:150-158.

[24]    M. Barburski, I. Straumit, X. W. Zhang, M. Weyers, S. V. Lomov. Micro-CT analysis of internal structure of sheared textile composite reinforcement. Composites Part a-Applied Science and Manufacturing. 2015;73:45-54.

[25]    S.C. Cowin, S.B. Doty. Tissue mechanics: Springer; 2007.

[26]    G. M. Luo, A. M. Sadegh, S. C. Cowin. The mean intercept length polygons for systems of planar nets. Journal of Materials Science. 1991;26(9):2389-2396.

[27]    A. Alemdar, H. Zhang, M. Sain, G. Cescutti, J. Mussig. Determination of fiber size distributions of injection moulded polypropylene/natural fibers using X-ray microtomography. Advanced Engineering Materials. 2008;10(1-2):126-130.

[28]    Y. Abdin, S. V. Lomov, A. Jain, G. H. Van Lenthe, I. Verpoest. Geometrical characterization and micro-structural modeling of short steel fiber composites. Composites Part a-Applied Science and Manufacturing. 2014;67:171-180.

[29]    Thanh Binh Nguyen Thi, Mizuki Morioka, Atsushi Yokoyama, Senji Hamanaka, Katsuhisa Yamashita, Chisato Nonomura. Measurement of fiber orientation distribution in injection-molded short-glass-fiber composites using X-ray computed tomography. Journal of Materials Processing Technology. 2015;219:1-9.

[30]    Xianjun Sun, John Lasecki, Danielle Zeng, Yuan Gan, Xuming Su, Jie Tao. Measurement and quantitative analysis of fiber orientation distribution in long fiber reinforced part by injection molding. Polymer Testing. 2015;42:168-174.

[31]    Guillermo Requena, Georg Fiedler, Bernhard Seiser, Peter Degischer, Marco Di Michiel, Thomas Buslaps. 3D-Quantification of the distribution of continuous fibres in unidirectionally reinforced composites. Composites Part A: Applied Science and Manufacturing. 2009;40(2):152-163.

[32]    S. Dietrich, J. M. Gebert, G. Stasiuk, A. Wanner, K. A. Weidenmann, O. Deutschmann, I. Tsukrov, R. Piat. Microstructure characterization of CVI-densified carbon/carbon composites with various fiber distributions. Composites Science and Technology. 2012;72(15):1892-1900.

[33]    K. I. Tserpes, A. G. Stamopoulos, Sp G. Pantelakis. A numerical methodology for simulating the mechanical behavior of CFRP laminates containing pores using X-ray computed tomography data. Composites Part B: Engineering. 2016;102:122-133.

[34]    N. Naouar, E. Vidal-Salle, J. Schneider, E. Maire, P. Boisse. 3D composite reinforcement meso F.E. analyses based on X-ray computed tomography. Composite Structures. 2015;132:1094-1104.

[35]    Garrett W. Melenka, Eric Lepp, Benjamin K. O. Cheung, Jason P. Carey. Micro-computed tomography analysis of tubular braided composites. Composite Structures.

2015;131:384-396.

[36]   H. L. Cox. THE ELASTICITY AND STRENGTH OF PAPER AND OTHER FIBROUS MATERIALS. British Journal of Applied Physics. 1952;3(MAR):72-79.

[37]   J. C. Halpin, S. W. Tsai. Environmental Factors in Composite Materials Design. AFML; 1967. p. 67-423.

[38]   J.C. Halpin. Stiffness and Expansion Estimates for Oriented Short Fiber Composites. Journal of Composite Materials. 1969;3(4):732-734.

[39]   Shao-Yun Fu, Bernd Lauke. Effects of fiber length and fiber orientation distributions on the tensile strength of SFRP. Composites Science and Technology. 1996;56:12.

[40]   Michael R. Piggott. Short Fibre Polymer Composites: a Fracture-Based Theory of Fibre Reinforcement. Journal of Composite Materials. 1994;28(7):588-606.

[41]   Z. Yu, J. Brisson, A. Ait-Kadi. Prediction of mechanical properties of short kevlar fiber-nylon-6,6 composites. Polymer Composites. 1994;15(1):64-73.

[42]   W. H. Bowyer, M. G. Bader. On the re-inforcement of thermoplastics by imperfectly aligned discontinuous fibres. Journal of Materials Science. 1972;7(11):1315-1321.

[43]   P.A. Templeton. Strength Predictions of Injection Molding Compounds. Journal of Reinforced Plastics and Composites. 1990;9(3):210-225.

[44]   A. R. Sanadi, M. R. Piggott. Interfacial effects in carbon-epoxies. Journal of Materials Science. 1985;20(2):421-430.

[45]   F. Ramsteiner, R. Theysohn. Tensile and impact strengths of unidirectional, short fibre-reinforced thermoplastics. Composites. 1979;10(2):111-119.

[46]   A. Kelly, W. R. Tyson. Tensile properties of fibre-reinforced metals: Copper/tungsten and copper/molybdenum. Journal Of the Mechanics And Physics Of Solids. 1965;13(6):329-350.

[47]   D. Mcnally, W. T. Freed, J. R. Shaner, W. Sell. A method to evaluate the effect of compounding technology on the stress transfer interface in short fiber reinforced thermoplastics. Polymer Engineering & Science. 1978;18(5):396-403.

[48]   H. L. Cox. The elasticity and strength of paper and other fibrous materials. British Journal of Applied Physics. 1952;3(3):72.

[49]   V. C. Li, Y. Wang, S. Backer. Effect of inclining angle, bundling and surface treatment on synthetic fibre pull-out from a cement matrix. Composites. 1990;21(2):132-140.

[50]   Fe Shaoyun, Zhou Benlian, Lung Chiwei. On the pull-out of fibers with fractal-tree structure and the interference of strength and fracture toughness of composites. Smart Materials and Structures. 1992;1(2):180.

[51]   Wei-Kuo Chin, Hsin-Tzu Liu, Yu-Der Lee. Effects of fiber length and orientation distribution on the elastic modulus of short fiber reinforced thermoplastics. Polymer

Composites. 1988;9(1):27-35.

[52]   M. Xia, H. Hamada, Z. Maekawa. Flexural Stiffness of Injection Molded Glass Fiber Reinforced Thermoplastics. International Polymer Processing. 1995;10(1):74-81.

[53]   L. T. Harper, T. A. Turner, N. A. Warrior, J. S. Dahl, C. D. Rudd. Characterisation of random carbon fibre composites from a directed fibre preforming process: Analysis of microstructural parameters. Composites Part a-Applied Science and Manufacturing. 2006;37(11):2136-2147.

[54]   L. T. Harper, T. A. Turner, N. A. Warrior, C. D. Rudd. Characterisation of random carbon fibre composites from a directed fibre preforming process: The effect of fibre length. Composites Part a-Applied Science and Manufacturing. 2006;37(11):1863-1878.

[55]   L. T. Harper, T. A. Turner, N. A. Warrior, C. D. Rudd. Characterisation of random carbon fibre composites from a directed fibre preforming process: The effect of tow filamentisation. Composites Part a-Applied Science and Manufacturing. 2007;38(3):755-770.

[56]   F. W. J. Van Hattum, C. A. Bernardo. A model to predict the strength of short fiber composites. Polymer Composites. 1999;20(4):524-533.

[57]   M. Hashimoto, T. Okabe, T. Sasayama, H. Matsutani, M. Nishikawa. Prediction of tensile strength of discontinuous carbon fiber/polypropylene composite with fiber orientation distribution. Composites Part a-Applied Science and Manufacturing. 2012;43(10):1791-1799.

[58]   S. Y. Fu, B. Lauke. The elastic modulus of misaligned short-fiber-reinforced polymers. Composites Science and Technology. 1998;58(3-4):389-400.

[59]   A. Gillet, O. Mantaux, G. Cazaurang. Characterization of composite materials made from discontinuous carbon fibres within the framework of composite recycling. Composites Part a-Applied Science and Manufacturing. 2015;75:89-95.

[60]   Paolo Feraboli, Tyler Cleveland, Patrick Stickler, John Halpin. Stochastic laminate analogy for simulating the variability in modulus of discontinuous composite materials. Composites Part a-Applied Science and Manufacturing. 2010;41(4):557-570.

[61]   Suresh G. Advani, Charles L. Tucker. The Use of Tensors to Describe and Predict Fiber Orientation in Short Fiber Composites. Journal of Rheology (1978-present). 1987;31(8):751-784.

[62]   J.C. Halpin, N.J. Pagano. The Laminate Approximation for Randomly Oriented Fibrous Composites. Journal of Composite Materials. 1969;3(4):720-724.

[63]   F. Zairi, M. Nait-Abdelaziz, J. M. Gloaguen, A. Bouaziz, J. M. Lefebvre. Micromechanical modelling and simulation of chopped random fiber reinforced polymer composites with progressive debonding damage. International Journal Of

Solids And Structures. 2008;45(20):5220-5236.

[64] A. Bouaziz, F. Zairi, M. Nait-Abdelaziz, J. M. Gloaguen, J. M. Lefebvre. Micromechanical modelling and experimental investigation of random discontinuous glass fiber polymer-matrix composites. Composites Science and Technology. 2007;67(15-16):3278-3285.

[65] Stephen W. Tsai, Jose Daniel D. Melo. An invariant-based theory of composites. Composites Science and Technology. 2014;100:237-243.

[66] S. Pimenta, P. Robinson. An analytical shear-lag model for composites with 'brick-and-mortar' architecture considering non-linear matrix response and failure. Composites Science and Technology. 2014;104:111-124.

[67] Saber Dormohammadi, Frank Abdi, Raghuram Mandapati, Harsh. K. Baid, Mike Lee, Umesh Gandhi. Impact Crush Modeling of Chopped Fiber Reinforced Polymers. American Society for Composites 30th Technical Conference. Kellogg Center, Michigan State University, East Lansing, Michigan, U. S.2015. p. 1899.

[68] B. W. Rosen. TENSILE FAILURE OF FIBROUS COMPOSITES. Aiaa Journal. 1964;2(11):1985-1991.

[69] C. L. Tucker, E. Liang. Stiffness predictions for unidirectional short-fiber composites: Review and evaluation. Composites Science and Technology. 1999;59(5):655-671.

[70] R. Hill. A SELF-CONSISTENT MECHANICS OF COMPOSITE MATERIALS. Journal Of the Mechanics And Physics Of Solids. 1965;13(4):213-&.

[71] Budiansk.B. ON ELASTIC MODULI OF SOME HETEROGENEOUS MATERIALS. Journal Of the Mechanics And Physics Of Solids. 1965;13(4):223-&.

[72] N. Laws, R. Mclaughlin. EFFECT OF FIBER LENGTH ON THE OVERALL MODULI OF COMPOSITE-MATERIALS. Journal Of the Mechanics And Physics Of Solids. 1979;27(1):1-13.

[73] T. W. Chou, S. Nomura, M. Taya. A SELF-CONSISTENT APPROACH TO THE ELASTIC STIFFNESS OF SHORT-FIBER COMPOSITES. Journal of Composite Materials. 1980;14(JUL):178-188.

[74] T. Mori, K. Tanaka. AVERAGE STRESS IN MATRIX AND AVERAGE ELASTIC ENERGY OF MATERIALS WITH MISFITTING INCLUSIONS. Acta Metallurgica. 1973;21(5):571-574.

[75] Y. Benveniste. A new approach to the application of mori-tanaka theory in composite-materials. Mechanics Of Materials. 1987;6(2):147-157.

[76] Nguyen Bn, J Paquette. EMTA's Evaluation of the Elastic Properties for Fiber Polymer Composites Potentially Used in Hydropower Systems. Richland, WA, U.S.: Pacific Northwest National Laboratory; 2010.

[77] H. Moussaddy, D. Therriault, M. Levesque. Modeling elastic properties of randomly oriented fiber composites.  ICCM 19. Canada2013.

[78] Shinichiro Yamashita. Effect of thin-ply on the material properties of chopped carbon fiber tape reinforced thermoplastics (CTT) [Graduation Thesis]. Tokyo, Japan: The University of Tokyo; 2017.

[79] Yi Wan, Jun Takahashi. Tensile and compressive properties of chopped carbon fiber tapes reinforced thermoplastics with different fiber lengths and molding pressures. Composites Part A: Applied Science and Manufacturing. 2016;87:271-281.

[80] Yizhuo Li, Soraia  Pimenta. Analytical prediction of strength for tow-based discontinuous composites.  5th ECCOMAS Thematic Conference on Mechanical Response of Composites. Bristol, UK2015. p. 7–9.

[81] Paolo Feraboli, Tyler Cleveland, Patrick Stickler, John Halpin. Stochastic laminate analogy for simulating the variability in modulus of discontinuous composite materials. Composites Part A: Applied Science and Manufacturing. 2010;41(4):557-570.

[82] P. Feraboli, E. Peitso, F. Deleo, T. Cleveland, P. B. Stickler. Characterization of Prepreg-Based Discontinuous Carbon Fiber/Epoxy Systems. Journal of Reinforced Plastics and Composites. 2009;28(10):1191-1214.

[83] Yuri Nikishkov, Luca Airoldi, Andrew Makeev. Measurement of voids in composites by X-ray Computed Tomography. Composites Science and Technology. 2013;89:89-97.

[84] Yi Wan, Jun Takahashi. CFRTP mechanical properties simulation by Mori-Tanaka model and equivalent laminate methods.  17th European Conference on Composite Materials. Munich, Germany2016.

[85] S. Sihn, R. Y. Kim, K. Kawabe, S. W. Tsai. Experimental studies of thin-ply laminated composites. Composites Science and Technology. 2007;67(6):996-1008.

[86] Tomohiro Yokozeki, Yuichiro Aoki, Toshio Ogasawara. Experimental characterization of strength and damage resistance properties of thin-ply carbon fiber/toughened epoxy laminates. Composite Structures. 2008;82(3):382-389.

[87] E-Xstream Engineering. DIGIMAT 5.0.1 manual2013.

[88] R. Hill. Elastic properties of reinforced solids: Some theoretical principles. Journal Of the Mechanics And Physics Of Solids. 1963;11(5):357-372.

[89] S. Nemat-Nasser, M. Hori. Micromechanics: overall properties of heterogeneous solids. North Holland1998.

[90] Z. Hashin. Analysis of Composite Materials—A Survey. Journal Of Applied Mechanics. 1983;50(3):481-505.

[91] Z. Hashin, Pennsylvania Univ Philadelphia Towne School Of Civil, Mechanical Engineering., University of Pennsylvania. Towne School Of Civil, Mechanical

Engineering, United States. Office of Naval Research. Theory of Mechanical Behavior of Heterogeneous Media: Defense Technical Information Center; 1963.

[92] J. D. Eshelby. The Determination of the Elastic Field of an Ellipsoidal Inclusion, and Related Problems1957.

[93] J.D. Eshelby. Elastic Inclusions and Inhomogeneities. In: I. N. Sneddon, R. Hill, editors. Progress in Solid Mechanics: North-Holland Publishing Company; 1961. p. 89-140.

[94] R. F. Eduljee, R. L. Mccullough, J. W. Gillespie. THE INFLUENCE OF INCLUSION GEOMETRY ON THE ELASTIC PROPERTIES OF DISCONTINUOUS FIBER COMPOSITES. Polymer Engineering and Science. 1994;34(4):352-360.

[95] T. Mura. Micromechanics of Defects in Solids: Springer Netherlands; 1987.

[96] T. S. Chow. EFFECT OF PARTICLE SHAPE AT FINITE CONCENTRATION ON ELASTIC-MODULI OF FILLED POLYMERS. Journal of Polymer Science Part B-Polymer Physics. 1978;16(6):959-965.

[97] R. M. Christensen. CORRECTION. Journal Of the Mechanics And Physics Of Solids. 1986;34(6):639-639.

[98] T. W. Clyne. A SIMPLE DEVELOPMENT OF THE SHEAR LAG THEORY APPROPRIATE FOR COMPOSITES WITH A RELATIVELY SMALL MODULUS MISMATCH. Materials Science and Engineering a-Structural Materials Properties Microstructure and Processing. 1989;122(2):183-192.

[99] R. F. Eduljee, R. L. Mccullough, J. W. Gillespie. THE INFLUENCE OF AGGREGATED AND DISPERSED TEXTURES ON THE ELASTIC PROPERTIES OF DISCONTINUOUS-FIBER COMPOSITES. Composites Science and Technology. 1994;50(3):381-391.

[100] W. B. Russel. EFFECTIVE MODULI OF COMPOSITE-MATERIALS - EFFECT OF FIBER LENGTH AND GEOMETRY AT DILUTE CONCENTRATIONS. Zeitschrift Fur Angewandte Mathematik Und Physik. 1973;24(4):581-600.

[101] T. S. Chow. ELASTIC-MODULI OF FILLED POLYMERS - EFFECT OF PARTICLE SHAPE. Journal of Applied Physics. 1977;48(10):4072-4075.

[102] J. Schjødt-Thomsen, R. Pyrz. The Mori–Tanaka stiffness tensor: diagonal symmetry, complex fibre orientations and non-dilute volume fractions. Mechanics Of Materials. 2001;33(10):531-544.

[103] M. R. Piggott, M. Ko, H. Y. Chuang. ALIGNED SHORT-FIBER-REINFORCED THERMOSETS - EXPERIMENTS AND ANALYSIS LEND LITTLE SUPPORT FOR ESTABLISHED THEORY. Composites Science and Technology. 1993;48(1-4):291-299.

[104] V. D. Azzi, S. W. Tsai. Anisotropic strength of composites. Experimental Mechanics.

1965;5(9):283-288.

[105]   Stephen W. Tsai, Edward M. Wu. A General Theory of Strength for Anisotropic Materials. Journal of Composite Materials. 1971;5(1):58-80.

[106]   G. P. Tandon, G. J. Weng. The Effect Of Aspect Ratio Of Inclusions on the Elastic Properties Of Unidirectionally Aligned Composites. Polymer Composites. 1984;5(4):327-333.

[107]   Dong-Li Shi, Xi-Qiao Feng, Yonggang Y. Huang, Keh-Chih Hwang, Huajian Gao. The Effect of Nanotube Waviness and Agglomeration on the Elastic Property of Carbon Nanotube-Reinforced Composites. Journal of Engineering Materials and Technology. 2004;126(3):250-257.

[108]   Y. Wan, T. Ohori, J. Takahashi. Mechanical properties and modeling of discontinuous carbon fiber reinforced thermoplastics.   the 20th International Conference on Composite Materials. Copenhagen, Denmark2015. p. 3222-4

[109]   C. J. Stimpson, C. D. Ernst, P. Knupp, P. P. P´Ebay, D. Thompson. The Verdict Library Reference Manual2007.

[110]   I. Doghri. Mechanics of Deformable Solids: Linear, Nonlinear, Analytical and Computational Aspects: Springer Berlin Heidelberg; 2000.

[111]   Shinichiro Yamashita, Yuto Nakashima, Jun Takahashi, Kazumasa Kawabe, Tetsuhiko Murakami. Tape length dependence of the electrical conductivity of ultra-thin chopped carbon fiber tape reinforced thermoplastics.   14th Japan International SAMPE Symposium and Exhibition. Kanazawa, Japan2015.

[112]   P. Feraboli, E. Peitso, T. Cleveland, P. B. Stickler. Modulus Measurement for Prepreg-based Discontinuous Carbon Fiber/Epoxy Systems. Journal of Composite Materials. 2009;43(19):1947-1965.

[113]   P. Feraboli, T. Cleveland, M. Ciccu, P. Stickler, L. Deoto. Defect and damage analysis of advanced discontinuous carbon/epoxy composite materials. Composites Part a-Applied Science and Manufacturing. 2010;41(7):888-901.

[114]   S. Y. Fu, B. Lauke, E. Mader, C. Y. Yue, X. Hu. Tensile properties of short-glass-fiber- and short-carbon-fiber-reinforced polypropylene composites. Composites Part a-Applied Science and Manufacturing. 2000;31(10):1117-1125.

[115]   A. Kelly, N.H. Macmillan. Strong solids: Clarendon Press; 1986.

# List of publications and awards

**(1) Journal Papers**

〔Peer-reviewed〕

(1-1)  **Yi Wan**, Tsuyoshi Matsuo, Isamu Ohsawa and Jun Takahashi, 'Effects of curvature on strength and damage modes of L-shaped carbon fiber-reinforced polypropylene', Journal of Reinforced Plastics and Composites, 2014, Vol. 33, No. 14, 1305–1315.

(1-2)  **Yi Wan** and Jun Takahashi, 'Deconsolidation behavior of carbon fiber reinforced thermoplastics', Journal of Reinforced Plastics and Composites, 2014, Vol. 33, No. 17, 1613-1624.

(1-3)  **Yi Wan** and Jun Takahashi, 'Tensile and compressive properties of chopped carbon fiber tapes reinforced thermoplastics with different fiber lengths and molding pressures', Composites Part a-Applied Science and Manufacturing. 2016, Vol. 87, 271-281.

(1-4)  **Yi Wan**, Ilya Straumit, Jun Takahashi and Stepan V. Lomov, 'Micro-CT analysis of internal geometry of chopped carbon fiber tapes reinforced thermoplastics', Composites Part a-Applied Science and Manufacturing. 2016, Vol. 91, 211-221.

(1-5)  **Yi Wan** and Jun Takahashi, 'Tensile properties and aspect ratio simulation of transversely isotropic discontinuous carbon fiber reinforced thermoplastics', Composites sciences and technology. 2016, Vol. 137, 167-176.

(1-6)  Xiuqi Lyu, Jun Takahashi, **Yi Wan** and Isamu Ohsawa, 'Determination of transverse flexural and shear moduli of chopped carbon fiber tape-reinforced thermoplastics by vibration', *Journal of Composite Materials*, accepted (2017/04/11), DOI: 10.1177/0021998317707815. (IF: 1.242)

(1-7)  Haowen Wei, Wataru Nagatsuka, Hooseok Lee, Isamu Ohsawa, Ken Sumimoto, **Yi Wan**, Jun Takahashi, 'Mechanical properties of carbon fiber paper reinforced thermoplastics made by mixed discontinuous recycled carbon fibers', *Advanced Composite Materials*, accepted (2017/04/30), DOI: 10.1080/09243046.2017.1334274. (IF: 1.029)

(1-8)  Xiuqi Lyu, **Yi Wan**, Jun Takahashi Isamu Ohsawa and Liaojun Yao, 'Health condition evaluation of carbon fiber reinforced thermoplastic with a tapping system', Journal of Thermoplastic Composite Materials. (2017/08/10, accepted)

〔Peer-reviewed　Under review *Italic under preparation*〕

(1-9)　　Xin Zhang, **Yi Wan**, Yu Sato and Jun Takahashi, 'Statistical analysis on tensile modulus of chopped fiber tape reinforced plastics', Journal of Composite Materials. (under review)

(1-10)　**Yi Wan**, Ilya Straumit, Jun Takahashi and Stepan V. Lomov, 'Micro-CT analysis of the orientation unevenness in random chopped strand composites in relation to the strand length', Composites Part a-Applied Science and Manufacturing. (under review)

(1-11)　*Xiuqi Lyu, Jun Takahashi, **Yi Wan** and Isamu Ohsawa,　'Strain rate and temperature dependence of elastic modulus of carbon fiber reinforced thermoplastics', Journal of Composite Materials.*

(1-12)　***Yi Wan** and Jun Takahashi,　'Mean filed homogenization and de-homogenization methods for predicting tensile properties of randomly oriented strands', Composites sciences and technology.*

(1-13)　***Yi Wan**, Ilya Straumit, Shinichiro Yamashita, Jun Takahashi and Stepan V. Lomov,　'Effect of internal geometry on the mechanical properties of chopped carbon fiber tapes reinforced thermoplastics with different tape thickness', Composites Part a-Applied Science and Manufacturing.*

(1-14)　***Yi Wan**, Ilya Straumit, Hirofumi Suganuma, Yuto Nakashima, Jun Takahashi and Stepan V. Lomov,　'Internal geometry and mechanical properties of randomly oriented strands with different fabrication processes', Composites Part a-Applied Science and Manufacturing.*

**(2) International Conference Proceeding：**

〔peer-reviewed　○: Presenter〕

(2-1)　　○ **Yi Wan**, Takeshi Goto, Tsuyoshi Matsuo, Isamu Ohsawa and Jun Takahashi, 'Investigation about fracture mode and strength in curved section of carbon fiber reinforced polypropylene', the 19th international conference on composite materials (ICCM19), pp. 6695-6702, Montreal, Canada, (July 2013).

(2-2)　　○ **Yi Wan**, Takeshi Goto, Tsuyoshi Matsuo, Isamu Ohsawa and Jun Takahashi, 'L-shaped tensile test for determining the minimum radius of CFRTP structure', the Composites Week, OA1, Leuven, Belgium, (September 2013).

(2-3)　　○ **Yi Wan**, Jun Takahashi and Isamu Ohsawa, 'Investigation about the springback effect

on short fiber reinforced thermoplastics', the 13th Japan International SAMPE Symposium & Exhibition (JISSE13), 1802, Nagoya, Japan, (November 2013).

(2-4) ○ **Yi Wan** and Jun Takahashi, 'Thermal deformation caused by residual stress in short fiber reinforced thermoplastics', the 35th international conference of SAMPE Europe 2014 (SAMPE SEICO14), pp. 343-350, Paris, France, (March 2014).

(2-5) ○ **Yi Wan** and Jun Takahashi, 'Fiber length effect on tensile and compressive strength of short fiber reinforced thermoplastics', the 16th European conference on composite materials (ECCM16), 25.1.1-R11, Seville, Spain, (June 2014).

(2-6) ○ **Yi Wan** and Jun Takahashi, 'Investigation of the deconsolidation effect of carbon mat reinforced thermoplastics', the 9th Asian-Australasian conference on composite materials (ACCM9), I-004, Suzhou, China, (October 2014).

(2-7) ○ **Yi Wan** and Jun Takahashi, 'Effect of tape length and impregnation conditions on mechanical properties of carbon fiber tape reinforced thermoplastics', the 12th International Conference on Textile Composites (TEXCOMP-12), Poster 4, Raleigh, NC, U.S.A., (May 2015).

(2-8) ○ **Yi Wan** and Jun Takahashi, 'Bending and impact properties of randomly orientated discontinuous carbon fiber reinforced thermoplastics with thin-ply structure', the 23rd Annual International Conference on Composites/NANO Engineering (ICCE-23), pp. 743-744, Chengdu, China, (July 2015).

(2-9) ○ Xiuqi Lyu, **Yi Wan**, Wataru Nagatsuka and Jun Takahashi, 'Determination of strain rate dependent young's modulus of carbon fiber reinforced thermoplastics by static and dynamic tests', the 23rd Annual International Conference on Composites/NANO Engineering (ICCE-23), pp. 513-514, Chengdu, China, (July 2015).

(2-10) ○ **Yi Wan**, Toshiro Ohori and Jun Takahashi, 'Mechanical properties and modeling of discontinuous carbon fiber reinforced thermoplastics', the 20th International Conference on Composite Materials (ICCM20), 3222-4, Copenhagen, Denmark, (July 2015).

(2-11) ○ ワンイー, 髙橋淳, '森・田中理論を用いた CTT 材の最適テープ長決定方法', 日本複合材料学会第４０回複合材料シンポジウム, B1-09, 金沢, (2015 年 9 月).

(2-12) ○ Xiuqi Lyu, **Yi Wan**, Jun Takahashi and Wataru Nagatsuka, 'Measurement of temperature dependence of flexural modulus of carbon fiber reinforced thermoplastics by dynamic test', the 40th Symposium of Japan Society for Composite Materials (JSCM 2015), C1-02, Kanazawa, Japan, (September 2015).

(2-13) ○ Hanchul Lee, Shuli Tang, Toshiro Ohori, Takahiro Hayashi, **Yi Wan**, Jun Takahashi,

Isammu Ohsawa, Kazumasa Kawabe and Tetsuhiko Murakami, 'Applicability of FEM to complex shape parts made by ultra-thin chopped carbon fiber tape reinforced thermoplastics', the 14th JAPAN international SAMPE symposium and exhibition (JISSE14), Kanazawa, Japan, (December 2015).

(2-14) ○ Taro Nakamura, **Yi Wan**, Haowen Wei and Jun Takahashi, 'Investigation of sandwich panel made by CFRTS and CFRTP', the 14th JAPAN international SAMPE symposium and exhibition (JISSE14), Kanazawa, Japan, (December 2015).

(2-15) ○ **Yi Wan** and Jun Takahashi, 'CFRTP mechanical properties simulation by Mori-Tanaka model and equivalent laminate methods', the 17th European Conference on Composite Materials (ECCM17), TUE-4_BIA_3.09-02, Munich, Germany, (June 2016).

(2-16) ○ Daiki Kobayashi, **Yi Wan**, Lee Hanchul, Taro Nakamura, Haowen Wei, Jun Takahashi and Isamu Ohsawa, 'Flow behavior of complex shaped hybrid CFRTP during compression molding, the 17th European Conference on Composite Materials (ECCM17), MON-4_STG_5.09-13, Munich, Germany, (June 2016).

(2-17) ○ Xiuqi Lyu, Jun Takahashi and **Yi Wan**, 'Analysis of viscoelastic behaviour of ultra-thin chopped carbon fiber tape reinforced thermoplastics with different tape lengths', the 17th European Conference on Composite Materials (ECCM17), TUE-4_BIA_3.09-01, Munich, Germany, (June 2016).

(2-18) ○ Saber DorMohammadi, M. Lee, M. Repupilli, F. Abdi, **Yi Wan**, Jun Takahashi and H. Huang, 'Multi-Scale Computational Modeling of Short Fiber Reinforced Thermoplastics', 31st ASC Technical Conference and ASTM D30 Meeting, Williamsburg, Virginia, U.S., (September 2016).

(2-19) ○ **Yi Wan** and Jun Takahashi, 'Modeling analysis and evaluation of tensile properties of discontinuous CFRTP using homogenization and de-homogenization methods', 2016 SAMPE International Education Program, The composites and advanced materials EXPO (CAMX), Anaheim, California, (September 2016).

(2-20) ○ ワンイー, 髙橋淳, '熱可塑性樹脂複合材料のランダム配向ストランド（ROS）の微視的構造の定量化と可視化', 第８回日本複合材料会議, 東京,（2016年３月）.

(2-21) ○ **Yi Wan**, Ilya Straumit, Stepan V. Lomov and Jun Takahashi, 'Internal geometry analysis of discontinuous carbon fiber reinforced thermoplastics with two micro-CT methods', 3rd International Conference on Tomography of Materials and Structure (ICTMS-2017), Lund, Sweden, (June 2017).

〔peer-reviewed ○: Presenter Accepted〕

(2-22)  ○ **Yi Wan** and Jun Takahashi, 'Multi-scale internal geometry analysis and mechanical modeling of randomly oriented strands', the 21st International Conference on Composite Materials (ICCM21), Xi'an, China, (August 2017).

(2-23)  ○ Bing Xiao, **Yi Wan**, Isamu Ohsawa and Jun Takahashi, 'Needle punching effect on compression molded carbon fiber paper reinforced thermoplastics', the 21st International Conference on Composite Materials (ICCM21), Xi'an, China, (August 2017).

(2-24)  ○ Daiki Kobayashi, Taro Nakamura, **Yi Wan**, Isamu Ohsawa and Jun Takahashi, 'Investigation of springbacked carbon fiber reinforced thermoplastics hybrid structures', the 21st International Conference on Composite Materials (ICCM21), Xi'an, China, (August 2017).

(2-25)  ○ Yunqian Zhang, **Yi Wan**, Taro Nakamura and Jun Takahashi, 'Effect of springback ratio on bending and impact property of carbon fiber reinforced thermoplastics sandwich structures', the 21st International Conference on Composite Materials (ICCM21), Xi'an, China, (August 2017).

(2-26)  ○ **Yi Wan** and Jun Takahashi, 'Internal geometry analysis and mechanical property simulation of randomly oriented strands', the 15th European-Japanese Meeting on Composite Materials, London, UK, (September 2017).

(2-27)  Jun Takahashi, Michinobu Fujita and **Yi Wan** 'Toward a new generations of composites for our common future - some activities on cfrtp for automotive applications –', the 15th European-Japanese Meeting on Composite Materials, London, UK, (September 2017).


〔Invited Presentation〕

(2-28)  **Yi Wan**, 'General activities and specific researches of CFRTP (carbon fiber reinforced thermoplastics) for mass production automotive in Japan', Department of Organic Materials Fiber Engineering, Chonbuk National University, Korea, July 9 2015, Inviting person: Prof. Seong Su Kim.

(2-29)  **Yi Wan**, 'Mechanical properties and structures of short carbon fiber reinforced thermoplastics', Fachhochschule Nordwestschweiz, Hochschule für Technik, Institut für Kunststofftechnik, Swiss, November 12 2015, Inviting person: Prof. Clemens Dransfeld.

(2-30)  **Yi Wan**, 'Development and research of discontinuous carbon fiber reinforced thermoplastics in Japan', Centre for Advanced Materials Technology, School of Aerospace, Mechanical and Mechatronic Engineering, The University of Sydney,

Australia, June 14, 2017, Inviting person: Prof. Lin Ye.

**(3) Awards**：

(3-1)　Outstanding Undergraduate Thesis (Top 5% students), Beihang University, Beijing, China, (June 2012).

(3-2)　Best Student Paper Award, the 13th Japan International SAMPE Symposium & Exhibition (JISSE13), Nagoya, Japan, (November 2013).

(3-3)　東京大学工学系研究科長賞（修士）, (2015 年 3 月).

(3-4)　Finalist of the Tsai Best Student Paper Award Competition, ICCM20, Copenhagen, Denmark, (July 2015).

(3-5)　林学生賞，日本複合材料学会第 40 回複合材料シンポジウム，金沢工業大学，(2015 年 9 月).

(3-6)　Finalist of the SAMPE International Education Program, PhD Candidate, The composites and advanced materials EXPO (CAMX), Anaheim, California, (September 2016).

(3-7)　優秀学生講演賞，第 8 回日本複合材料会議（JCCM-8），東京，(2017 年 3 月).

(3-8)　SAMPE（先端材料技術協会）日本支部　奨学賞，(2017 年 7 月).